



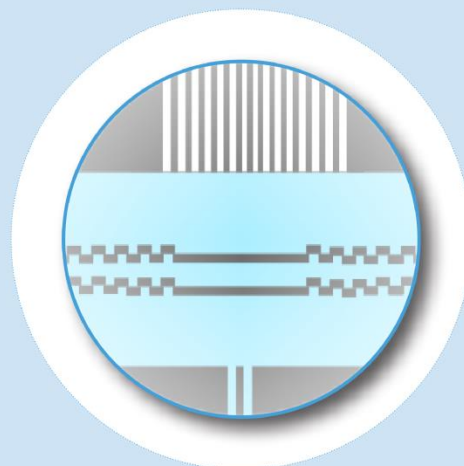
Berichte aus dem
Institut für Technische Optik

Nr. 97

INSTITUT FÜR
TECHNISCHE OPTIK
UNIVERSITÄT STUTT GART

Huiyu Li

Design, fabrication and
characterization of
a cascaded plasmonic superlens
for the visible spectrum



Januar 2019



Universität Stuttgart

Design, fabrication and characterization of a cascaded plasmonic superlens for the visible spectrum

Von der Fakultät für Konstruktions-, Produktions- und Fahrzeugtechnik
der Universität Stuttgart
zur Erlangung der Würde eines Doktor-Ingenieurs (Dr.-Ing.)
genehmigte Abhandlung

Vorgelegt von

M.Eng. Huiyu Li
aus China

Hauptberichter: Prof. Dr. sc. nat. Wolfgang Osten

Mitberichter: Prof. Dr.-Ing. Manfred Berroth

Tag der mündlichen Prüfung: 31.01.2019

Institut für Technische Optik der Universität Stuttgart

2019

ISBN 978-3-923560-96-7

D 93 Stuttgart

Vorwort des Herausgebers

Hochentwickelte Methoden zur Verbesserung des Auflösungsvermögens (engl. resolution enhancement) kommen vor allem bei der Abbildung von mikroskopischen und nanoskopischen Objekten zum Einsatz. Derartige Verfahren stellen zumindest eine beugungsbegrenzte Abbildung oder, wenn überhaupt möglich, darunter in Aussicht. Im Ergebnis der rasanten Verkleinerung der Strukturbreiten in der Halbleitertechnologie, die gegenwärtig kritische Dimensionen von 10nm in Serie verzeichnet, und der breiten Anwendung licht-mikroskopischer Verfahren in den Lebenswissenschaften zur Sichtbarmachung von Zellen und Gewebestrukturen, mit denen u.a. das Ziel verfolgt wird, Krankheiten frühzeitig zu erkennen und Diagnosen auf sichere Füße zu stellen, hat sich inzwischen eine Reihe von neuen Mikroskopie-Techniken etabliert, deren außergewöhnliche Leistung mit Prädikaten, wie super-resolved, höchstauflösend und resolved beyond the diffraction limit beworben wird. Es würde zu weit führen, all diese neuen Methoden hier zu zitieren. Es sei jedoch zumindest erwähnt, dass es sich bei einer Vielzahl von neuen Schöpfungen aus der sog. Superresolution-Sparte lediglich um Verfahren handelt, die u.U. Beugungsbegrenzung erzielen, das Abbe-Limit jedoch nicht unterschreiten. Weitere Verfahren, wie PALM und STORM sind der sog. Lokalisationsmikroskopie zuzuordnen, die auf dem Ein- und Ausschalten von Floreszenz in einzelnen Molekülen beruht. Die sehr leistungsfähige STED-Mikroskopie gewinnt ihren Vorteil im Vergleich zur klassischen Mikroskopie ebenfalls durch Rückgriff auf nichtlineare Übertragungsprinzipien und eine geschickte Maskierung der Impulsantwort mittels selektiver Deaktivierung von Fluorophoren. Allen diesen Verfahren ist jedoch gemeinsam, dass sie das Fernfeld auswerten und keinen Zugriff auf die nicht-propagierenden Komponenten des Wellenfeldes haben, die sog. evaneszenten Wellen, die jene hohen Ortsfrequenzen repräsentieren, die von Strukturbreiten herrühren, deren Dimensionen kleiner als die der Wellenlänge des benutzten Lichts sind. Die Nahfeldmikroskopie geht einen anderen Weg und tastet das Nahfeld mit sog. Nahfeldsonden ab, deren Apertur deutlich kleiner ist als die Wellenlänge. Das Verfahren ist jedoch sowohl technisch als auch zeitlich sehr aufwendig und es kommt u.U. zu Artefakten bei der Interpretation der gewonnenen Bilddaten. Die Implementierung mikroskopischer Methoden, die eine ideale Abbildung auch ohne Zugriff auf nichtlineare photophysikalische Prozesse ermöglichen und insbesondere die Propagation der Nahfeldkomponenten mit dem Ziel einer verbesserten Fernfeldauswertung induzieren, ist daher ein langgehegter Wunsch in der Mikro-

skopie. Hoffnung kam auf, als Sir John Pendry die Ideen von Wiktor Wesselago über die Existenz von Negativ-Index-(NI)-Materialien, auch als Meta-Materialien bezeichnet, aufnahm und unter deren Einsatz eine ideale Linse postulierte. Seitdem ist die Suche nach NI-Superlinsen ungebrochen und es existiert eine Vielzahl von Design-Vorschlägen. Mit der Implementierung von NI-Superlinsen, die eine physikalisch solide Auflösung unterhalb der Beugungsgrenze in Aussicht stellen, gehen jedoch einige strenge Herausforderungen einher. Während Pendrys Vorschlag auf eine ideale 1:1-Abbildung hinausläuft, ist das Moment der Vergrößerung für die Mikroskopie unverzichtbar. Hinzu kommt, dass eine echte Auflösungssteigerung über die Beugungsgrenze hinaus nur dann gelingt, wenn die Propagation der Nahfeldkomponenten ermöglicht wird. Das bedeutet zum einen die Anregung der evaneszenten Wellen und zum anderen deren Übertragung bzw. Propagation mittels induzierter Plasmonenresonanz. Die Literatur kennt bisher eine Reihe von Super-Linsen-Implementierungen, angefangen bei der einfachen 1:1-Super-Linse, über die Fernfeld-Superlinse bis hin zur sog. Hyper-Lens, mit der die Vergrößerung von einfachen sub-Wellenlängen-Strukturen gezeigt werden konnte. Frau Li knüpft an diese Ergebnisse an und entwickelt insbesondere die Ergebnisse der Dissertation von Herrn Schau systematisch weiter. Sie stellt sich dabei folgenden Herausforderungen: Design, Simulation, Fertigung und Erprobung einer Superlinse zur direkten Abbildung von Sub-Wellenlängen-Strukturen im sichtbaren Wellenlängenbereich. Das Konzept von Frau Li setzt dabei direkt auf die Anregung propagierender Nahfeldmoden, die nach Ausbreitung ins Fernfeld zur weiteren Strukturabbildung bzw. –Vergrößerung mit einem konventionellen Mikroskop genutzt werden können. Die Kopplung der Plasmonenresonanz an das Photonenfeld, die Fernfeldpropagation und Vergrößerung werden dabei systematisch durch die Implementierung einer kaskadierten Doppelstruktur, bestehend aus einer Doppel-Mäander-Kavität (double layer meander cavity structure DLMC) und einer planaren plasmonischen Linse (planar plasmonic lens PPL), erzielt. Indem also Nahfeldmoden der konventionellen Abbildung im sichtbaren Wellenlängenbereich zugänglich gemacht werden, geht Frau Li mit Ihrer Dissertation deutlich über den Stand der Technik hinaus. Hervorzuheben ist insbesondere, dass Frau Li eine geglückte Symbiose aus innovativem Design, präziser Simulation, aufwendiger und geschickter Herstellung der komplizierten Strukturen sowie deren sorgfältiger experimenteller Evaluation gelingt.

Stuttgart, März 2019

Prof. Dr. Wolfgang Osten
Institut für Technische Optik
Universität Stuttgart

Contents

| | |
|---|-----------|
| List of abbreviations | 8 |
| List of symbols | 9 |
| Abstract | 10 |
| Kurzzusammenfassung | 13 |
| 1 Introduction | 21 |
| 2 State of the art in resolution enhanced imaging | 24 |
| 2.1 Resolution limit of conventional microscopes | 24 |
| 2.2 Superresolution with scanning or post-processing | 25 |
| 2.3 Metalenses, microsphere and other methods | 27 |
| 2.4 The plasmonic superlens | 28 |
| 3 Design and working principle of a cascaded plasmonic superlens | 32 |
| 3.1 Introduction to the new design and its advantages compared to existing plas- monic superlenses | 32 |
| 3.1.1 The new design of a cascaded superlens | 32 |
| 3.1.2 Imaging with high spatial frequency information | 33 |
| 3.1.3 Simulation method: rigorous coupled wave analysis | 37 |
| 3.1.4 Advantages of the design | 41 |
| 3.2 Dispersion engineering with metallic meander stacks | 42 |
| 3.2.1 Surface plasmon polaritons | 42 |
| 3.2.2 Excitation of surface plasmon polaritons with meander structures | 44 |
| 3.2.3 Near-field transmission dispersion of the DLMC structure | 46 |
| 3.3 Phase compensation of the PPL structure | 48 |
| 3.3.1 Phase retardation through nano-slits | 48 |
| 3.3.2 Imaging by a planar plasmonic lens | 50 |

| | | |
|----------|---|-----------|
| 4 | Simulation of the functions of the cascaded superlens | 52 |
| 4.1 | Near-field transfer function of the cascaded superlens | 52 |
| 4.1.1 | Wave dispersion of the cascaded superlens | 52 |
| 4.1.2 | Phase compensation introduced by the PPL structure | 55 |
| 4.2 | Numerical calculations of the cascaded superlens using Microsim | 56 |
| 4.2.1 | Lateral resolution of the cascaded superlens | 56 |
| 4.2.2 | Influence of the position shift between the sub-components | 58 |
| 4.2.3 | Discussion of parameter tolerance for the cascaded superlens | 61 |
| 5 | Fabrication and characterization of the sub-components in the cascaded superlens | 63 |
| 5.1 | Introduction to fabrication facilities and processes | 63 |
| 5.1.1 | Film deposition techniques | 63 |
| 5.1.2 | Focused ion beam system for nano-fabrication | 65 |
| 5.1.3 | Optical characterization methods | 66 |
| 5.1.4 | Fabrication processes | 67 |
| 5.2 | Preparation for the fabrication | 69 |
| 5.2.1 | Challenges in the fabrication process | 69 |
| 5.2.2 | Deposition of metallic films | 69 |
| 5.2.3 | Focused ion beam milling | 73 |
| 5.3 | Characterization of the fabricated sub-components in the cascaded superlens . . | 76 |
| 5.3.1 | Characterization of the fabricated DLMC structures | 76 |
| 5.3.2 | Optical verification of the fabricated PPL structure | 79 |
| 5.4 | Assembly of the cascaded structure with a dielectric spacer | 82 |
| 6 | Experimental verification of the cascaded superlens | 86 |
| 6.1 | Image of pair-slits under conventional microscope | 86 |
| 6.2 | Preliminary imaging test of the cascaded superlens | 88 |
| 6.3 | Lateral resolution of the fabricated cascaded superlens | 90 |
| 6.4 | Lessons learned | 94 |
| 7 | Modification of the cascaded superlens | 96 |
| 7.1 | Introduction to the design of a modified cascaded superlens | 96 |
| 7.2 | Simulation results of the modified cascaded superlens | 97 |
| 7.2.1 | Near-field transmission dispersion of the DBR-PCL structure | 97 |
| 7.2.2 | Near-field transmission dispersion of the modified cascaded superlens . . | 102 |
| 7.2.3 | Numerical study of the modified cascaded superlens | 102 |
| 7.3 | Fabrication and experimental verification of the modified cascaded superlens . . | 105 |
| 7.3.1 | Fabrication of the modified meander structure | 105 |

| | | |
|----------|--|------------|
| 7.3.2 | Imaging tests of the modified cascaded superlens | 107 |
| 8 | Summary and outlook | 110 |
| 8.1 | Summary | 110 |
| 8.2 | Outlook | 111 |
| | Bibliography | 113 |
| | publication | 126 |
| | Lebenslauf | 127 |

List of abbreviations

| | |
|---------|---|
| AFM | Atomic force microscope |
| CCD | Charge coupled device |
| DLMC | Double layer meander cavity |
| DBR-PCL | Planar cavity lens integrated with distributed Bragg reflectors |
| E-gun | Electron-beam physical vapor deposition |
| FIB | Focused ion beam |
| FTIR | Fourier-transform infrared spectroscopy |
| FWHM | Full width half maximum |
| ICP-RIE | Inductively coupled plasma-reactive ion etching |
| LRSP | Long range surface plasmon |
| NA | Numerical aperture |
| NTF | Near-field transfer function |
| PALM | Photo activated localization microscopy |
| PPL | Planar plasmonic lens |
| PSF | Point spread function |
| RCWA | Rigorous coupled-waves analysis |
| SEM | Scanning electron microscope |
| SNR | Signal-to-noise ratio |
| SNOM | Scanning near-field optical microscopy |
| STORM | Stochastic optical reconstruction microscopy |
| SOG | Spin-on-glass |
| SRSPP | Short range surface plasmon |
| SPPs | Surface plasmon polaritons |
| STED | Stimulated emission depletion |
| STEDD | Stimulation emission double depletion |
| TM | Transverse magnetic |
| TE | Transverse electric |

List of symbols

| | |
|---------------|--|
| λ | Incident wavelength |
| \mathbf{E} | Electric vector field, |
| \mathbf{D} | Displacement current |
| \mathbf{H} | Magnetic field |
| \mathbf{B} | Magnetic induction |
| J | Current density |
| ρ | Charge density |
| ε | Spatially permittivity |
| μ | Spatially permeability |
| n | Refractive index |
| k_0 | Wave vector |
| k_x | Transverse wave vector |
| X_D | Distance of double slits from center to center |
| D_O | Thickness of the object |
| D_{OM} | Distance between object and cascaded superlens |
| D_{DM} | Thickness of double layer meander cavity |
| D_C | Coupling distance between two sub-components |
| D_{PL} | Thickness of planar plasmonic lens |
| D_{spa} | Distance between meander structure |
| P_x | Period of the meander cavity |
| W_r | Width of the gratings in meander structure |
| d | Thickness of films in meander structure |
| t | Depth of the meander |

Abstract

Optical microscopy is one of the most important imaging techniques. However, its resolution is diffraction limited. To obtain an image with superresolution, plenty of efforts have been devoted to subwavelength imaging. Most of the solutions are time consuming, e.g. stimulated emission depletion needs scanning process [1]. For direct imaging, plasmonic lenses are proposed, e.g. a hyperlens for direct far-field imaging [2]. But the working frequencies of the plasmonic lenses are ultra violet and recently it is demonstrated that plasmonic lenses with multi-layers have fundamental limitations for imaging because of their high optical loss [3]. The goal of this dissertation is to design and to fabricate a cascaded superlens for directly imaging objects with subwavelength features in the far field at visible spectrum. Such a superlens can be useful for the improvement of the resolution of a conventional microscope. Here, two superlens designs are proposed that are based on a concept suggested by Ma et al. [4] to achieve super resolution with a wide transverse wave vector coverage and a compression of lateral transverse wave vector.

In the original lens design, the cascaded superlens is composed of a double layer meander cavity (DLMC) structure and a planar plasmonic lens (PPL). The DLMC structure is employed for coupling evanescent waves via excitation of surface plasmon polaritons. The periodical corrugation in the DLMC structure helps to fold the dispersion of surface plasmon polaritons at the metal/dielectric interface to visible wavelengths. The PPL structure is used to introduce a phase compensation via nano-slits with different sizes in a thick metal film. With a proper design, we can obtain a planar lens with a focal length of several micrometers. The PPL structure was chosen due to its compact size and flexibility for design. In the modified lens design, a planar cavity lens (PCL) is utilized to replace the DLMC structure to solve an alignment problem between the DLMC structure and the object brought by the corrugation of the films. However, in the modified design, the optical response of the PCL structure (composed of two layers of metallic films) is at violet wavelength. To tune the performance wavelength to the visible range and to enhance the near field transmission, distributed Bragg reflectors (DBR) are integrated to the PCL structure around the lens center, forming additional lateral cavities for surface waves. Dispersion of the DLMC structure or the DBR-PCL structure is taken as the near-field transfer function, with which the information carried by high transverse

wave vector can be transferred. In this dissertation, both simulation and fabrication results of the cascaded superlens are reported.

Simulations for the cascaded superlenses are performed with an in-house developed software package Microsim based on rigorous coupled wave analysis (RCWA). We first study the near-field transmission dispersion of the DLMC structure, which is used as near-field transfer function. The dispersion covers a range of $2k_0$ in terms of the transverse wave vector with proper structural parameters. For the DBR-PCL structure, its dispersion is generated in a broader frequency range (from 350 to 700 THz) with a larger range of transverse wave vector. Then we design the PPL structure for phase compensation considering the feasibility for fabrication. The structural parameters are optimized for the wavelength of 640 nm. Imaging properties of the cascaded superlenses (the DLMC or DBR-PCL structure stacked with the PPL structure) with the optimized parameters are illustrated by using a pair-slit in a chromium layer as an object. The PPL structure alone cannot be applied for imaging when the structure is placed in the near field of an object due to grating diffraction. However, the transmission peaks from the PPL structure are greatly suppressed when the PPL is combined with a DLMC or a DBR-PCL structure. With the cascaded superlenses, we can obtain a lateral resolution of 180 nm for the original design or 200 nm for the modified design at the wavelength of 640 nm in the far field. In the end, we have also studied the tolerance of the structural parameters. The results roughly show that if we change the structural parameters less than 10% of the optimized ones, their influences to imaging can be neglected.

With the parameters optimized in the simulation, the cascaded superlenses were fabricated for experimental verification. We fabricated and characterized the two sub-components, the DLMC/DBR-PCL structure and the PPL structure, separately to ensure that they each work as designed. We then stacked them together to achieve an entire superlens. The optical property of the DLMC/DBR-PCL structure was characterized by a Fourier transformation infrared spectroscopy and that of the PPL structure was characterized by a conventional microscope. Cross sections of all the structures were further checked with a scanning electron microscope. To experimentally verify the lateral resolution of the cascaded superlens, a pair-slit with different sizes in a chromium layer was fabricated as an object. The image of pair-slits with different sizes were measured first to check the actual lateral resolution of our microscope. Then the pair-slit object was measured with presence of the superlens under the same microscope.

For the cascaded superlens with the original design, we first use a pair-slit with slit width of 400 nm and slit distance of 800 nm for a detail study of the far field distributions projected by the cascaded superlens. Then we decrease the slit width to 100 nm and the slit distance to 180 nm to test the lateral resolution of the cascaded superlens. The obtained experimental

results achieve a lateral resolution down to 180 nm at the wavelength of 640 nm, demonstrating that the superlens has been successfully fabricated.

In the experimental verification of the cascaded superlens with the original design, we find that the relative position between the DLMC structure and the slit object influences the image field distribution heavily. To solve the problem, a PCL structure is introduced to replace the DLMC structure. Furthermore, a DBR structure is integrated to the sides of the PCL structure to fold the working wavelength back to the visible range. For the modified design, the simulation was performed not only to study the lateral resolution but also to study whether the design with the DBR-PCL structure works in diminishing the critical alignment problem existing in the original design. In the experimental verification, we change the relative lateral position between the DBR-PCL structure and the pair-slit object. The obtained results achieve a lateral resolution of 200 nm at the incident wavelength of 640 nm. The obtained results demonstrate that the modified cascaded superlens solves the alignment problem. Furthermore, the modified design provides a possibility to use the superlens under white incident light due to its broad spectral response within a larger transverse wave vector (the PPL structure needs to be modified or replaced with the variation of the wavelength).

Our results demonstrate that the concept of realizing a far-field superlens by wave coupling and image magnification separately works well. Experimental results agree well with the simulations thanks to precise controlled fabrication procedure. The successfully fabricated nano-sized structures pave the way for further fabricating structures with similar sizes (e.g. thin metallic film on meander structure) as well.

The following papers showing the results were published:

- Li, Huiyu, Liwei Fu, Karsten Frenner, and Wolfgang Osten. "Cascaded plasmonic superlens for far-field imaging with magnification at visible wavelength." *Optics Express* 26, no. 8 (2018): 10888-10897,
- Li, Huiyu, Liwei Fu, Karsten Frenner, and Wolfgang Osten. "Cascaded DBR plasmonic cavity lens for far-field subwavelength imaging at a visible wavelength." *Optics Express* 26, no. 15 (2018): 19574-19582,
- Li, Huiyu, Liwei Fu, Karsten Frenner, and Wolfgang Osten. "Nanofabrication results of a novel cascaded plasmonic superlens: lessons learned." *Proc. SPIE*, vol. 10330, (2017): 103300Y.

Kurzzusammenfassung

Das Ziel dieser Dissertation ist es, eine kaskadierte Superlinse zur direkten Abbildung von Objekten mit Subwellenlängeigenschaften im Fernfeld bei einer sichtbaren Wellenlänge (z. B. 640 nm in dieser Dissertation) mit Hilfe eines herkömmlichen Mikroskops zu untersuchen und herzustellen.

Plasmonische Superlinsen wurden als eine vielversprechende Lösung für die Bildgebung jenseits der Beugungsgrenze in Echtzeit vorgestellt, da sie evaneszente Wellen verstärken und übertragen können [5, 6]. Künstliche anisotrope Medien[7–10] oder hyperbolische Metamaterialien (HMMs)[2, 11–13], die abwechselnd aus Metallschichten und Schichten aus Dielektrika bestehen, sind die am intensivsten untersuchten Strukturen zur Erzielung einer Subwellenlängenabbildung bei optischen Frequenzen aufgrund der Anregung und Nahfeldwechselwirkung von Oberflächenplasmonpolaritonen (SPPs) an der Metall/Dielektrikum Schnittstelle [5, 11, 14–17]. Da die Plasmonenresonanz von dafür geeigneten Edelmetallen, wie Silber, Gold oder Aluminium, im ultravioletten Wellenlängenbereich liegt, wurde eine Spezielle Auslegung der Strukturen vorgenommen, um die Wellenlänge auf den sichtbaren Spektralbereich abzustimmen [2, 18–20]. Unter Verwendung von Hochindex-Dielektrika kann die optische Antwort einer Silberschicht oder eines HMM ausschließlich zu violetten Wellenlängen verschoben werden [2, 18]. Ein effektiver Weg, die Transmissionsspektren von HMMs über den sichtbaren Bereich abzustimmen, ist die Anzahl der Silberschichten zu erhöhen und eine Verringerung ihrer Dicke auf beispielsweise 10 nm vorzunehmen [16]. Es wurde jedoch kürzlich gezeigt [3], dass solche Mehrschichtstrukturen grundlegende Nachteile für die Bildgebung besitzen, da die Bildauflösung mit der Anzahl der Schichten aufgrund von erhöhtem Verlust und der Unterdrückung hoher Ortsfrequenzen abnimmt. Eine weitere Einschränkung der plasmonischen Superlinse besteht darin, dass das von den Superlinsen projizierte Bild immer noch evaneszent ist. Folglich ist es weiterhin eine große Herausforderung, das Nahfeldbild in das Fernfeld zu übertragen. Hyperlinsen, die durch Auftragen von HMMs auf einer gekrümmten Oberfläche hergestellt werden, können als Fernfeld-Superlinse wirken, da das Nahfeldbild durch die Lichtausbreitung vergrößert wird. Neben den auftretenden hohen Verlusten beschränkt auch die gekrümmte Objektoberfläche ihre praktische Anwendbarkeit [2, 9, 21]. Andere Arten von Fernfeld-Superlinsen oder Fernfeld-Subwellenlängen-Bildgebungsverfahren wurden vorgeschlagen oder demonstriert, z .B

eine Metallplatte, die auf einer Seite mit Subwellenlängengitter strukturiert [22] ist strukturierte Nahfeldbeleuchtung [23–25], "Sparse" Rekonstruktion oder selektive Anregung lokalisierter Oberflächenplasmonen [26, 27]. Diese Methoden erfordern jedoch eine Nachbearbeitung der Bilder oder einscannendes Aufnahmeverfahren.

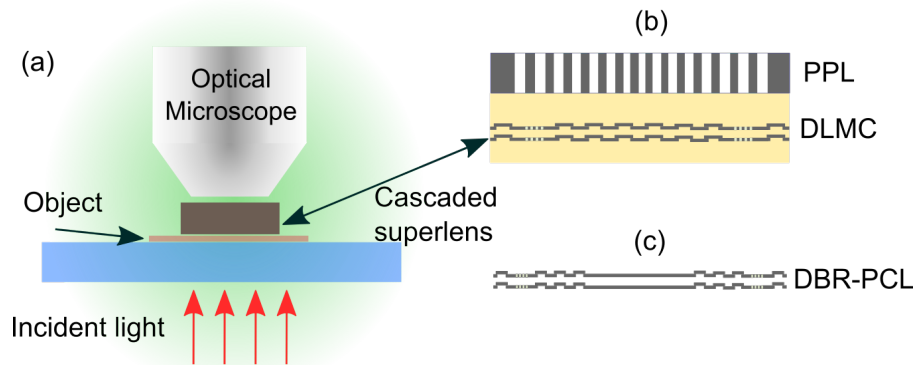


Abbildung K.1 (a) Messaufbau der Subwellenlängenabbildung unter Verwendung einer Fernfeld-Superlinse kombiniert mit einem Mikroskop; (b) Schema des ursprünglichen Entwurfs (Querschnittansicht) einer DLMC-Struktur kombiniert mit einer PPL-Platte; (c) DBR-PCL-Struktur.

Um eine Fernfeld-Superlinse mit plasmonischen Metaoberfläche zu erhalten, werden in dieser Arbeit zwei Designs diskutiert, wie die Abb. K.1 zeigt. Das Arbeitsprinzip der kaskadierten Superlinse basiert auf dem von Ma et al. [4, 28, 29] vorgeschlagenen Konzept zur Realisierung einer Superauflösung im Fernfeld durch separate Kopplung der evaneszenten Wellen und Kompression des Transversalwellenvektors. In dieser Arbeit werden zwei plasmonische Elemente in einer kaskadierten Superlinse verwendet, um die erforderlichen Funktionen zu erfüllen: zur Kopplung der Nahfeld-Information, eine Doppelschicht Mäander Struktur (DLMC) für das ursprüngliche Design und eine integrierte Plankavitätslinse (DBR-PCL) mit verteilten Bragg-Reflektoren für das modifizierte Design. Bei der zweiten Komponente handelt es sich um eine planare plasmonische Linsenstruktur (PPL) zur Phasen -kompensation um die Bildvergrößerung zu realisieren. Die Fähigkeiten zur Abbildung von Subwellenlängen Details beider Designs werden in dieser Arbeit numerisch und experimentell demonstriert.

Die DLMC-Struktur wird im ursprünglichen Entwurf der kaskadierten Superlinse verwendet, da die Mäander-Schicht dabei hilft, die Arbeitsfrequenz, die zur Ausbreitung von hohen k -Wellen verwendet wird, zu verschieben, indem SPPs sowohl mit großer als auch mit kurzer Reichweite in den sichtbaren Wellenlängenbereich gefaltet werden. In der Simulation verwenden wir die Otto-Konfiguration [30], um evaneszente Wellen zu erzeugen, wie die schematische Darstellung in Abb. K.2(a) zeigt. Für eine flexible Steuerung der optischen Antwort und der Übertragung wird eine Doppelschichtstruktur anstelle einer einzelnen oder dreifachen Schicht

gewählt. Abb. K.2(b) zeigt die Dispersion der Nahfeldübertragung der DLMC-Struktur. Wir erkennen dort einen breiten Transmissionsbereich bei Frequenzen von 400 bis 500 THz, was zeigt, dass eine Übertragung von Nahfeldwellen bei großen räumlichen Frequenzen auftritt. Die Funktion der DLMC-Struktur ähnelt der einer Linse mit negativem Brechungsindex, die das Nahfeld des Objekts zum Nahfeld des Bildes koppeln und übertragen kann. Um das Bild in das Fernfeld zu übertragen, müssen wir eine Phasen-kompensation oder eine Vergrößerung bereitstellen. In der kaskadierten Superlinse wird dazu die PPL-Struktur verwendet.

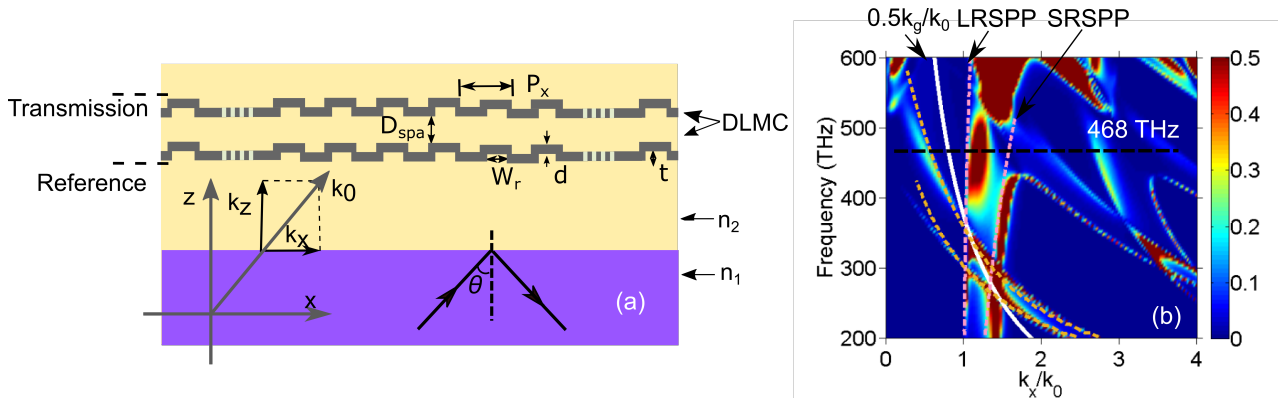


Abbildung K.2 (a) Schema für die Berechnung der Nahfeldübertragung einer DLMC-Struktur; (b) Transmissions-Dispersionsspektrum einer DLMC-Struktur mit: $P_x = 400$ nm, $d = 25$ nm, $D_{spa} = 70$ nm und $t = 50$ nm. Weiße Linie: $k_g/2k_0$. LR- und SR-SPP: Plasmon-Polariton mit großer bzw. kurzer Reichweite.

Das Design des PPL basiert darauf, dass sich SPPs in schmalen Schlitzen in einem Wellenleitermodus ausbreiten und dort die Wellenausbreitungskonstante von der Schlitzgröße abhängt [28, 31–34]. Die Phasenkompensation wird erzeugt, indem einfallendes Licht Nano-Spalte unterschiedlicher Strukturparameter durchläuft. Die Strukturparameter können so gestaltet werden, dass sie die Wellenfront des Lichts so modulieren, dass eine Brennweite von einigen Mikrometern erweitert wird, wie in Abb. K.3 gezeigt wird. Die PPL-Struktur allein eignet sich allerdings nicht zum Abbilden, wenn die PPL-Struktur in das Nahfeld eines Objekts gebracht wird. Wenn es jedoch mit der DLMC- (oder DBR-PCL-) Struktur kombiniert wird, kann das Streulicht unterdrückt werden (Abschnitt 4.4.1).

Zur Untersuchung des Abbildungsverhaltens der kaskadierten Superlinse mittels Simulation wird ein in einer Chromschicht eingebrachter Doppelschlitz mit einer Spaltbreite von 100 nm als Objekt verwendet. Die Dispersion der kaskadierten Superlinse wird, dann benutzt, um die Abbildung des Objekts im Idealfall zurechnen. Anschließend wird mit Hilfe des Softwarepakets "MicroSim", basierend auf der rigorosen gekoppelten Wellenanalyse (RCWA), die laterale Auflösung der kaskadierten Superlinse und die Optimierung der Strukturparameter berechnet. Ein Beispiel für die Simulationsergebnisse ist in Abb. K.4 gezeigt. Die Größe des Objekts in Abb. K.4(b) ist 200 nm. Wenn wir $z = 470$ nm als Bildebene nehmen und die normalisierte

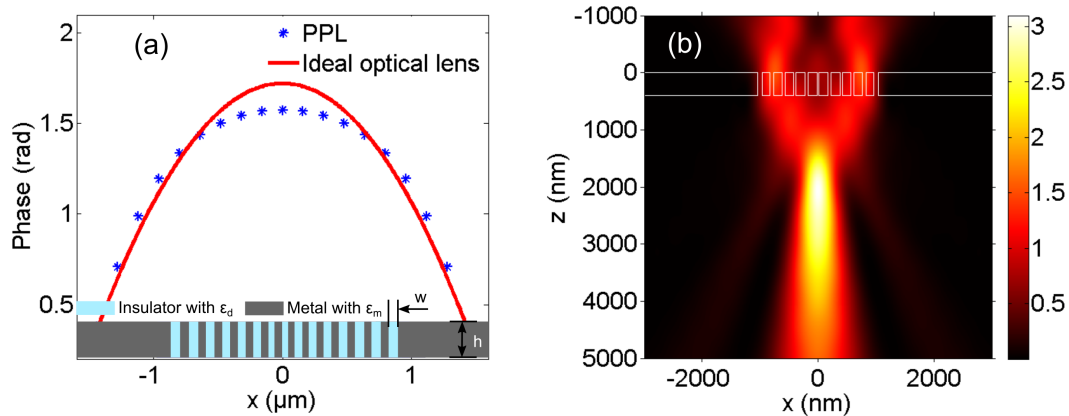


Abbildung K.3 (a) Phasenkompensation der mit Microsim berechneten PPL-Struktur mit einer Schlitzbreite von 88, 57,5, 47,5, 42, 34, 42, 47,5, 57,5, 64 und 88 nm, einer Schrittweite von 200 nm und einer Höhe von 400 nm; (b) Fokussierung einer ebenen Welle mit einer Wellenlänge von 640 nm einer PPL-Struktur.

Intensitätsverteilung in der Bildebene nach dem Rayleigh – Kriterium auftragen, beträgt die laterale Auflösung der kaskadierten Superlinse 180 nm bei der Wellenlänge von 640 nm, was fast $\frac{1}{4}$ der einfallenden Wellenlänge entspricht.

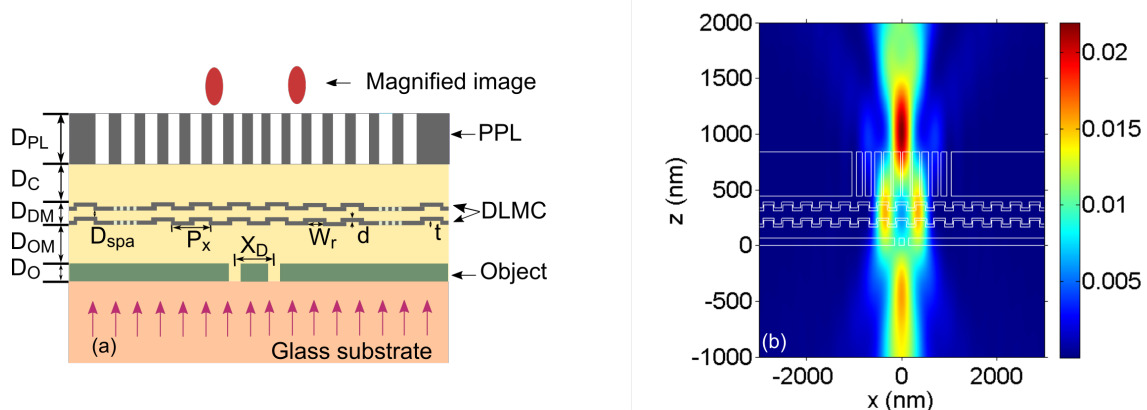


Abbildung K.4 (a) Schema der kaskadierten Superlinse mit einem Doppelschlitz als Objekt; (b) Feldverteilung, abgebildet durch die kaskadierte Superlinse für Objekte mit $w = 100$ nm und $X_D = 200$ nm. Simulationsparameter (nm): $D_{PL} = 400$, $D_C = 50$, $D_{DM} = 210$, $D_{OM} = 70$, $D_O = 100$, $D_{Spa} = 70$, $P_x = 400$, $W_r = 200$, $d = 25$ und $t = 50$.

Mit den durch die Simulation optimierten Parametern wurden kaskadierte Superlinsen hergestellt, um experimentell ihre Abbildungs-Fähigkeit zu demonstrieren. Als Vorbereitung für die abschließende experimentelle Verifikation wurden zwei Unterstrukturen (DLMLC- und PPL-Struktur) getrennt hergestellt und charakterisiert, um sicherzustellen, dass ihre optische Antwort in Übereinstimmung mit der Simulation ist. Der Querschnitt der DLMLC-Struktur wurde mit einem Rasterelektronenmikroskop (SEM) überprüft, das übertragene Spektrum mit der

Fourier-Transformation-Infrarotspektroskopie gemessen. Der Spot der PPL-Struktur bei einer Wellenlänge von 640 nm wurde mit einem Aerial-Scanning-Mikroskop überprüft. Die erhaltenen Ergebnisse zeigen, dass wir die Strukturen mit unseren Nanofabrikationsanlagen präzise nach dem Design herstellen können. Anschließend werden die zwei Unterstrukturen aufeinander gestapelt, um eine vollständige Superlinse zu erhalten. Das SEM-Bild ist in Abb. K.5 gezeigt.

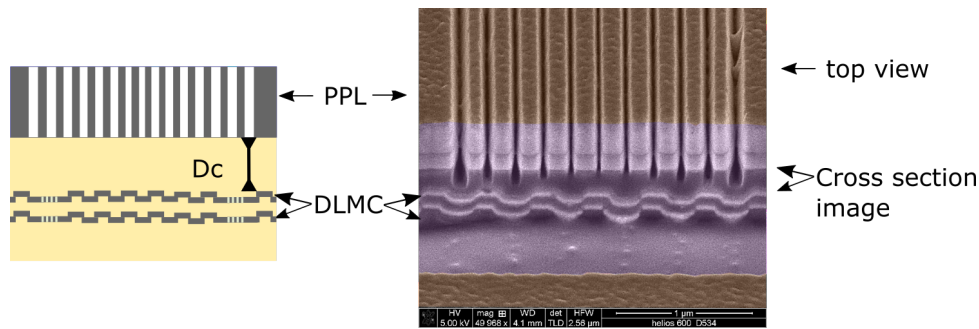


Abbildung K.5 Querschnitt einer kaskadierten Superlinse, hergestellt auf einem Glassubstrat ($D_c = 100$ nm).

Um experimentell die laterale Auflösung der kaskadierten Superlinse des ursprünglichen Designs mit der DLMLC-Struktur zu vergleichen, wurden zwei Unterstrukturen auf einem Objekt gestapelt. Die Doppelschlitze mit unterschiedlichen Größen wurden zuerst ohne die kaskadierte Superlinse gemessen, um die laterale Auflösung unseres konventionellen Mikroskops bei der Wellenlänge von 640 nm zu testen. Die erhaltenen Ergebnisse zeigen, dass das Objekt mit einer Spaltbreite von 100 nm und einer Objektgröße bis 300 nm mit dem konventionellen Mikroskop nicht aufgelöst werden kann. Erst bei einer Objektgröße von 400 nm ist eine konventionelle Abbildung möglich, was gemäß der Simulation einer lateralen Auflösung von 360 nm entspricht. Anschließend wurde die kaskadierte Superlinse auf dem Doppelschlitz-Objekt mit unterschiedlich Schlitzabstand aufgebracht, um die Abbildungseigenschaften zu testen. Zuerst wurde ein Doppelschlitz mit einem Spaltabstand von 800 nm und einem Spaltbreite von 400 nm verwendet, um die übertragene Intensitätsverteilung und Bildgröße der kaskadierten Superlinse mit der Simulation zu vergleichen. Dann wurde die Größe des Spaltobjekts bis auf 180 nm verkleinert. Das Bild des Objekts ohne die kaskadierte Superlinse, wie in Abb. K.6(d) gezeigt, verschmilzt zu einem einzelnen Schlitz. Mit kaskadierten Superlinsen auf dem Objekt, wie in Abb. K.6(b) gezeigt, kann mit Hilfe eines herkömmlichen Mikroskops ein aufgelöstes Bild gewonnen werden (Abb. K.6(e)). Wenn wir die Intensitätsverteilung entlang der gestrichelten Linie auftragen und mit der Simulation vergleichen, können wir sehen, dass die gemessene Bildgröße gut übereinstimmt. Mit den erhaltenen Ergebnissen können wir die Schlussfolgerung ziehen, dass die Fähigkeit zur Superauflösung der kaskadierten Superlinse numerisch und experimentell demonstriert wurde. Die kaskadierte Superlinse wurde im Rahmen dieser Arbeit erfolgreich

gefertigt, wobei eine laterale Auflösung bei einer Wellenlänge von 640 nm von 180 nm erreicht wurde.

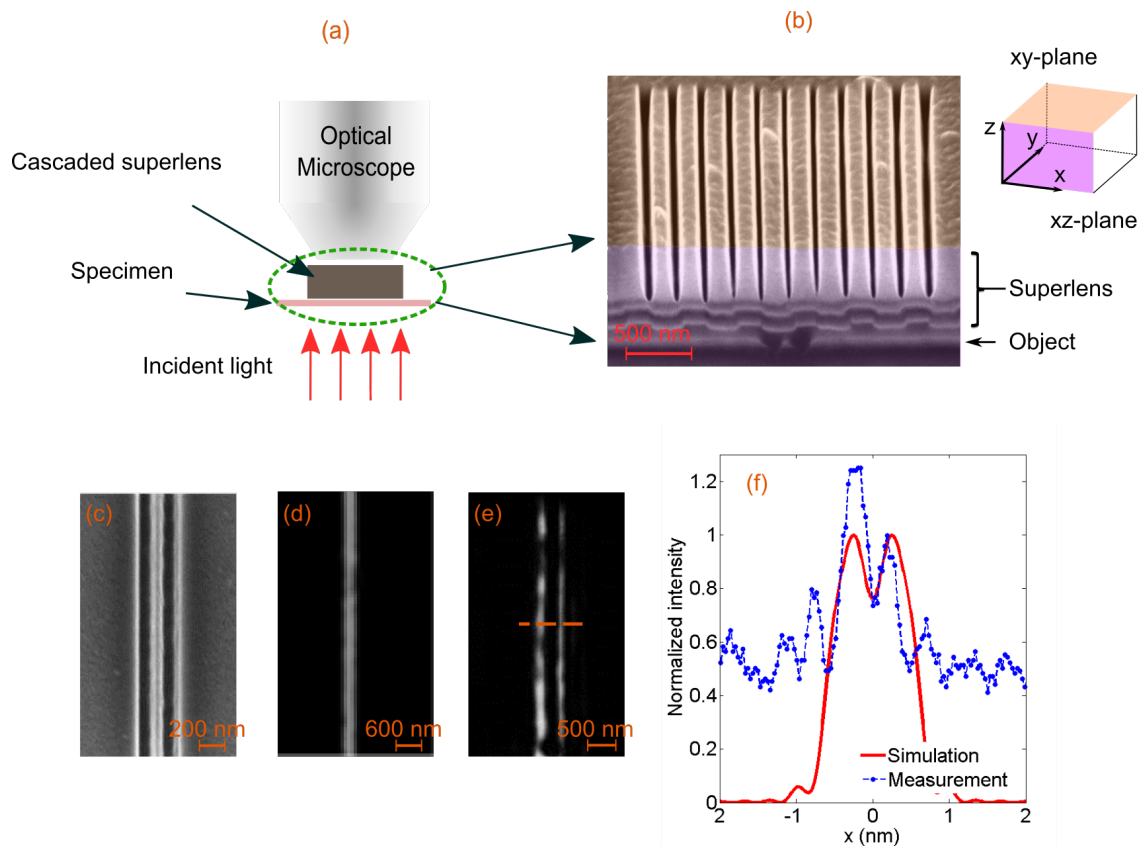


Abbildung K.6 (a) Schema eines Subwellenlängen-Abbildungssystems, bestehend aus einer kaskadierten Superlinse und einem herkömmlichen Mikroskop für die direkte Bildgebung im Fernfeld; (b) Querschnitt der Superlinse, die auf dem Objekt mit einer Breite von 100 nm und einer Objektgröße von 180 nm hergestellt wurde; (c) SEM-Bild des Objekts mit einer Breite von 100 nm und einer Objektgröße von 180 nm von Mitte zu Mitte; (d) Bild des Objekts unter einer herkömmlichen Mikroskopie; (e) Bild des im Fernfeld erhaltenen Objekts mit Hilfe der kaskadierten Superlinse; (f) Vergleich zwischen Simulation und Messung: Simulation, die aus der Abbildung im Kapitel 4, und Messdaten, die in (e) gestrichelt gezeichnet sind.

Bei dem experimentellen Vergleich erkennt man, dass die maximalen Bildintensitäten für die beiden Schlitze unterschiedlich sind, was durch die Ausrichtung des Objekts zur periodischen Mäanderstruktur erklärt werden kann. Um das Problem zu lösen, kann die ursprüngliche kaskadierte Superlinse modifiziert werden, indem eine planare Hohlraumlinse (PCL) verwendet wird, um die DLMC-Struktur zu ersetzen. Um eine Arbeit-Wellenlänge im sichtbaren Bereich zu erhalten und die Nahfeldübertragung zu verbessern, wurde verteilte Bragg-Reflektoren (DBR) in die plasmonische Kavität um das Linsenzentrum integriert, die zusätzliche laterale Hohlräume für Oberflächenwellen bilden. Ein Schema der kaskadierten Superlinse mit dem modifizierten

Design ist in Abb. K.7(a) gezeigt. Sowohl die Simulationen (Abschnitt 7.1) als auch die experimentelle Verifizierung (Abschnitt 7.2) wurden unter Verwendung des gleichen Verfahrens, wie für die ursprüngliche Superlinse durchgeführt. Die Ergebnisse zeigen, dass mit geeigneten Parametern die Dispersion der DBR-PCL-Struktur in einem breiteren Frequenzbereich (von 350 bis 700 THz) und innerhalb eines größeren Bereichs des transversalen Wellenvektors erzielt wird. Wird die DBR-PCL-Struktur mit der PPL-Struktur über den Schlitz gestapelt, kann man das Abbildungsverhalten der modifizierten kaskadierten Superlinse untersuchen. Die Simulationsergebnisse zeigen, dass die kaskadierte Superlinse mit dem modifizierten Design gut funktioniert. Das kritische Ausrichtungsproblem zwischen dem Objekt und der Mäanderstruktur ist beseitigt. Die Linse wurde hergestellt, die laterale Auflösung des modifizierten Designs bei der Einfallswellenlänge von 640 nm betrug 200 nm. Darüber wurden experimentelle Verifikationen mit einer relativen Positionsverschiebung zwischen dem Objekt und der DBR-PCL-Struktur durchgeführt. Die erhaltenen Bildintensitäten sind in Abb.K.7(b) gezeigt. Die kaskadierte Superlinse mit dem modifizierten Design funktioniert gut durch die Lösung des Problems der kritischen Ausrichtung. Zusätzlich bietet das modifizierte Design die Möglichkeit, die Superlinse aufgrund ihrer breiten spektralen Antwort innerhalb eines größeren transversalen Wellenvektors mit Weißlicht zu verwenden.

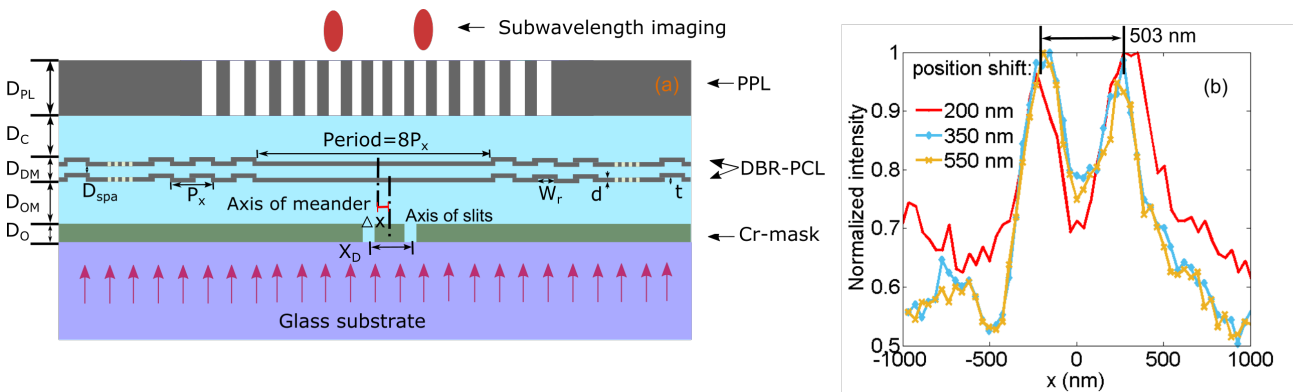


Abbildung K.7 (a) Schematische Darstellung der kaskadierten Superlinse mit dem modifizierten Design; (b) Normalisierte Intensitätsverteilung der erhaltenen Bilder mit relativen Positionsverschiebungen zwischen der PPL- und der DBR-PCL-Struktur. Die optimierten Strukturparameter: $D_{PL} = 400$, $D_C = 40$, $D_{DM} = 320$, $D_{OM} = 160$, $D_O = 100$, $D_{Spa} = 100$, $P_x = 400$, $W_r = P_x/2 - d$, $d = 30$ und $t = 70$ (Einheit: nm).

Unsere Ergebnisse zeigen, dass das Konzept, eine Fernfeld-Superlinse mit räumlich getrennter Wellenkopplung und Bildvergrößerung zu realisieren, funktioniert. Die experimentellen Ergebnisse stimmen gut mit den Simulationen überein, was das Ergebnis einer präzise kontrollierten Herstellungsprozedur ist. Die erfolgreich hergestellten Nanostrukturen ebnen den Weg für die weitere Herstellung von Strukturen ähnlicher Größe (z. B. dünner metallischen Schichte auf Mäanderstrukturen).

Folgende Veröffentlichungen wurden im Rahmen der Promotion publiziert:

- Li, Huiyu, Liwei Fu, Karsten Frenner, and Wolfgang Osten. "Cascaded plasmonic superlens for far-field imaging with magnification at visible wavelength." *Optics Express* 26, no. 8 (2018): 10888-10897,
- Li, Huiyu, Liwei Fu, Karsten Frenner, and Wolfgang Osten. "Cascaded DBR plasmonic cavity lens for far-field subwavelength imaging at a visible wavelength." *Optics Express* 26, no. 15 (2018): 19574-19582,
- Li, Huiyu, Liwei Fu, Karsten Frenner, and Wolfgang Osten. "Nanofabrication results of a novel cascaded plasmonic superlens: lessons learned." *Proc. SPIE*, vol. 10330, (2017): 103300Y.

1 Introduction

With the development of nanoscience and technology, improving the lateral resolution of optical microscopes becomes highly demanded. However, the resolving power of a conventional optical microscope is limited by Abbe diffraction, which is approximately half of the incident wavelength. To improve the resolution, a variety of efforts have been devoted to imaging objects with subwavelength features. There are no reports yet regarding far-field plasmonic superlenses to directly obtain an image at visible wavelength.

In this dissertation, a novel cascaded plasmonic superlens is studied based on an idea to couple and amplify near-field evanescent waves at visible wavelengths and to transfer the evanescent waves to propagating waves achieving a super resolving power in the far field. Both numerical simulation and experimental verification will be illustrated to demonstrate subwavelength imaging capability of the design. Afterwards, the novel cascaded superlens was modified based on the obtained results of the original design to diminish an alignment problem between the lens and the object.

In chapter 2, a brief review of subwavelength imaging methods and related working principles are given. We have analyzed advantages and disadvantages of existing subwavelength imaging methods including those with scanning or post-processing, metalenses and plasmonic superlenses. To directly observe an image with super resolution in the far field, a cascaded superlens was suggested early in our group [35] based on the concept to couple waves at higher spatial frequencies and to compress the information by using two separate plasmonic elements.

In chapter 3, we introduce the idea and two basic designs of the cascaded superlens consisting of a double layer meander cavity (DLMC) structure or a simple plasmonic cavity lens (PCL) integrated with distributed Bragg reflectors (DBRs), combined with a planar plasmonic lens (PPL). The cascaded superlens is aimed to couple and compress the evanescent waves to propagating waves, so that the information of high spatial frequencies can be detected in the far field. Furthermore, an in-house developed software package Microsim based on rigorous coupled wave analysis is briefly introduced.

In chapter 4, simulation results about the lateral resolution of the cascaded superlens are presented. Near-field interactions between the two structures and their influences are briefly discussed. The simulation results show that a lateral resolution of 180 nm can be achieved with the cascaded superlens when an incident wavelength of 640 nm is used, the resolving power of which is better than $\lambda/3$. Furthermore, the tolerance of structural parameters for the cascaded superlens are discussed.

In chapter 5, preparations for the experimental verification are discussed. We first give a brief introduction to the fabrication and characterization facilities. The fabrication process is complicated due to a variety of geometrical parameters for different structures. Deposition of thin metallic films on a structured surface and the structring of nano-slits with high aspect ratio are challenging. Before fabrication of the whole structure, each fabrication process was tested and optimized separately to ensure the optical responses of the fabricated superlens approaching the numerical results.

In chapter 6, experimental verification of the cascaded superlens is illustrated. To explore the lateral resolution of the cascaded superlens, a pair-slit in a chromium layer is used as an object. The fabricated slit objects are first measured under a conventional microscope, then the cascaded superlens is stacked on top of the slit object. The lateral resolution of 180 nm at the wavelength of 640 nm as in the simulation is achieved with the fabricated cascaded superlens. Furthermore, the measured results are compared with the simulations. The comparison shows a good agreement between the two. We have also fabricated objects with varying sizes and analyzed reasons for the distortion of the obtained image, which is due to an alignment problem between the object and the DLMC structure. The critical alignment requirement limits the application of the cascaded superlens with the original design containing the DLMC structure, therefore a modified design is necessary.

In chapter 7, the modified design based on the obtained results of the originally designed cascaded superlens is presented to overcome the alignment challenge of the cascaded superlens with the original design. For the modified cascaded superlens, we use a planar cavity lens integrated with distributed Bragg reflectors to replace the DLMC structure. In numerical simulations, we consider first physical properties of the modified superlens, and then numerically optimize the structural parameters. The cascaded superlens with a modified design was fabricated and characterized, which achieves a lateral resolution of 200 nm at the wavelength of 640 nm, a similar resolving power as with the original design. Moreover, the obtained results show that the modification to the cascaded superlens efficiently solves the alignment problem of the cascaded superlens with the original design.

In chapter 8, main achievements in this dissertation are summarized and a short outlook on future work in developing a cascaded superlens is given.

2 State of the art in resolution enhanced imaging

With the development of nano-science and technology, improving the lateral resolution of optical microscopes becomes highly demanded [36–38]. Varieties of efforts have been devoted to improving it [36, 39, 40]. In this chapter, a brief introduction is given to these methods, including several pointillistic imaging superresolution techniques, plasmonic superlenses, and other methods developed recently.

2.1 Resolution limit of conventional microscopes

According to the Abbe diffraction limit published in 1873 [41, 42], the resolving power of a conventional optical microscope is limited by light diffraction, which is approximately half of the incident wavelength

$$d_{res} = \frac{\lambda}{2n \sin \theta} = \frac{\lambda}{2NA}. \quad (2.1)$$

In this equation, d_{res} is the resolvable feature size, λ is the observation wavelength, n is the index of refraction of the surrounding medium, θ is the half-angle subtended by the optical objective lens, and $NA = n \cdot \sin(\theta)$ is the numerical aperture of the lens. For instance, when $\lambda = 640$ nm, the highest lateral resolution for a conventional microscope in air is 320 nm in ideal case. The resolution can be improved according to the E.q. 2.1. A general method to increase NA is immersing the lens and objects in oil [43], and the largest commercial NA of an immersion lens is around 1.6 [44]. There are still other methods to increase NA including 4Pi-microscopy to utilize the full angular spectrum [45]. Other than varying wavelength or NA, decreasing the focus size of incident wavelength [46], collecting evanescent wave [5] or imaging processing [47] have also been suggested to improve the lateral resolution.

2.2 Superresolution with scanning or post-processing

One of the earliest applied methods to realize superresolution, which breaks Abbe diffraction limitation, is structured illumination microscopy (SIM) pioneered by Tony Wilson [48]. SIM relies on a grid pattern resides in one of the illumination apertures to generate a sinusoidal excitation wave field. The interference of diffraction orders superimposed on the specimen is captured at the image plane. By shifting or rotating the grid pattern in steps between the capture of each image set, information can be extracted and an image is then constructed. Nevertheless, the maximum resolution of the SIM achieves typically a twofold lateral resolution enhancement with an axial resolution ranging between 150 and 300 nm at visible wavelength [36, 49]. Furthermore, more than one frame of images are required at different orientation angle of the grid to generate one image subset [50]. With nonlinearity arising from the saturation of the excited state of a saturated structured-illumination microscopy, the resolution has been improved to less than 50 nm [51]. The technique of SIM has already been extensively implemented for standard commercial wide field microscopes.

Considering the object as a branch of separate points, superresolution can be realized by pointillistic collecting the information and precisely localizing each individual molecule in a sample, e.g. scanning near-field optical microscopy (SNOM), or stimulated emission depletion (STED) as the schematic of the imaging principles shown in Fig. 2.1 (b) or (c).

By the SNOM, near-field information is collected point-by-point using an detecting tips with a diameter smaller than the excitation wavelength [49]. In this case, the resolution of the obtained image is usually limited by the diameter of tip. For instance, when diameter is 150 nm, an average of 100-nm-spaced object can be distinguished [52]. Efforts have been devoted to improving the SNOM with polarized light [53], metal-coated fiber tips [54] or dual-scanning [55]. However, the SNOM assumes the high risk of damaging the sample or the tip due to the short distance between them, and the low scanning speed makes it time-consuming to obtain a single image.

STED realizes superresolution by altering the excitation beam using a second doughnut-shaped laser. Through bleaching the excitation back to the ground state, only molecules in the center of the doughnut beam are able to emit fluorescence, therefore improves the resolution. For a dye with an average emission wavelength of 400 nm, the full width half maximum of a beam is predicted to be reduced to 35 nm [56]. With a yellow fluorescent protein tag, resolution for 3D better than 50 nm inside the living cell was achieved [57]. In addition, stimulation emission double depletion (STEDD) further improves the resolution to $1/5 \lambda$ by repeating the bleaching second time [58, 59]. However, the STED (or STEED) scans the image point by point with

a frame rate of 10 s, therefore is time-consuming and during the movement, a slight position shift influences the image quality as well [57].

In contrast, full-field superresolution methods, such as stochastic optical reconstruction microscopy (STORM) and photo activated localization microscopy (PALM), utilizing photo switchable [58, 60, 61] or photo activated fluorophores [62–64] methods, have been developed in the past decades. The fluorophore groups are randomly activated by illumination causing them to emit light of longer wavelengths under different mechanisms, which makes it to be a non-linear imaging system different from a conventional microscope. Therefore, individual molecule in a sample is precisely localized and recorded in multiple frames. Hundreds of individual images and post-processing are needed in the two methods to obtain a single image. STORM is capable of imaging biological structures with a resolution of 20 nm [61] or 60 nm for a 3D imaging [60]. The fluorescence image is constructed from individual fluorescent molecules that are switched on and off under light of different colors. The resolution of the technique is limited in principle only by the number of photons emitted per switch cycle, but not the wavelength of light. PALM makes it possible to investigate nanoscale dynamic living cells [62]. The effectual time of the fluorophores is increased to 25 min under physiological conditions with spatial resolutions down to 60 nm but frame rates of 25 s [63]. However, the STORM or PALM are only capable for molecular and cell biology imaging and the use of chemi-luminescent has a risk of pollution to sample.

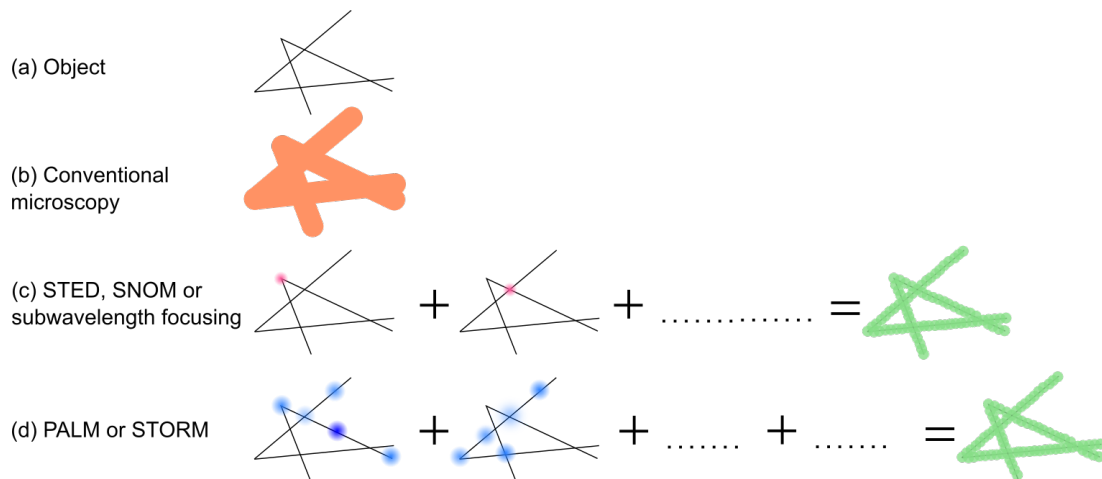


Figure 2.1 Principles of sub-wavelength imaging with scanning: (a) Schematic of an object; (b) Image under a conventional microscope; (c) Imaging principle of methods with sub-wavelength focus point; (d) Imaging principle of PLAM or STORM with Gaussian fit [36].

Other kinds of far-field superlens or far-field subwavelength imaging methods have been suggested or demonstrated based on point spread function engineering, including a metal slab structured on one side with subwavelength grating [11, 22], structured near-field illumina-

tion [23–25], sparse-reconstruction [65], or selective excitation of localized surface plasmons [26, 27]. For these methods, the resolution is influenced by the relative position of the object.

Nevertheless, these methods require post-processing or scanning, which are beyond our consideration.

2.3 Metalenses, microsphere and other methods

With the development of artificially structured metamaterials, a novel type of lens for imaging with enhanced resolution appeared. A series of attractive metalenses with planar shape has been reported by the group of professor Capasso [66–69]. The lenses were made from nano-structured dielectric films with high refractive index. The periodical distributed nano-structures, in a shape of circular pillars, fins or rectangles, retards phase distribution of incident light. The metalens is a far-field lens and manifests a great potential for flat and compact designs of optical element with flexible phase retardation. Different from the sub-wavelength imaging with scanning, these structures have the same function as a conventional lens but in a planar shape. Theoretically, the flat metalens is free from spherical aberrations [68]. However, the achieved lateral resolution of the metalens is only $3/4$ of the incident wavelength, which is not as good as other reported results.

A microsphere is considered as a promising dielectric lens for superresolution because of a subwavelength focusing point [70, 71] or total reflection [72]. The working principle of a microsphere to enable subwavelength resolution has not reached an agreement but experimental results show that it works well in subwavelength imaging. The resolution of a microsphere is related to the material and sizes, and a resolution of 220 nm at $\lambda = 600$ nm depends on a barium titanate sphere with diameter of $6 \mu\text{m}$ is reported in [73]. The advantage of a microsphere lens is that it can be used under white light: e.g. SiO_2 microsphere with a diameter of $5 \mu\text{m}$, the lateral resolution is about 100 nm (object: 50 nm pores in diameter and spaced 50 nm apart) [74]. However, view field of a microsphere is limited [75] and the imaging quality of a microsphere is related with the observing ways e.g. immersion or semi-immersion [70].

Very recently, dielectric meta-surfaces [64] and microspheres [76] with subwavelength focusing was demonstrated with potential for scanning imaging. The method is also based on scanning principle similar to STED, but with a different mechanism to decrease the size of the illumination beam. For these scanning or post-processing based imaging method, though the performance of computers is largely improved, an operation time is still required and image cannot be presented in real-time.

2.4 The plasmonic superlens

The basic principle of a plasmonic superlens is to utilize the evanescent wave by left-hand material or dispersion engineering through nano-structured metallic materials [13, 77–79]. A representative example is negative refractive index metallic material (NIM): with $n = -1$, a perfect near-field subwavelength imaging can be realized [5]. The major limitation for NIM is that the material is unavailable in nature. By combining metallic strips and split ring resonators, NIM at microwave frequency was first demonstrated in 2001 [80]. However, these materials suffer from a high loss which is mainly induced by the magnetic resonances responsible for the negative permeability. For instance, in a recently optimized stacked mesh structure, an index of $-1.23 + 0.34i$ at $\lambda = 1.775 \mu m$ was achieved, which is still absorptive [81] and only 0.1 % is left. Moreover, the working wavelength is restricted to range of microwave or infrared.

As an alternative for the NIM, materials with negative permittivity or structures with nano-scale features were further studied [9, 82–88]. A thin layer of noble metal film can already work as a near-field superlens as a result of its negative permittivity [7, 89]. Experimentally, a grating with 60 nm half-pitch and an object with 40 nm line width was imaged through a 35 nm silver slab at $\lambda = 365 \text{ nm}$ [84].

Artificial anisotropic media composed of multi-layer dielectric/metallic stacks [7–10] utilizing surface plasmon polaritons [84, 90, 91] has a similar function to propagate evanescent wave: with a proper design, the dispersion of the light in the medium becomes hyperbolic. Plasmonic superlenses have been envisioned as a promising device for real-time subwavelength imaging [6, 38]. The permittivities can be estimated using the effective medium theory [6, 11].

Nevertheless, the image has the same size as the object and remains at the near field behind the lens and cannot be propagated to the far field. To transfer the information to the far field, metallic wire arrays were proposed [37, 39, 67, 92–96]. Take nanolens consisting of aligned gold nanowires embedded in a porous alumina matrix as an example, the transport distance were increased to 6 times of the incident wavelength with a lateral resolution of $1/4$ incident wavelength [97]. The propagation distance increased, but still limited by the length of nanowires. The resolution is decided to the size of nanowires and distance between them. However, the working wavelength is still in infrared range.

Another concept to realize a subwavelength imaging is using a metamaterial namely the classical metalens with a typical periodical array of split rings [26, 98, 99]. The location of the object can be identified when it is coupled with the rings. However, the optical losses is high due to the magnetic resonances and the application wavelength is limited in microwave and infrared range.

To collect the information with high spatial information in the far field, slanted gratings were proposed [22, 100, 101]. The diffraction grating leads to a one-to-one relationship between the far-field and the near-field angular spectra, which makes the device suitable for imaging beyond the diffraction limit and far-field measurement: the information at each order can be converted to the responding spatial-frequencies and a resolved image can be reconstructed with post-processing. The numerically reported resolution is 40 nm lines with a 30 nm gap at $\lambda = 376$ nm.

The concept of a far-field optical superlens was first proposed by Liu et al [11]. The superlens is a combination of a thin layer of poly and plasmonic gratings. The optical transfer function is designed for p-polarization and the zeroth order light is suppressed to enhance the diffracted first-order. Hence, the evanescent wave band can be mapped unambiguously into the propagating wave band in the far field. Lateral resolution of the superlens is about 120 nm at $\lambda = 377$ nm. However, its working wavelength is still limited at ultra violet and the reported image is constructed by both s- and p-polarized light.

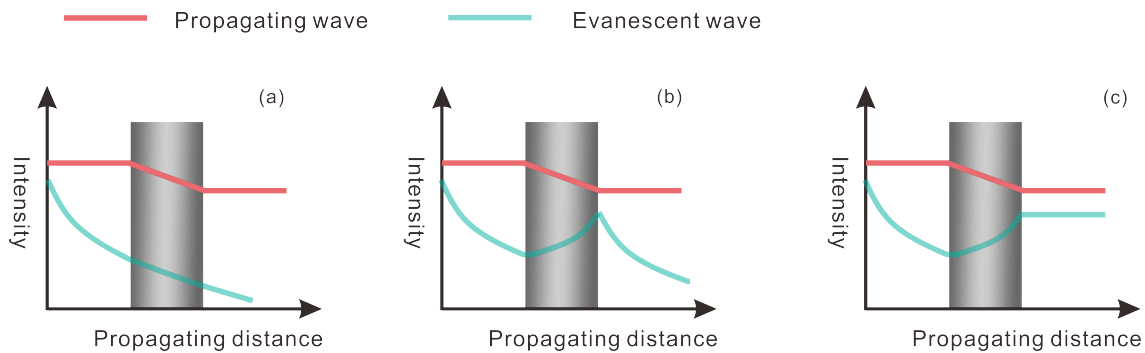


Figure 2.2 Principle of lenses: (a) Conventional lens; (b) Near-field superlens [5]; (c) Far-field superlens [4].

Other than far-field subwavelength imaging with post processing, the near-field optical waves can also be coupled to form a propagating field through artificially designed metamaterials, hyperlenses, of which the near-field image is magnified with the light propagation through the multiple layers [2, 11–13]. A series of experiments have validated the concept of cylindrical or spherical hyperlens [2, 102, 103]. Cylindrical hyperlens was first designed for one-dimensional imaging working at violet or ultraviolet range, which is composed of conformal 16 layers' deposition of Ag and Al_2O_3 on a cylindrical curved surface. The lens can realize resolution of a 150 nm-pitched slits with width of 40 nm nearly 1/3 of the incident wavelength $\lambda = 365$ nm [11, 103], which is the best experimental results of hyperlens at present. Although simulated results show that the working wavelength can be shifted to visible range [104], or theoretically lateral resolution can be as good as 5 nm [12] but there is no validated experimental results. However, it was demonstrated very recently that the multilayer structures have fundamental

limitations for imaging because the image resolution is decreased with the number of layers due to increased loss and the suppression of large spatial frequencies [3].

Based on the results of one-dimensional hyperlens, a spherical hyperlens was designed to work at visible wavelength range for two-dimensional super-resolution [2]. The lens used a higher refractive index material i.e. Ti_3O_5 to replace Al_2O_3 and the object with a feature down to 160 nm was clearly resolved at the wavelength of 410 nm. View field is limited by the radius of the cylindrical- or spherical- hyperlens, therefore the object has to be placed inside the cavity. Moreover, more than 98 % of the incident light is lost, which is induced by a stack of alternative metal and dielectric films. Its application is highly restricted.

Alternatively, a metal slab with a periodic surface corrugation was proposed for far-field sub-wavelength imaging [11]. The imaging is realized by coupling the information of high transverse vectors to lower ones through different diffraction orders of the corrugation film. Due to an incomplete wave transformation in terms of spatial frequency, the image needs to be reconstructed through combining both s- and p-polarized waves. Furthermore, the lens works only at a wavelength close to the surface plasmon frequency of the metal, which is ultraviolet in the case of silver, the metal of which is also used in this dissertation.

To directly obtain an image with super-resolution in the far field, cascaded plasmonic super-lenses with two designs are numerically and experimentally studied in this dissertation. The designs are based on a concept suggested by Ma et al [4, 28, 29] to realize the function of enabling the propagation of the light with higher transverse wave vectors and compressing high wave vectors in the metamaterial to lower wave vectors separately. The concept suggested by Ma is only numerically studied due to the absence of materials with the desired dispersion.

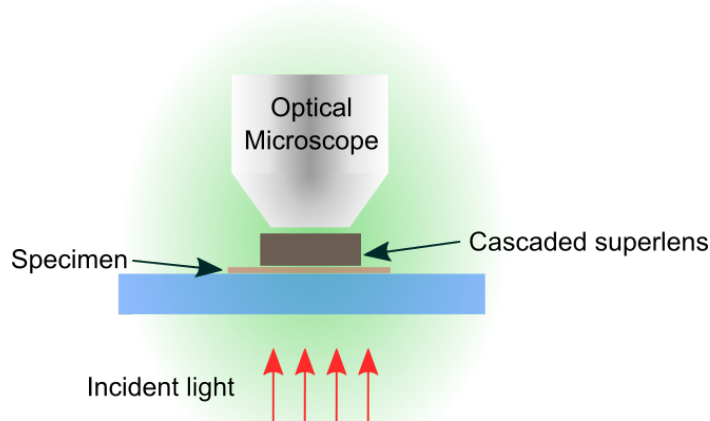


Figure 2.3 Schematic of a subwavelength imaging system consists of a cascaded superlens and a conventional microscope for direct imaging in the far field.

In this dissertation, a double layer meander structure or a planar cavity lens integrated with a distributed Bragg reflectors is used as the assumed metamaterial for couple and propagation of the evanescent waves carrying information of subwavelength features, which can be realized with existing nano-fabrication technology. A planar plasmonic lens is aim for phase compensation and magnification to convert evanescent waves into propagating ones. The two sub-components are stacked together to achieve a cascaded superlens which is used for directly obtain a far-field image with resolution beyond the Abbe diffraction at visible wavelength with less optical loss and a planar view field. The far-field image can be further magnified with a conventional microscope as shown by the schematic in Fig. 2.3.

3 Design and working principle of a cascaded plasmonic superlens

From the view point of Fourier optics, the reason for resolution limitation of conventional microscopes is the lost of evanescent waves, which carry the subwavelength information of an object but vanish exponentially with propagating. Therefore, to improve the imaging resolution, the question becomes how we can couple the evanescent waves into a lens system.

3.1 Introduction to the new design and its advantages compared to existing plasmonic superlenses

In this section, we will briefly explain our route for far-field subwavelength imaging and the basic working principle of a cascaded plasmonic superlens, discuss its novelties compared with the existing plasmonic superlenses, and introduce the simulation method used in this dissertation.

3.1.1 The new design of a cascaded superlens

The cascaded superlens is designed for far-field subwavelength imaging at visible spectrum, which can be combined together with a conventional microscope as shown by the schematic in Fig. 3.1(a).

In the design, the cascaded plasmonic superlens is composed of two parts as shown in Fig. 3.1(b). The first part is a double layer meander cavity structure (DLMC). It is used to couple and amplify evanescent waves emanating from subwavelength objects. Its working wavelength can be tuned to visible spectrum by varying the geometrical parameters, and this be attributed to the interaction between surface plasmon polaritons from the two cavity layers and the Fabry-Perot cavity modes [35, 67]. Nevertheless, the DLMC structure can only transfer the near field information from near field to near field.

To transfer the near field image to the far field with a magnification, a planar plasmonic lens (PPL) consisting of a nano-slit array in a thick silver slab is employed due to its compact and planar design. Although the lens behavior of the PPL has been demonstrated almost decade ago [105?], it alone cannot be applied for near-field imaging due to its near-field interaction with object. In our design, however, the near field interaction is greatly suppressed when it is combined with the DLMC structure, which is going to be discussed in detail in subsection 4.1.1.

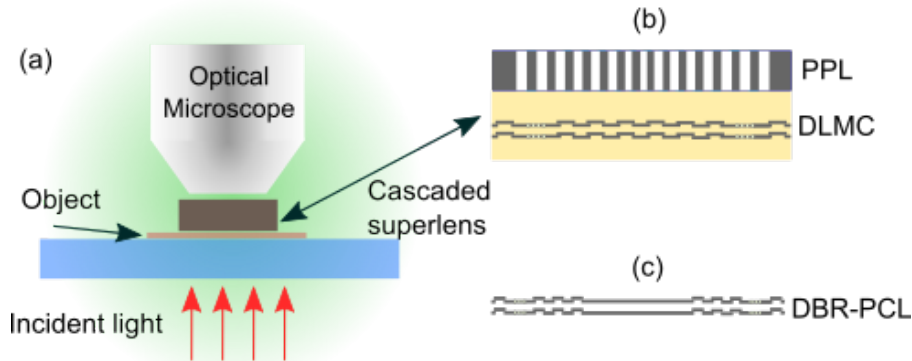


Figure 3.1 (a) Measurement setup for exploring subwavelength imaging using a far-field superlens combined with a microscope; (b) Schematics of the original design (Cross-sectional view) with a DLMC structure and a PPL slab; (c) The DBR-PCL structure as a replacement of the DLMC structure in the modified design.

Fig. 3.1(c) shows a plasmonic cavity lens integrated with a distributed Bragg reflector (DBR-PCL) structure, which is going to be discussed in detail in subsection 7.2.1.

3.1.2 Imaging with high spatial frequency information

When studying an imaging process with wave theory, angular spectrum representation is a powerful mathematical method to describe the optical field in a homogeneous medium. Assuming that a plane wave with a unit amplitude at wavelength λ propagates in the z -direction, its electric field at position z can be represented by:

$$E(x, y, z) = \iint_{-\infty}^{+\infty} E(k_x, k_y; 0) \exp[i(k_x \cdot x + k_y \cdot y + k_z \cdot z)] dk_x dk_y, \quad (3.1)$$

in which k_x, k_y, k_z are spatial frequencies along the x -, y - and z - directions, respectively. $E(x, y, z)$ satisfies the vector Helmholtz equation in free space (without source):

$$\nabla^2 E + k_0^2 E = 0, \quad (3.2)$$

in which $k_0 = \sqrt{k_x^2 + k_y^2 + k_z^2} = 2\pi/\lambda$ is the wave vector in space. When $k_z^2 = k_0^2 - (k_x^2 + k_y^2) \geq 0$, k_z is real, and the wave can propagate to the far field. However, when $k_z^2 = k_0^2 - (k_x^2 + k_y^2) < 0$, k_z becomes imaginary and the electric field amplitude decays exponentially with z . The wave is evanescent and is confined in the near field.

To illustrate the information of an object carried by evanescent waves and their influence on the image, we use a pair of slits with a slit-width of 100 nm and an object size of 200 nm to model it. The object size is defined as the slit distance from slit center to slit center. Such objects are also used for numerical calculations and experimental demonstrations in this dissertation. At an incident wavelength of 640 nm, the object is subwavelength and cannot be resolved in the far field by a conventional microscope. For current illustration, we use an one-dimensional rectangular function with a unit amplitude of E_x to model the object as shown by the black curve plotted in Fig. 3.2(a), the field of the object at $z = 0$ is defined as

$$E_1(x) = \begin{cases} 1, & \text{when } 50 \leq |x| \leq 150 \\ 0, & \text{otherwise} \end{cases} . \quad (3.3)$$

Its angular spectrum $E_1(k_x)$ in frequency space is the Fourier transformation of $E_1(x)$ as shown by the black curve in Fig. 3.2(b). We apply a near-field superlens with an ideal transfer function (TF) [106], which is defined as:

$$\text{TF}(k_x) = \begin{cases} 1, & |k_x| \leq mk_0, \text{ } m \text{ is a real number} \\ 0, & \text{otherwise} \end{cases} , \quad (3.4)$$

to the object. Without considering any other field interactions, the angular spectrum behind the lens $E_2(k_x)$ can be calculated as:

$$E_2(k_x) = \text{TF}(k_x) \cdot E_1(k_x). \quad (3.5)$$

The output fields of $E_2(x)$ with different TFs in real space are plotted in figure 3.2 (a). In free space, only the waves within the band of $|k_x| \leq k_0$ can propagate to the far field, under which condition the image degenerates to a single slit as shown by the red curve in Fig. 3.2(a) due to the lost of waves with high spatial frequencies.

When the waves within a larger band width, e.g. $|k_x| \leq 2.6k_0$, of the object are transferred by a superlens, the features of the two slits on the image plane are remained as shown by the blue curve in Fig. 3.2(a). Therefore, to resolve an object with a size of 200 nm, a near-field imaging lens with a TF spanning a bandwidth of $(-2.6k_0, 2.6k_0)$ is sufficient. The required bandwidth

of the transfer function for a resolvable image is related to the size of objects. For a smaller object, the TF with a broader passband is required to obtain a resolvable image.

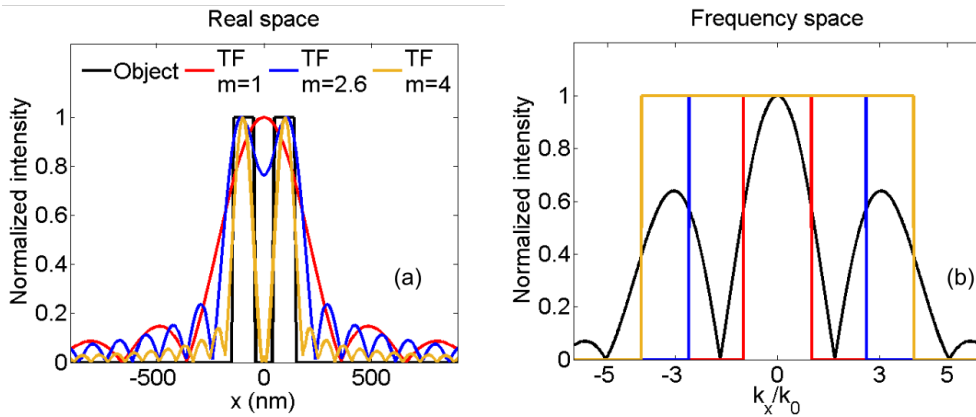


Figure 3.2 (a) Field distribution of a pair-slit object and its image distributions with different transfer functions in real space; (b) Angular spectrum of the object and different transfer functions.

To detect the subwavelength features in the far field, the high spatial frequency information of the evanescent waves is required to be transferred to the far field, e.g. by coupling them to propagating waves. When a phase compensation mechanism is applied to the superlens, which results in image magnification, the information carried by higher k_x can be compressed to lower one [28, 107, 108]. In this case, parts of evanescent waves are transferred to propagating ones. An example is shown in Fig. 3.3. The black curve in Fig. 3.3(a) is from the same object of that in Fig. 3.2, while the green curve is an image of the object magnified by a factor of 3. The slit-width and the object size are increased to 300 nm and 600 nm, correspondingly. If we compare the angular spectrum of the image with the one from the object as shown in Fig. 3.3(b), it can be seen that the main information (the three peaks in the figure for the case of pair-slit) is now compressed from $|k_x| \leq 3k_0$ into $|k_x| \leq k_0$. These waves can propagate to the far field in free space with features that are resolvable under conventional microscopes.

Based on the analysis discussed above, the route to design a superlens for far-field subwavelength imaging is summarized by a schematic in Fig. 3.4: first the information carried by high spacial frequencies are coupled and transferred by a near-field superlens; Considering the decay during wave propagation in free space, the intensity in spatial frequency domain will be amplified in the meanwhile. Then the near-field waves are compressed through phase compression so that the image can be propagated to the far field. To implement the two principle in a realistic lens structure, we use a double layer meander structure for coupling and transferring the near-field waves, and a planar plasmonic lens for phase compensation. Due to the fact that the far-field super-resolution imaging is realized separately with two plasmonic elements, the design is named cascaded plasmonic superlens.

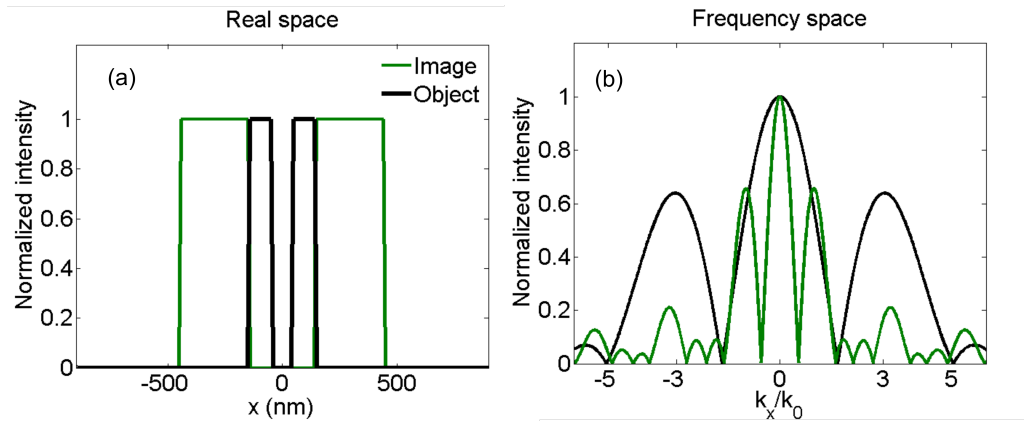


Figure 3.3 (a) Real space field distribution of a pair-slit object with a slit width of 100 nm and distance of 200 nm and its image magnified by a factor of 3 distribution; (b) Angular spectrum of the object and its image.

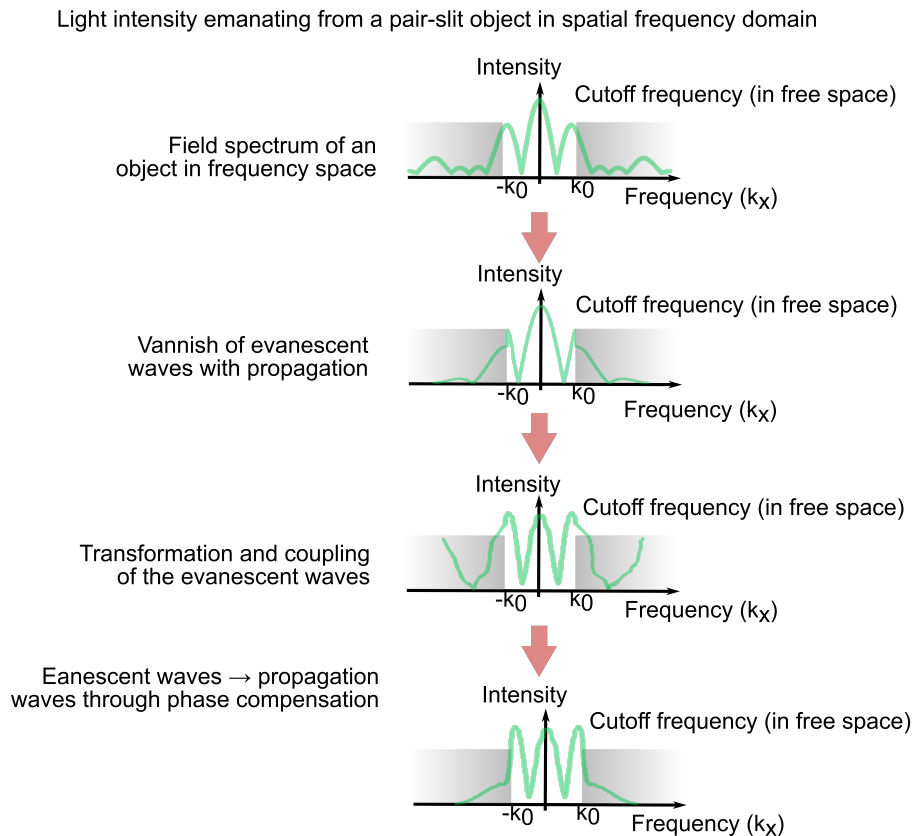


Figure 3.4 Schematic for principle of direct imaging with super resolution in the far field which is going to be realized by a cascaded plasmonic superlens.

3.1.3 Simulation method: rigorous coupled wave analysis

An in-house developed software package Microsim based on rigorous coupled wave analysis (RCWA) method is used to calculate the optical properties of the suggested superlens. RCWA is a Fourier-space method, by which fields are represented as a sum of field spatial harmonics, and is a most widely used method for analyzing diffraction of electromagnetic waves by period structures with a relatively straightforward technique to obtain accurate solutions of Maxwell's equations:

$$\nabla \times \mathbf{E} = -\frac{\partial \mathbf{B}}{\partial t}, \quad (3.6)$$

$$\nabla \times \mathbf{H} = \frac{\partial \mathbf{D}}{\partial t} + J, \quad (3.7)$$

$$\nabla \cdot \mathbf{D} = \rho, \quad (3.8)$$

$$\nabla \cdot \mathbf{B} = 0, \quad (3.9)$$

where \mathbf{E} is the electric vector field, \mathbf{B} is the magnetic induction, \mathbf{H} is the magnetic vector field and \mathbf{D} is the displacement current. The current density J and the charge density ρ are zero for our case since no charge or current source is present.

The method has been extensively described in literatures [109–113]. In this section, we only present the essential matrices for a brief introduction to the method. A schematic in Fig. 3.5 shows a periodical grating bounded by two different media with refractive indices n_I and n_{II} . The periodicity of the grating is P_x and the grating height is h .

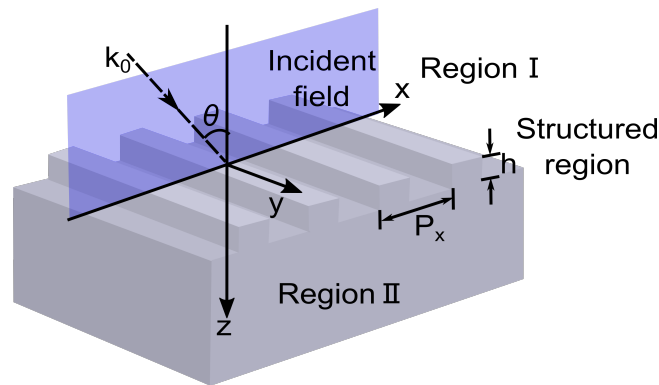


Figure 3.5 Schematic of a periodic structure and illumination configuration for RCWA.

To simplify the problem, we assume a plane wave illumination at a wavelength of λ with the incident plane perpendicular to the grating and consider only the transverse magnetic (TM) polarization. The incident magnetic field with a time harmonic of $\exp(i\omega t)$ and a unit amplitude propagating in the z -direction, can be expanded by a series of space harmonics

$$H_{inc,y} = \exp[-jk_0 n_I (\sin \theta \cdot x + \cos \theta \cdot z)]. \quad (3.10)$$

The magnetic field $H_{I,y}$ in the reflected ($z < 0$) and transmitted $H_{II,y}$ ($z > h$) region can be written as:

$$H_{I,y} = H_{inc,y} + \sum_i R_i \exp[-j(k_{xi}x - k_{I,zi}z)], \quad (3.11)$$

$$H_{II,y} = \sum_i T_i \exp\{-j[k_{xi}x + k_{II,zi}(z - h)]\}, \quad (3.12)$$

where k_{xi} is determined by the Floquet condition and $k_{I,II,zi}$ is decided by k_{xi} and $n_{I,II}$ [111]. R_i is the normalized magnetic field amplitude of the i th order reflected wave in region I. T_i is that of the i th order transmitted wave in region II.

In the grating region ($0 < z < h$), the field distribution can be written as Fourier expansion

$$H_{gy} = \sum_i U_{yi}(z) \exp(-jk_{xi}x), \quad (3.13)$$

$$E_{gx} = j\left(\frac{\mu_0}{\varepsilon_0}\right)^{1/2} \sum_i S_{xi}(z) \exp(-jk_{xi}x), \quad (3.14)$$

where U_{yi} and S_{xi} are the normalized magnetic and electric field of the i th space harmonic fields. Rewrite the Maxwell equations for the field components shown above:

$$\frac{\partial H_{gy}}{\partial z} = -j\omega\varepsilon_0\varepsilon E_{gx}, \quad (3.15)$$

$$\frac{\partial E_{gx}}{\partial z} = -j\omega\mu_0 H_{gy} + \frac{\partial E_{gz}}{\partial x}. \quad (3.16)$$

Substituting Eqs. 3.13 and 3.14 to Eqs. 3.15 and 3.16 and eliminating E_{gz} , we obtain the coupled-wave equations in the reduced form of:

$$\left[\frac{\partial^2 \mathbf{U}_y}{\partial (z')^2} \right] = [\mathbf{E}_g \mathbf{B}] [\mathbf{U}_y], \quad (3.17)$$

where

$$z' = k_0 z, \quad (3.18)$$

$$\mathbf{B} = \mathbf{K}_x \mathbf{E}_g^{-1} \mathbf{K}_x - \mathbf{I}. \quad (3.19)$$

\mathbf{E}_g is a matrix formed by the permittivity components. \mathbf{K}_x is a diagonal matrix, with the i th element equal to k_{xi}/k_0 . \mathbf{I} is the identity matrix. The above equations can be solved by calculating the eigenvalues and the eigenvectors associated with the matrix $\mathbf{E}_g \mathbf{B}$ having a dimension of $(n \times n)$, where n is the number of space harmonics retained in the field expansion.

According to [111], the set of coupled-wave equations can be solved by calculating the eigenvalues and the eigenvectors associated with the matrix \mathbf{B} by matching the tangential electric- and magnetic-field components at the two boundaries. At the input boundary ($z = 0$):

$$\begin{bmatrix} \delta_{i0} \\ j \frac{\cos \theta}{n_I} \delta_{i0} \end{bmatrix} + \begin{bmatrix} \mathbf{I} \\ -\mathbf{Z}_I \end{bmatrix} [\mathbf{R}] = \begin{bmatrix} \mathbf{W} & \mathbf{W}\mathbf{X} \\ \mathbf{V} & -\mathbf{V}\mathbf{X} \end{bmatrix} \begin{bmatrix} c^+ \\ c^- \end{bmatrix}, \quad (3.20)$$

where $\delta_{i0} = 1$ for $i = 0$ (Region I) and $\delta_{i0} = 0$ for $i \neq 0$ (others). c^+ and c^- are unknown values to be decided by boundary conditions and at output boundary ($z = h$):

$$\begin{bmatrix} \mathbf{W}\mathbf{X} & \mathbf{W} \\ \mathbf{V}\mathbf{X} & -\mathbf{V} \end{bmatrix} \begin{bmatrix} c^+ \\ c^- \end{bmatrix} = \begin{bmatrix} \mathbf{I} \\ j\mathbf{Z}_{II} \end{bmatrix} [\mathbf{T}], \quad (3.21)$$

where \mathbf{W} is the eigenvector matrix. $\mathbf{V} = \mathbf{W}\mathbf{Q}$, in which \mathbf{Q} is the positive square root of the eigenvalues of the matrix \mathbf{B} . \mathbf{X} is a diagonal matrix related to the structure region. \mathbf{Z}_I and \mathbf{Z}_{II} are diagonal matrices with the diagonal elements $(k_{I,zi}/k_0)$ and $(k_{II,zi}/k_0)$ [111]. If there is more than one layer of structures as shown in Fig. 3.6, there is a relation [114]:

$$\begin{bmatrix} \delta_{i0} \\ j \frac{\cos \theta}{n_I} \delta_{i0} \end{bmatrix} + \begin{bmatrix} \mathbf{I} \\ -\mathbf{Z}_I \end{bmatrix} [\mathbf{R}] = \prod_{i=1}^K \left(\begin{bmatrix} \mathbf{W}_i & \mathbf{W}_i \mathbf{X}_i \\ \mathbf{V}_i & -\mathbf{V}_i \mathbf{X}_i \end{bmatrix} \begin{bmatrix} \mathbf{W}_i \mathbf{X}_i & \mathbf{W}_i \\ \mathbf{V}_i \mathbf{X}_i & -\mathbf{V}_i \end{bmatrix}^{-1} \right) \begin{bmatrix} \mathbf{I} \\ j\mathbf{Z}_{II} \end{bmatrix} [\mathbf{T}]. \quad (3.22)$$

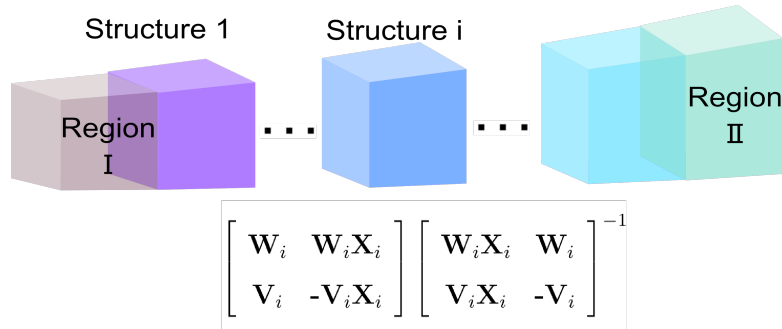


Figure 3.6 Structure with multiple layers.

Therefore, the transmitted or reflected field can be calculated with the coefficients of the space harmonics of the structured regions.

During the simulation, besides the shape and parameters of the structure, we need to determine mode number (the number of space harmonics n for expanding the field in Eq. 3.19). Theoretically, the larger the mode number, the more accurate the simulation result is. Due to the large number of arrays and columns used in defining the simulation model, the required calculation mode number is large as well. Considering the simulation time and memory, the convergence of the cascaded superlens is tested first as the results shown in Fig. 3.7.

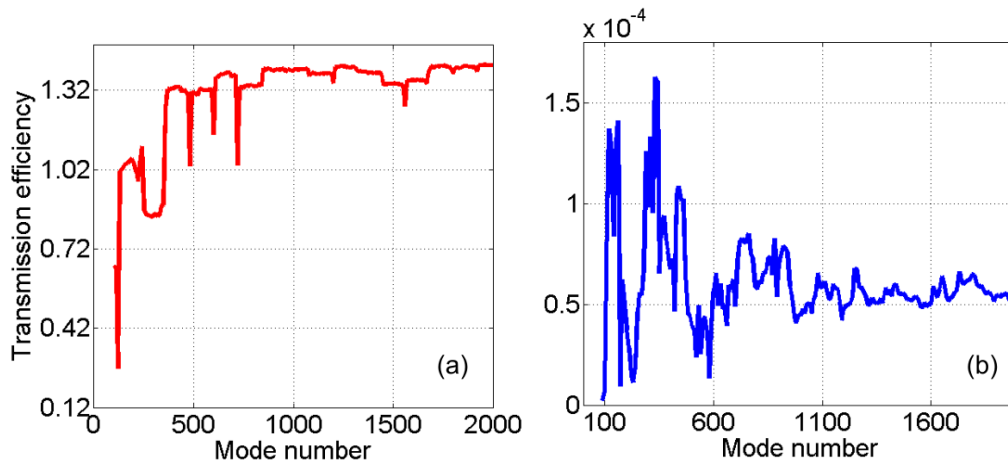


Figure 3.7 Influence of mode number n on near-field transmission efficiency when the size of the structure in the model is $24 \mu\text{m}$: (a) Simulation for a double-layer meander structure; (b) Simulation for the cascaded superlens.

The curve for a double-layer meander structure becomes smoother and the transmission efficiency converges as shown in Fig. 3.7(a), when the mode number is larger than 370 (except for several special points). A similar conclusion can be obtained for the test of the cascaded superlens when the mode number is larger than 600. Therefore, for the simulation of the cascaded superlens, the mode number of 400 for the double layer meander structure and 600 for the simulation of cascaded superlens are used.

We first calculated near-field transmission of each component in the superlens. However, direct excitation of evanescent waves in Microsim is not readily available. In this case, Otto configuration [30] is implemented to generate evanescent waves. As shown in Fig. 3.8, when $n_2 > n_1$ and when the incident angle θ is larger than the critical angle, total reflection occurs and evanescent field is generated. With this method, the accessible range of the transverse wave vector k_x is extended from $(-k_0, k_0)$ to $(-\frac{n_2}{n_1}k_0, +\frac{n_2}{n_1}k_0)$.

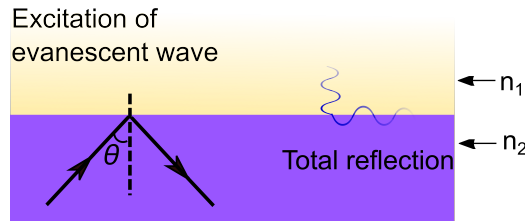


Figure 3.8 Otto configuration for generating evanescent waves. When the incident angle θ is larger than the critical angle for total reflection, evanescent waves are generated.

3.1.4 Advantages of the design

In the design of the cascaded superlens for far-field imaging with superresolution as described in subsection 3.1.1, the superlens is supposed to achieve following advantages:

- Direct imaging with an improved superresolution. The best reported resolution (demonstrated with experimental results using a pair of slits as an object) from side to side (right side of the left slit to left side of right slit) is about 1/5 of the incident wavelength [102]. The resolving of our suggested cascaded superlens, which will be calculated and fabricated in this dissertation, is increased to 1/8 of the incident wavelength.
- Operation at visible wavelength. The working wavelengths of hyperlenses, which are the most promising far-field plasmonic superlens, are dominantly in violet wavelength range [9]. The working wavelength for the cascaded superlens can be tuned to mid visible range. In this dissertation, the experimental verification will be conducted at the wavelength of 640 nm. Our suggested cascaded superlens will be a great contribution to the existed plasmonic superlenses.
- Higher transmission efficiency as a plasmonic lens. One disadvantage of the plasmonic lenses is high optical loss. For instance, for a hyperlens composed of 16 layer of silver/magnesium fluoride [103], the calculated transmission is lower than one percent. However, there are only three layers of metals in our designed cascaded superlens (two layers for a meander structure and one for a planar plasmonic lens).

- Relative large field of view (in contrast to hyperlens) with a planar object plane. Meander structure is a periodical structure and can be extended infinitely. Planar plasmonic lens modulates the phase distribution via a slit array with different slit sizes milled into a metallic slab. The aperture size of the lens can be extended with properly designed slit width and hence phase distribution.
- The concept to realize coupling evanescent waves and transferring them to propagating waves separately, provides flexibility to replace each component inside the cascaded superlens by other elements when a better choice is available, e.g. dielectric lens instead of planar plasmonic lens for phase compensation.

3.2 Dispersion engineering with metallic meander stacks

As discussed in Chapter 2, the working frequencies of the up to now reported superlenses, which are based on metal slabs or hyperbolic metamaterials, are in the violet or ultraviolet range. In order to shift the working frequency to middle visible range, a metallic meander structure will be employed as introduced in this section. With a proper structural design, the dispersion transmission in terms of k_x can be tuned through a large frequency range. We will discuss surface plasmon polaritons first, then simulate the transmission dispersion of meander cavity structures.

3.2.1 Surface plasmon polaritons

Surface plasmon polaritons (SPPs) are collective oscillations of free electrons in metals in response to light illumination, and propagate along the interface between the metal and the environmental dielectric medium. To derive the surface plasmon mode, we assume a plane wave with a wavelength λ in a medium with a refractive index of n_d (and permittivity of ε_d with $\varepsilon_d = n_d^2$) incident on a metal with a index of n_m (and permittivity of ε_m). Using a proper boundary conditions, we have:

$$k_{d,z}/\varepsilon_d = k_{m,z}/\varepsilon_m, \quad (3.23)$$

in which $k_{d,z}$ and $k_{m,z}$ are the normal wavevectors in dielectric and metal, respectively, as shown in Fig. 3.9.

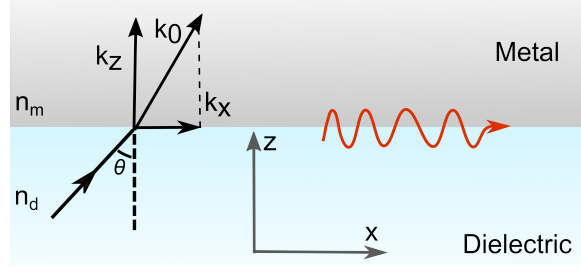


Figure 3.9 Excitation of SPPs at a dielectric/metal interface.

From the relation of $n^2 k_0^2 = k_x^2 + k_z^2$ (in case of p-polarization), we obtain the relation for the existence of surface waves in each medium [115]

$$k_{d,z} = -i(k_x^2 - \varepsilon_d k_0^2)^{1/2}, \text{ when } k_x^2 > \varepsilon_d k_0^2, \quad (3.24)$$

$$k_{m,z} = i(k_x^2 - \varepsilon_m k_0^2)^{1/2}, \text{ when } k_x^2 > \varepsilon_m k_0^2, \quad (3.25)$$

where $k_0 = \omega/c$. Note that surface waves, which decay exponentially into both media, only exist at the interface between a metal and a dielectric medium with opposite signs of the real part of their dielectric permittivities. Substitute Eqs. 3.24 and 3.25 into Eq. 3.23, we obtain the following dispersion relation at the air/metal interface [115]:

$$k_x = \omega/c \sqrt{\frac{\varepsilon_d \varepsilon_m}{\varepsilon_d + \varepsilon_m}}. \quad (3.26)$$

Since ε_m for metal is complex, we can rewrite ε_m and k_x to separate the real and imaginary parts as

$$\varepsilon_m = \varepsilon'_m + i\varepsilon''_m, \quad (3.27)$$

$$k_x = k'_x + ik''_x. \quad (3.28)$$

The real part of k_x determines the wavelength of the SPPs, and the imaginary part of k_x accounts for the damping of the SPPs when they propagate along the interface. Under the assumption of $|\varepsilon'_m| \ll |\varepsilon''_m|$, we can obtain the following expressions for the dispersion of SPPs:

$$k'_x = k_{sp} \approx \omega/c \left(\frac{\varepsilon'_m \varepsilon_d}{\varepsilon'_m + \varepsilon_d} \right)^{1/2}, \quad (3.29)$$

$$k_x'' \approx \omega/c \left(\frac{\epsilon_m' \epsilon_d}{\epsilon_m' + \epsilon_d} \right)^{3/2} \frac{\epsilon_m''}{2(\epsilon_d')^2}. \quad (3.30)$$

According to Eq. 3.29, the dispersion of the SPP at the air/metal interface is plotted in Fig. 3.10(b). The black line represents the dispersion of the light in air. The horizontal line shows the asymptotic resonance frequency ω_{sp} .

On a thin metal film, two SPPs are formed at the upper and lower surfaces. They are coupled and hybridized forming two new SPPs modes: long range SPP (LRSPP) and short range SPP (SRSPP). The splitting of the two branches increases with the decrease of the film thickness d [10].

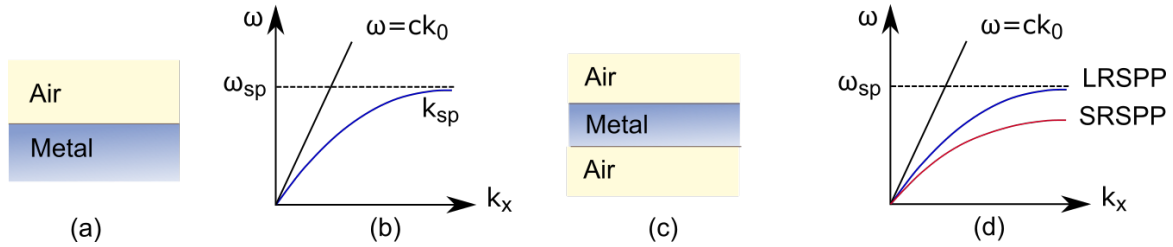


Figure 3.10 (a) Schematic of an air/metal interface; (b) SPP dispersion at the air/metal interface; (c) Schematic of a thin metal film in air; (d) Dispersions of the SPP modes formed on a thin metal film.

In both cases shown in Fig. 3.10(b) and (d), the dispersion relations lie below the light line. This means that surface plasmons have a larger wave vector than that of the light in free space, and SPPs cannot be excited by any light. To excite SPPs at a resonance condition of $k_x = k_{sp}$, we have to increase the wave vector of light or change the momentum of the SPPs, e.g., through grating diffraction.

3.2.2 Excitation of surface plasmon polaritons with meander structures

Nano-fabrication technologies nowadays allow materials to be structured and characterized on nanometer scale, which in turn enable the control of SPP excitations. In our design, a particular attention is given to a metallic meander structure, with which SPPs are excited via grating diffraction. The structure is out of a periodically corrugated metallic film. The wavevector of the surface wave k_{sp} is changed by adding a multiple of the reciprocal lattice vector of the grating according to

$$k_{sp} = k_x + mk_g, \quad (m = 0, \pm 1, \pm 2\dots), \quad (3.31)$$

in which $k_g = 2\pi/P_x$ is the grating vector, P_x is the periodicity of the corrugation. k_x is the transverse wave vector of the incident light determined by $k_x = k_0 \cdot \sin \theta = \omega/c \cdot \sin \theta$, and θ is the incidence angle of the light as shown in Fig. 3.9(a). The dispersion curves repeat themselves periodically in the k_x -space due to the diffraction by the periodic corrugation of the film, as can be seen in the Fig. 3.11(b). Parts of the dispersions are thus folded into the light line cone, and are therefore accessible by free space light.

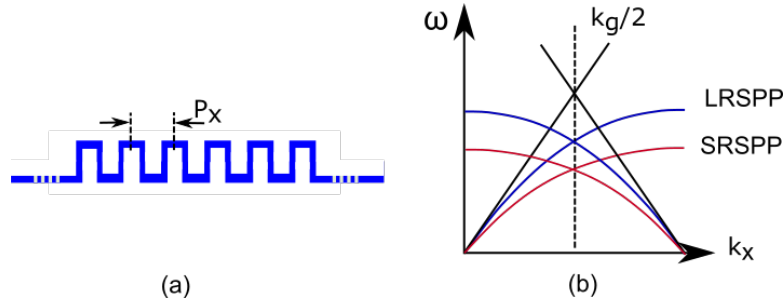


Figure 3.11 (a) A periodically corrugated metallic film with limited thickness; (b) Schematic of the SPP dispersions diffracted by the meander structure ($k_g = 2\pi/P_x$) shown in (a).

As we have seen from Fig. 3.11, periodically corrugated metallic meander structure support excitations of both LR- and SR-SPPs. Moreover, the excitation frequency of the SPPs can be shifted to visible frequencies, depending on the geometrical parameters of the corrugation. Calculated transmitted spectra of a single layer silver meander structure with different periodicities are plotted in Fig. 3.12. We see that a passband is induced due to the excitation of both SR- and LR-SPPs in the visible frequency range. The transmission spectrum is tuned in this range when the period is varied. Other than the period, other parameters such as W_r , t , d will change the optical properties as well. Details about the numerical calculations will be discussed in Section 3.2.3. This structure is a basic plasmonic element in our superlens, which is design for one dimensional subwavelength imaging.

Stacking two layer meander structures over each other, we obtain a double layer meander cavity (DLMC) structure. Mode interactions of surface plasmons between the top and bottom layer exist. The dispersion of the DLMC structure can be more flexibly varied via structural parameters, which makes the structure more practical in controlling the optical responses [116–119]. Although a larger bandwidth in terms of field transmission can be generated by stacking more meander layers, the transmission will be reduced dramatically. To avoid this problem, we will use only two layers of the meander structures. Furthermore, it is sufficient to use the two-layer structure to obtain an angular dispersion suitable for subwavelength imaging.

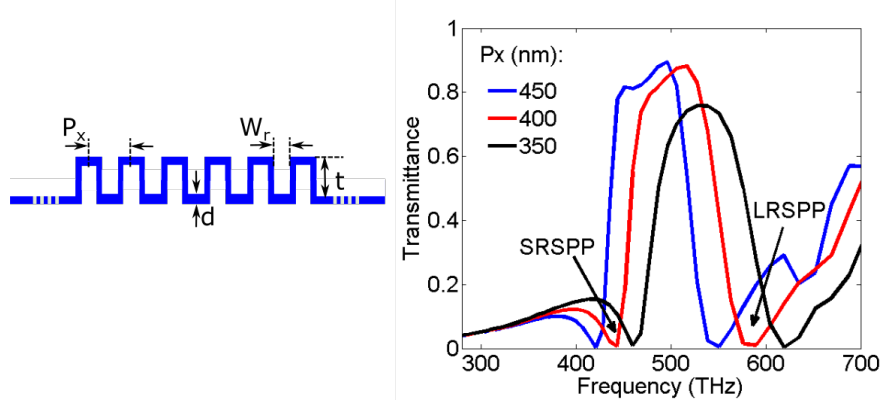


Figure 3.12 Calculated transmittance spectra of a single silver meander structure in air with a film thickness d of 30 nm, grating depth t of 30 nm and different periods ($W_r = P_x/2 - d$).

3.2.3 Near-field transmission dispersion of the DLMC structure

In this dissertation, the lens is designed and tested at the frequency of 468 THz (the wavelength of 640 nm). Therefore, the parameters used in this section are optimized values based on the results published in references [35, 116, 118].

A schematic for calculating the near-field transmission dispersion is illustrated in Fig. 3.13. Near-field transmission efficiency of a DLMC structure is calculated using the Otto-configuration as explained in Fig. 3.8, Subsection 3.1.3. In the simulation, the incident light is p-polarized plane wave and propagates from medium with $n_1 = 5$ to medium with $n_2 = 1$. By varying the incident angle from 0° to 89° , waves with a spatial frequency varying from 0 to $5k_0$ are excited behind medium n_1 .

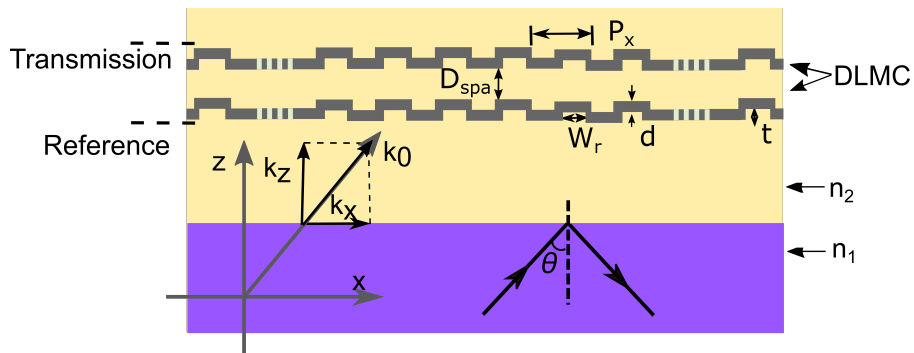


Figure 3.13 Schematic for calculation near-field transmission of a DLMC structure. D_{spa} is the distance between the two layers.

Figure 3.14 (a) shows the calculated near-field transmission spectrum as a function of k_x/k_0 behind a DLMC structure. In the calculation, the DLMC structure is placed 70 nm above the high index material n_1 . A reference spectrum is taken at the same position when no structure

is present. The near-field transmission efficiency of the structure is thus calculated as the ratio between the field intensity directly behind the DLMC structure and the reference intensity as shown in Fig. 3.13. Variation of the structural parameters, e.g. W_r , t , d , P_x or D_{spa} , change the dispersion. We can see that near-field transmission with a large intensity occurs in the range of 400 THz to 600 THz. In the figure, the white line is the reciprocal lattice vector k_g , which is normalized to k_0 ; the dashed lines are LR- or SR-SPP respectively. The transmission dispersion illustrates that a transfer of near-field waves occurs at much larger spatial frequencies than k_0 . The dispersion at the frequency of 468 THz is plotted in Fig. 3.14 (b). The peaks in the figure at $k_x/k_0 = 0.52$, 1.28 and 2.74 respectively are the results of SPPs at different orders. Although the spectrum in k_x is not continuous, when an additional element is added to it, the dispersion will be flattened as we will show in Section 4.1.

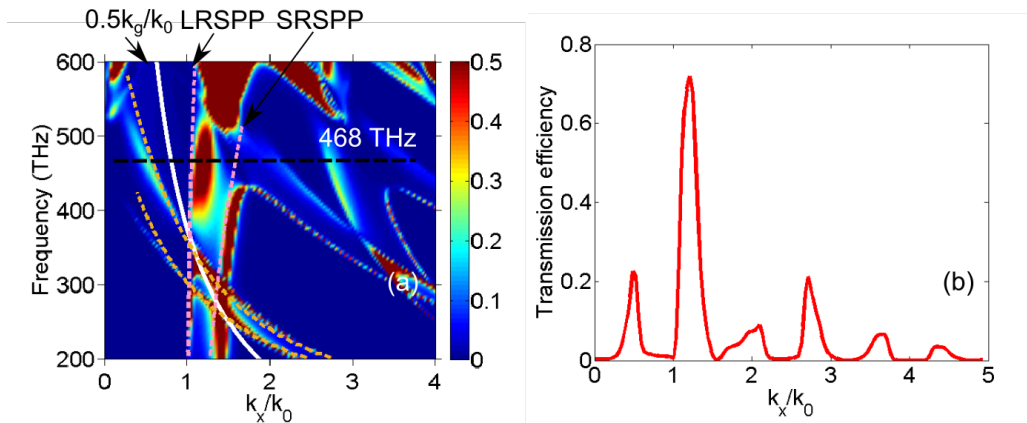


Figure 3.14 (a) Transmission dispersion spectrum of a DLMC structure with parameters: $P_x = 400$ nm, $d = 25$ nm, $D_{\text{spa}} = 70$ nm and $t = 50$ nm. White line: $\frac{k_g}{2k_0}$; (b) Amplitude of near-field transmission at the frequency of 468 THz.

Considering fabrication tolerance in deposition of thin metal films, the DLMC structure with a film thickness d of 20 nm was calculated as well. The transmission efficiency plotted in Fig. 3.15(a) is increased compared with the results with $d = 25$ nm (Fig. 3.14(b)) but with a similar bandwidth. This indicates that the structure is rather tolerant to the thickness of the metallic film.

Materials other than silver such as gold can also be used for the DLMC structure. As shown in Fig. 3.15(b), for a gold DLMC structure, a similar response in k_x is obtained. However, we find it is difficult to obtain a continuous and uniform thin gold film as we will show in Chapter 5. Therefore, the superlens structure will be fabricated with silver due to its superior optical properties, and we will perform the simulations mainly based on silver.

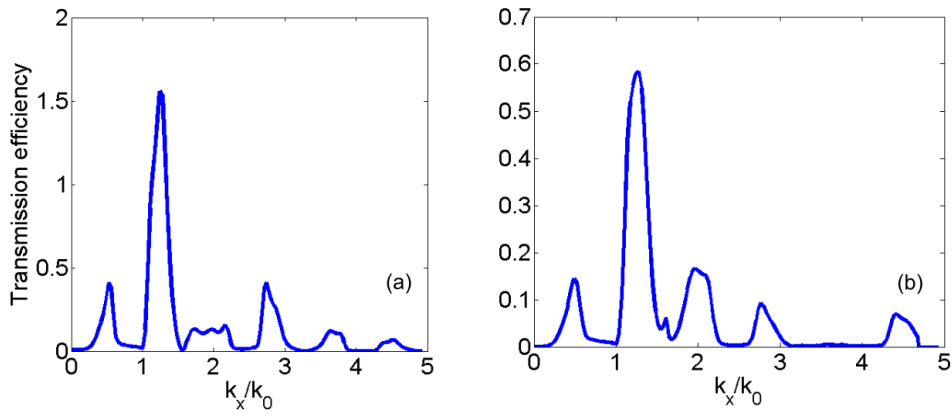


Figure 3.15 (a) Near-field transmission dispersion of a silver DLMLC structure with: $d = 20$ nm, $D_{\text{spa}} = 70$ nm and $t = 50$ nm at the frequency of 468 THz; (b) Dispersion of a gold DLMLC structure with $d = 30$, $t = 50$ and $D_{\text{spa}} = 70$ nm at the same frequency.

3.3 Phase compensation of the PPL structure

As we have discussed in Section 3.1, in order to obtain an image with magnification in the far field, a phase compensation mechanism is required. In our structure, a planar plasmonic lens (PPL) is chosen due to its compact size and flexibility for design [32]. In this section, we will discuss the working principle of the PPL structure and its imaging behaviors when it is used as a near-field lens.

3.3.1 Phase retardation through nano-slits

The design of the PPL is based on the principle that SPPs propagate through nanometer slits in a waveguide mode, and the wave propagating constant depends on the slit width [28, 31–34]. A schematic of a planar plasmonic lens is shown in Fig. 3.16.

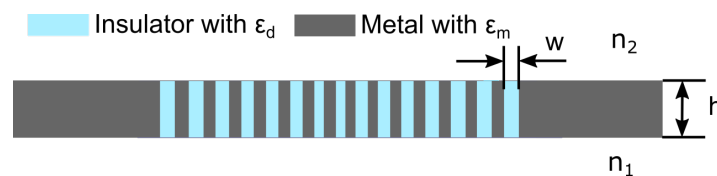


Figure 3.16 Schematic of a planar plasmonic lens based on a nanoscale slit array in a metallic slab.

Considering two parallel infinite metallic plates with a distance of w (slit width), the SPPs on each surface are coupled and propagate in the form of a waveguide mode for p-polarized light. The complex propagation constant β can be calculated according to [120]

$$\tanh\left(\frac{w}{2}\sqrt{\beta^2 - k_0^2\varepsilon_d}\right) = \frac{-\varepsilon_d\sqrt{\beta^2 - k_0^2\varepsilon_m}}{\varepsilon_m\sqrt{\beta^2 - k_0^2\varepsilon_d}}, \quad (3.32)$$

where ε_m and ε_d are the relative dielectric constants of the metal and the material in the slits. Eq. 3.32 is valid for the nano-slits with a limit slit height h as well. The phase of light transmitted through the nano-slits can be expressed as:

$$\phi = \phi_0 + \Delta\phi_1 + \Delta\phi_2 + \beta h - \theta, \quad (3.33)$$

where ϕ_0 is the initial phase at the entrance. $\Delta\phi_1$ and $\Delta\phi_2$ are the accompanied phase changes at the entrance and exit interface. θ is introduced by the multiple reflections between the entrance and exit surfaces. Only the term βh plays a dominating role in the equation [31] and therefore in our PPL design, we neglected other terms in the equation.

To obtain a lens with a focus length f , phase distribution at position x is obtained according to the equal optical length principle [31]:

$$\phi(x) = 2m\pi + \frac{2\pi f}{\lambda} - \frac{2\pi(f^2 + x^2)^{1/2}}{\lambda}, \quad (3.34)$$

where m is an integer. The calculated phase retardation of the nano-slits with Eqs. 3.32 and 3.33 in an silver slab with a thickness of 400 nm is plotted in Fig. 3.17(a). Assuming a focus length of 6.5 μm , a hyperbolic phase compensation of an ideal lens can be plotted according to Eq. 3.34 as shown by the red curve in Fig. 3.17(b). The pitch, the thickness and the slit width can be varied to alter the focus length. In our design, the pitch is 200 nm and height is 400 nm, the width of the nano-slits at the corresponding position can be calculated accordingly as the parameters shown in the figure caption are optimized results considering the fabrication feasibility with our facilities. In the design, the interactions among different slits were not taken into consideration, which will change the phase compensation and the actual focus length, which was also discussed in reference [31]. The phase compensation of the PPL structure calculated by Microsim is plotted in Fig. 3.17(b), the actual focus length is 2 μm , as will be shown later.

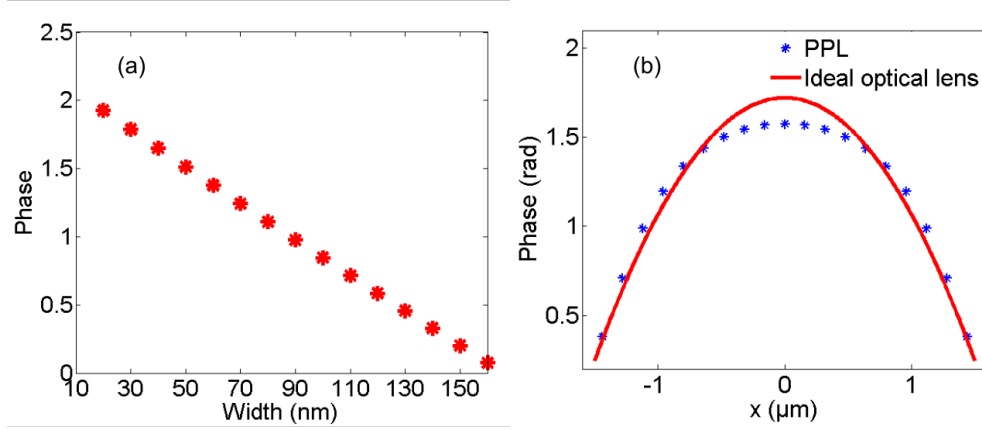


Figure 3.17 (a) Phase retardation in a metal-insulator-metal nano-slit composed of air and silver with a slit height of 400 nm but with different slit width; (b) Comparison of phase compensation of an ideal optical lens (focus length = $6.5 \mu\text{m}$) and the PPL structure calculated with Microsim with slit width of 88, 57.5, 47.5, 42, 34, 42, 47.5, 57.5, 64 and 88 nm, a pitch of 200 nm and height of 400 nm.

The focusing of a plane wave with different incident angle by the PPL structure with parameters same as in Fig. 3.17 is plotted in Fig. 3.18.

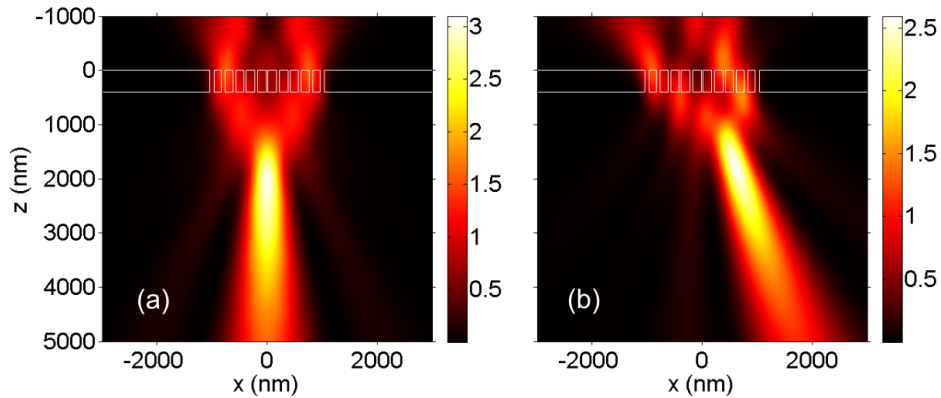


Figure 3.18 Focusing of a plane wave by our designed PPL structure with incident angle: (a) 0° ; (b) 15° .

3.3.2 Imaging by a planar plasmonic lens

To explore imaging properties of the designed PPL structure, a pair of slits with slit width of 100 nm are used as an object. The slit distance X_D is defined as the object size. The object is illuminated by a plane wave with an incident frequency of 468 THz and the object is buried in glass with a refractive index of 1.41 for an comparison with the simulation results of the cascaded superlens that we will show later.

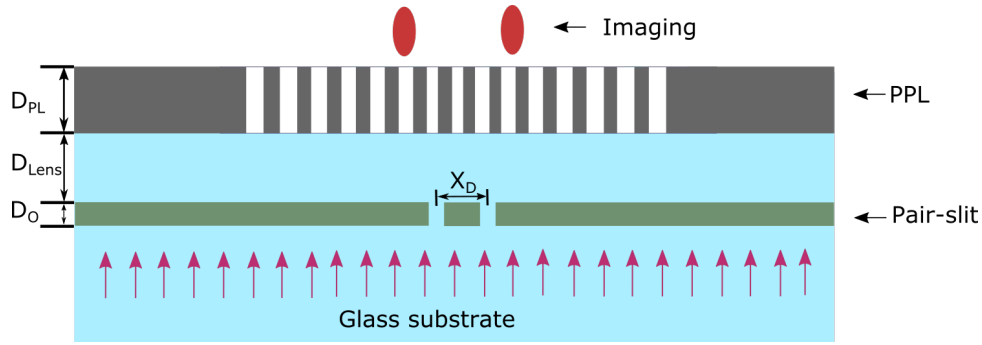


Figure 3.19 Schematic model in Microsim to calculate the image of an object via the PPL structure. The object is composed of a pair of slits in an optical opaque Cr slab.

The PPL used in the simulation has the same parameter as illustrated in Fig. 3.17. The distance between the PPL structure and the object is 640 nm. The far-field image with two intensity peaks is formed between $z = 200$ nm and $z = 700$ nm as shown in Fig. 3.20(a). The distance of the two peaks is identified as the image size.

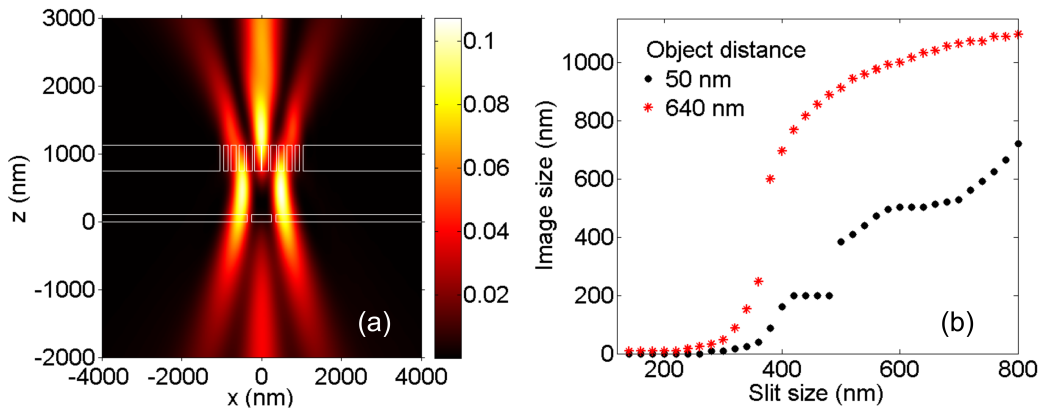


Figure 3.20 (a) Image of a pair-slit object with an object size of 600 nm and D_{Lens} of 640 nm; (b) Image size as a function of object size at $z = 538$ or 1000 nm with different object distance.

Take $z = 538$ nm as the image plane and plot the image size versus the object size as shown by the red curve in Fig. 3.20(b). The image is obviously magnified, though the relation is extremely nonlinear which may be constrained by the limited aperture size of the PPL structure. When we reduce the object distance D_{Lens} to 50 nm, which is close enough for the lens to collect evanescent waves, the calculated image size versus the object size is shown by the black curve in Fig. 3.20(b), the image plane of which is $z = 1000$ nm. The image size does not change with that of object at the X_D from 400 to 600 nm, which indicates a near-field interaction between the nano-slits in the PPL structure and the object. Both effects limit the practical application of the planar plasmonic lens as a near-field lens for subwavelength imaging.

4 Simulation of the functions of the cascaded superlens

In this chapter, we assemble the DLMC structure and the PPL structure together to form the far-field superlens. Its imaging property will be investigated for a pair-slit object using numerical simulations. The parameters of the structure will be optimized for experimental fabrication and verification that is going to be shown later.

4.1 Near-field transfer function of the cascaded superlens

As we have shown in Chapter 3, the near-field transfer function (TF) plays a key role for near-field subwavelength imaging. In this section, the near-field wave dispersion of the cascaded superlens in terms of the near-field transfer function, which is different from the ideal one as written in Eq. 3.4, will be studied.

4.1.1 Wave dispersion of the cascaded superlens

As we have discussed in Chapter 3, to achieve far-field subwavelength imaging, we intend to use two plasmonic elements. One is a DLMC structure used to couple and amplify the information carried by high spatial frequencies, and the other one is a PPL structure used to introduce a phase compensation for image magnification. When the DLMC structure is assembled with the PPL structure as shown by Fig. 4.1, the cascaded structure has both the characters of a wide range transfer function in spacial frequency and phase compensation to transfer evanescent waves to propagating ones.

Near-field transmissions as a function of k_x/k_0 were calculated using Microsim in the same way as shown in the Fig. 3.14 and the positions to collect the reference and transmissions are shown by the schematic in Fig. 4.2(a). Different from the calculations in Chapter 3, we bury or place the structures in or on the top of SOG considering the actual situation in fabrications.

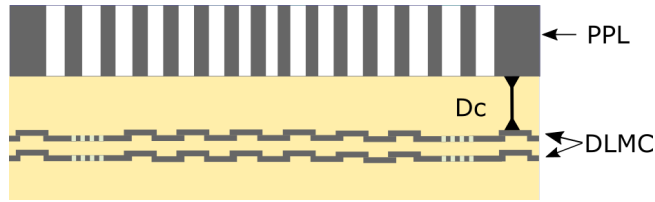


Figure 4.1 Schematic of the designed cascaded superlens for far-field subwavelength imaging.

Near-field transmission was obtained by normalizing the near field 70 nm behind the element to the incident field. Dispersions of the three structures at the wavelength of 640 nm are plotted in Fig. 4.2(b). A passband for both propagating and evanescent waves are shown for the PPL slab. However, a huge transmission peak is manifested around $k_x = 1.6k_0 = 0.5k_g$, which explains the nonlinear problem of the PPL structure for near-field imaging as discussed in Chapter 3. Similarly, there is also a strong transmission peak with the DLMC structure around $k_x = 1.8k_0$. In contrast, when the PPL is combined with the DLMC structure, a flattened and broadened dispersion is generated without reducing transmission, as shown by the red curve in Fig. 4.2(b). The angular spectrum of the cascaded structure is extended to $3k_0$ compared with $2k_0$ of the DLMC structure.

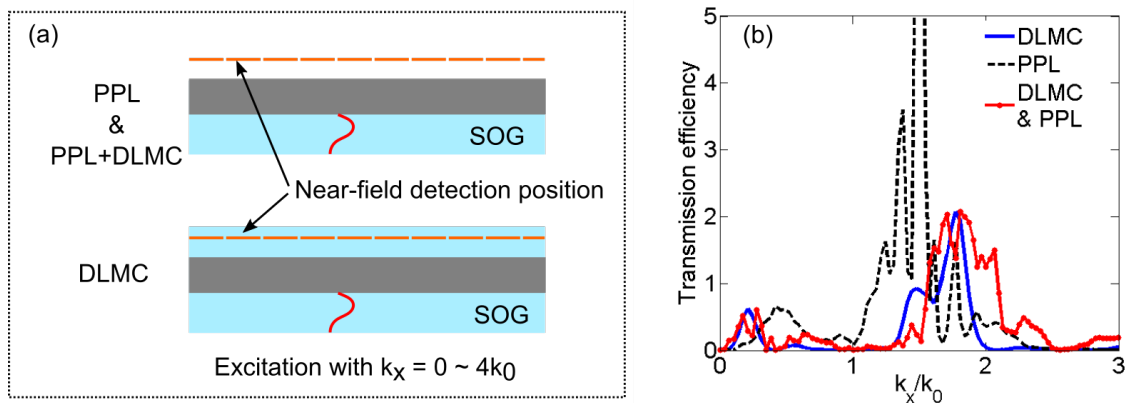


Figure 4.2 Near field transmission dispersion of the sub-components and the cascaded superlens. (a) Configuration for the dispersion calculation; (b) Near-field transmission dispersions of different elements as a function of k_x/k_0 at the wavelength of 640 nm.

To illustrate the effect of these dispersion curves for a superlens, we use the transmission efficiency of the angular spectrum as a near-field transfer function without considering the phase of the TF and calculate the output field distribution of the object analytically according to Eq. 3.5. The angular spectrum of the same object ($X_D = 200$ nm and $w = 100$ nm) in Fig. 3.2 is shown in Fig. 4.3(a). We can see that the output field transmitted through the DLMC structure has side-lobes as shown by the blue curve in Fig. 4.3(b). However, by introducing a PPL structure, the side lobes are reduced as shown by the red curve in Fig. 4.3(b).

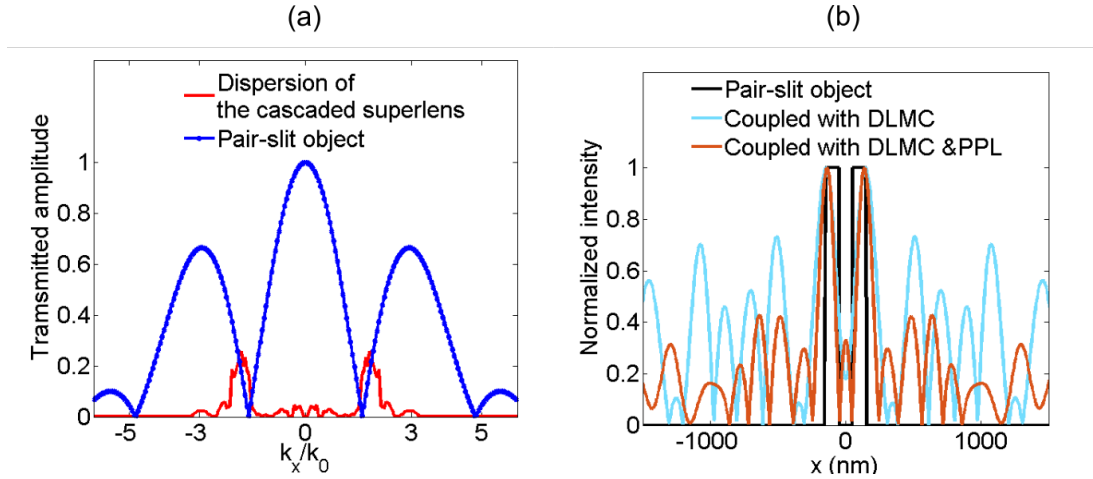


Figure 4.3 (a) Field distribution of a pair-slit ($w = 100$ nm and $X_D = 200$ nm) and transmission dispersion of the cascaded superlens at 640 nm in k -space; (c) Intensity distribution of the pair-slit object, that coupled with dispersion of DLMC and the cascaded superlens directly behind the structure.

The simulation results of the near-field transmission distribution illustrate that the cascaded structure has advantages compared with those using the DLMC or the PPL structure alone. In our calculation, the PPL and the DLMC structure are aligned symmetrically with each other. To study the position tolerance between the two elements, an addition simulation was calculated to see how the position shift will affect the near-field TF. The results are illustrated in Fig. 4.4. In the simulation, the position of the PPL structure (or relatively the position of the DLMC structure) is shifted to the right within a distance of 100 nm with steps of 20 nm. It can be seen that the position shift leads to a variation to the transmitted dispersion distribution. The pass band becomes broader, which is a positive change for subwavelength imaging. However, when the shift is larger than 60 nm, the transmitted waves turns to several peaks which are not desired. Nevertheless, a tolerance of 60 nm position shift between the PPL and the DLMC structure is quite enough for the fabrication.

Briefly, the DLMC structure can be used as a near-field superlens [46], resonant peaks in the near-field dispersion shown in Fig. 4.2 will introduce strong side-lobes to the imaging field. Moreover, the DLMC structure can only transfer the subwavelength information from the front side to the back side of the structure and the high frequency information vanishes rapidly in the far field. On the other side, focusing capability of the PPL structures has been demonstrated almost a decade ago [31, 32], however the structure alone cannot be applied for near-field imaging due to its strong interaction with the object as we have already discussed in Chapter 3. Nevertheless, when the DLMC structure is combined with the PPL structure, the TF function is flattened in intensity and broadened in k_x , and is more suitable for a near-field superlens. Moreover, a phase compensation for magnification will be introduced by the PPL structure

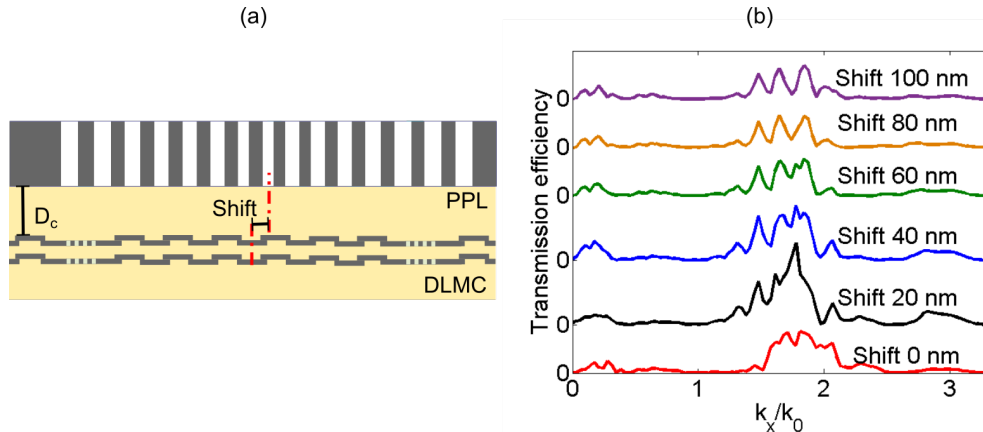


Figure 4.4 Dispersion of the cascaded superlens with a relative position shift between the two sub-components: (a) Schematic of the simulation model; (b) Near-field transmission at the wavelength of 640 nm.

and the details will be illustrated in following subsections. It should be emphasized that in our design, besides the flat design, the PPL structure behaves more like a high-index immersion lens than a conventional geometrical lens.

4.1.2 Phase compensation introduced by the PPL structure

In the former subsection, we have calculated the near-field transmission of the sub-components of the cascaded superlens. We also analytically explained the benefits by assembling the DLMLC structure together with a PPL structure. To illustrate the phase-compensation effect brought by the PPL structure, here we perform a simple calculation. We take the transmission dispersion of the cascaded structure as a near-field TF, and couple it with a pair-slit object ($w = 100$ nm and $X_D = 200$ nm). Together with Eq. 3.5, we can propagate the field according to [121]:

$$E(k_x; z) = E(k_x; 0) \cdot \exp(i \cdot z \cdot \sqrt{1 - k_x^2}), \quad (4.1)$$

where $E(k_x; 0)$ is the Fourier transformation of $E_2(x) \cdot \exp[i \cdot \phi(x)]$ and $\phi(x)$ is the hyperbolic phase compensation of our designed PPL structure as shown in Fig. 3.17. The result is plotted in Fig. 4.5(a) and we can see that a resolvable image of a pair-slit object with magnification is achieved at the position between $z = 1000$ and 1500 nm. The resolution is better than Abbe diffraction limit at the wavelength of 640 nm.

For the cascaded superlens, a focal spot can be numerically obtained thanks to the phase compensation introduced by the PPL structure. The focusing field intensity calculated with Microsim is shown in Fig. 4.5(b). The size of the focal spot in terms of the full width at half

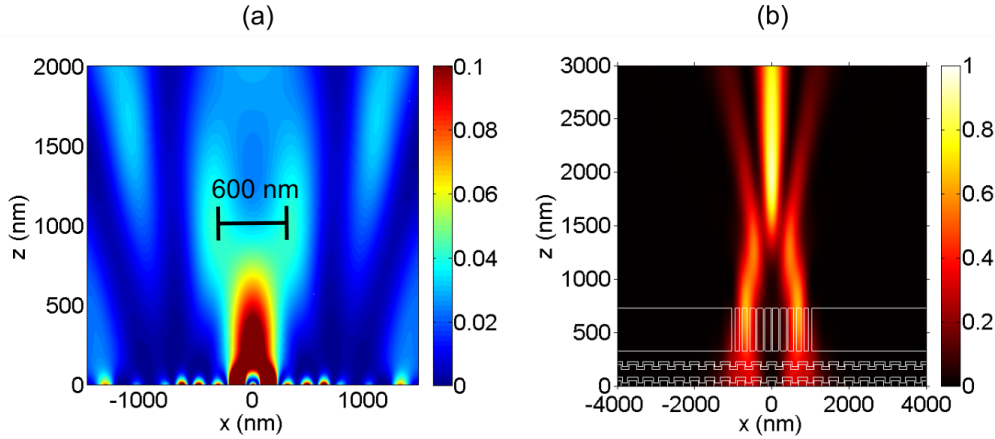


Figure 4.5 (a) Imaging with magnification using the transmitted field distribution of the cascaded superlens and phase compensation of the designed PPL structure as a transfer function for a virtual lens. Object: two slits with a width of 100 nm and slits distance of 200 nm; (b) Focusing pattern of a cascaded superlens ($D_c = 70$ nm) for a plane wave with normal incidence .

maximum (FWHM) is 419 nm, which is 4/5 of that when only the PPL structure is used. The focal spot is not subwavelength which is not necessary for our superlens, since we intend to observe sub-diffraction-limited objects in the far field. Furthermore, the focal length of the cascaded superlens is the same as the focal length of the designed PPL structure, which is $2 \mu\text{m}$.

4.2 Numerical calculations of the cascaded superlens using Microsim

According to the analytical analysis we have performed in Section 4.1, superresolution imaging in the far field can be obtained with the cascaded superlens. To examine the imaging behavior of the cascaded superlens using numerical experiment, simulations will be done using Microsim. Parameters of the structure will also be optimized for fabrication.

4.2.1 Lateral resolution of the cascaded superlens

A pair of slits are used as an object in the simulation. The slits in a chromium layer are located underneath the cascaded superlens as illustrated in Fig. 4.6. The slit distance X_D from slit center to center is designated as the size of the object. According to our design, when a p-polarized plane wave illuminates the object from the bottom side, an image with magnification

size due to the film corrugation and near-field interactions. Nevertheless, this slight intensity variation does not influence the imaging behavior of the superlens.

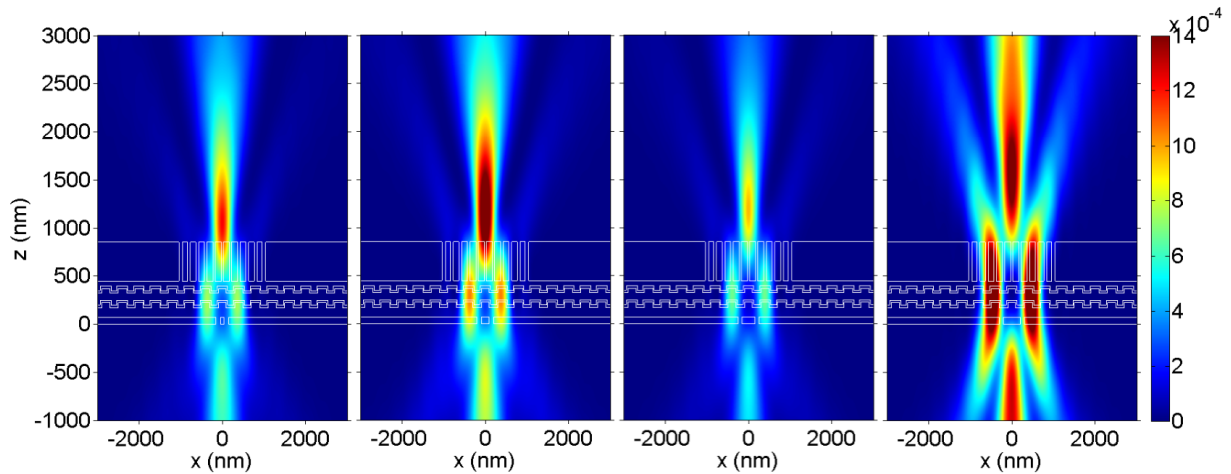


Figure 4.7 Field distributions imaged by the cascaded superlens for pair-slit objects with $w = 100$ nm and $X_D = 200, 300, 400$ and 500 nm separately. Simulation parameter (nm): $D_{PL} = 400$, $D_C = 50$, $D_{DM} = 210$, $D_{OM} = 70$, $D_O = 100$, $D_{spa} = 70$, $P_x = 400$, $W_r = 200$, $d = 30$ and $t = 50$.

If we take $z = 470$ nm as the image plane and plot the one-dimensional field intensities as shown in Fig. 4.8(a), a lateral resolution of 180 nm for the optimized cascaded superlens can be derived according to Rayleigh criterion (image contrast smaller than 0.73). Under the same criterion, the calculated resolution for the pair-slit with the absence of the superlens is 360 nm. The results show that the resolving power with the proposed superlens is doubled (180 nm vs. 360 nm). This value is different from the predication of Abbe diffraction limit (320 nm at $\lambda = 640$ nm). In our case, the definition of the object size is different from that of a point light source. It is because the slit width is 100 nm and the gap between the slits is 100 nm. Details will be discussed later in Chapter 6. The image size as a function of the object size is plotted in Fig. 4.8(b). A nearly linear relationship between the two parameters is obtained. The problem of non-linearity of the PPL structure shown in Section 3.3.2 is improved greatly with the cascaded superlens. For the cascaded superlens, the magnification factor is not constant, which is a limitation of the design. The problem will be diminished by a modified cascaded superlens illustrated in Chapter 7.

4.2.2 Influence of the position shift between the sub-components

In the verification experiment, the sub-components of the cascaded superlens are going to be fabricated on the top of the object one after the other. In this subsection, we study how the

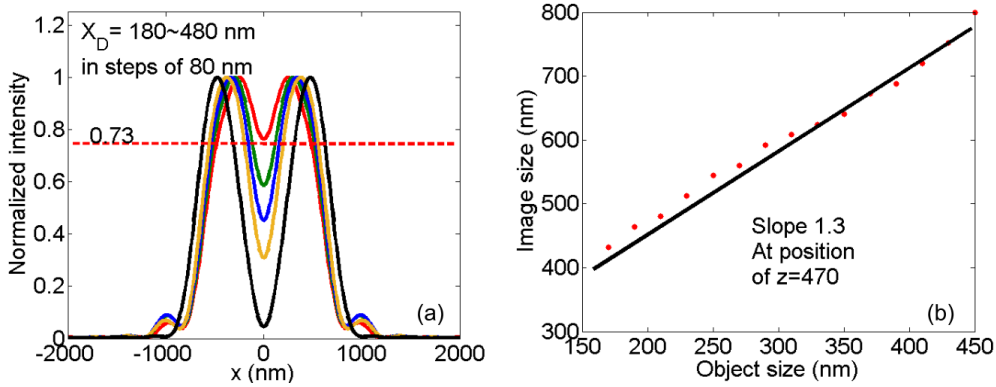


Figure 4.8 (a) Image field intensities along the x-axis for a pair-slit object with different sizes at $z = 470$ nm; (b) Image size as a function of object size at the same position.

relative position between the elements influence the imaging, the position of each sub-structure is shifted separately with respect to the central axis at $x = 0$ and calculate the image field.

First, the whole structure of the cascaded superlens is shifted with a step of 20 nm with respect to the object (at $x = 0$). The image field distribution is plotted in Fig. 4.9(a). It can be seen that the image position and shape remain nearly unchanged in the xz -plane. To obtain a clear view of the image deformation introduced by the position shift of the cascaded superlens, the image intensity profiles of the pair-slit at $z = 470$ nm with different position shifts are further plotted in Fig. 4.9(b), in which we can see that the position shift of the cascaded superlens (or relatively the position shift of the object) leads to a small side-lobe to the image intensity distribution, which is neglectable.

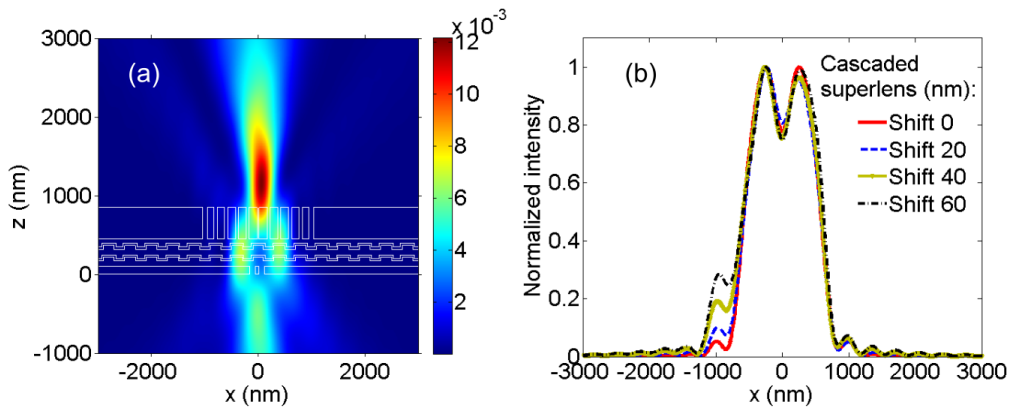


Figure 4.9 Field distributions imaged by the cascaded superlens for pair-slit objects ($w = 100$ nm and $X_D = 200$ nm) with different position shift of the cascaded structure: (a) Far-field image with a 20 nm of the cascaded superlens shift to the right; (b) Normalized intensity distribution at about $z = 470$ nm.

Figure 4.10 is the simulation results studying the position shift of the PPL structure with respect to $x = 0$. It can be seen that the image plane is shifted to $z = -500$ nm as shown in

Fig. 4.10(a). The image intensity at $z = -500$ nm are plotted in Fig. 4.10(b). The intensity of one of the two peaks is affected by the position shift of the PPL structure, yet an image with fixed size can still be obtained though with intensity decrease and the width of one slit in the image broadens when the shift is larger than 40 nm.

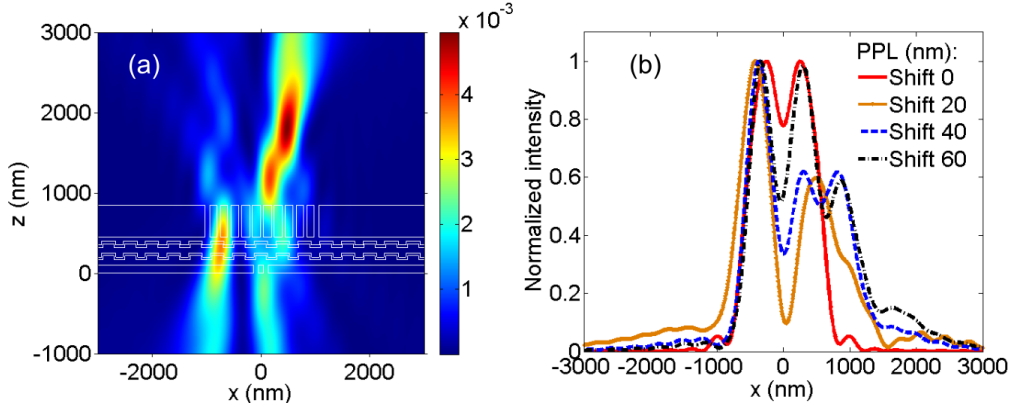


Figure 4.10 Field distributions imaged by the cascaded superlens for pair-slit objects ($w = 100$ nm and $X_D = 200$ nm) with different PPL position shift: (a) Far-field image with a 20 nm shift of the PPL structure to the right; (b) Normalized intensity distribution at about $z = 0$ nm.

However, if we shift the DLMC structure as shown in Fig. 4.11(a), the variations of the images are similar to the results when we shift the PPL structure. Furthermore, when the position shift of the DLMC structure is larger than 60 nm (shown in Fig. 4.11(b)), it is hard to identify the object pattern from image field due to the intensity difference between the pair of slits and increase of a side-lobe in the image. This is led by the corrugation in the meander structure which works like a wave guide and largely affects the field distribution of the pair-slit when the size of it is comparable with the period of the DLMC structure.

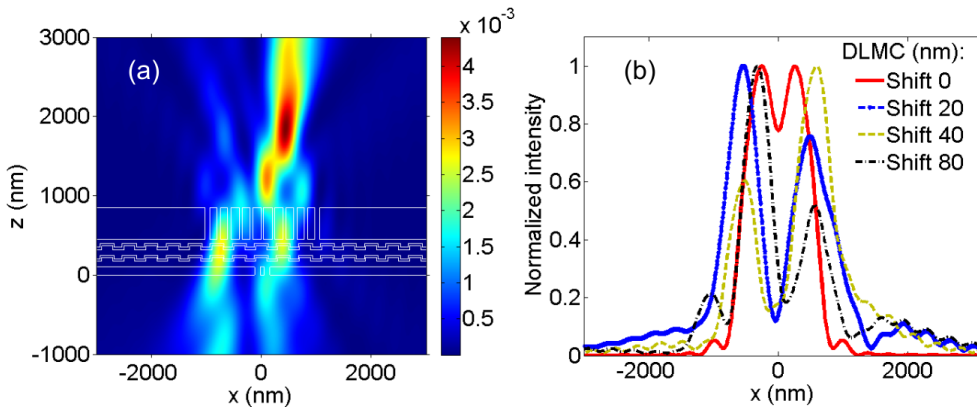


Figure 4.11 Field distributions for pair-slit objects ($w = 100$ nm and $X_D = 200$ nm) imaged by the cascaded superlens with different DLMC position shift: (a) Far-field image with a 20 nm shift of the DLMC structure to the right; (b) Normalized intensity distribution at about $z = 0$ nm .

The problem of the image size and position varies with the relative position between the DLMC structure and the object is a limitation of the cascaded superlens, which will be modified and the optimization results will be illustrated later.

To summarize, numerical calculations show that a lateral resolution of 180 nm can be obtained with an optimized cascaded superlens at the incident wavelength of 640 nm. The fabrication tolerance of the element shift is 20 nm which is achievable in fabrication. The simulation results are going to be verified by experiments and shown in Chapter 6.

4.2.3 Discussion of parameter tolerance for the cascaded superlens

In the former section, the steps among the parameter tests are relatively large in the range that can be realized with our fabrication methods. In this section, further simulation results with smaller steps, with which imaging in the far field can still be obtained, will be presented.

Take the film thickness inside the DLMC structure as an example. If we reduce the film thickness d from 30 nm to 25 nm but keep other parameters the same as the ones used in Section 4.2.2, image distribution is similar except for an image position shift of about 200 nm to the positive z -axis direction. Results are shown in Fig. 4.12.

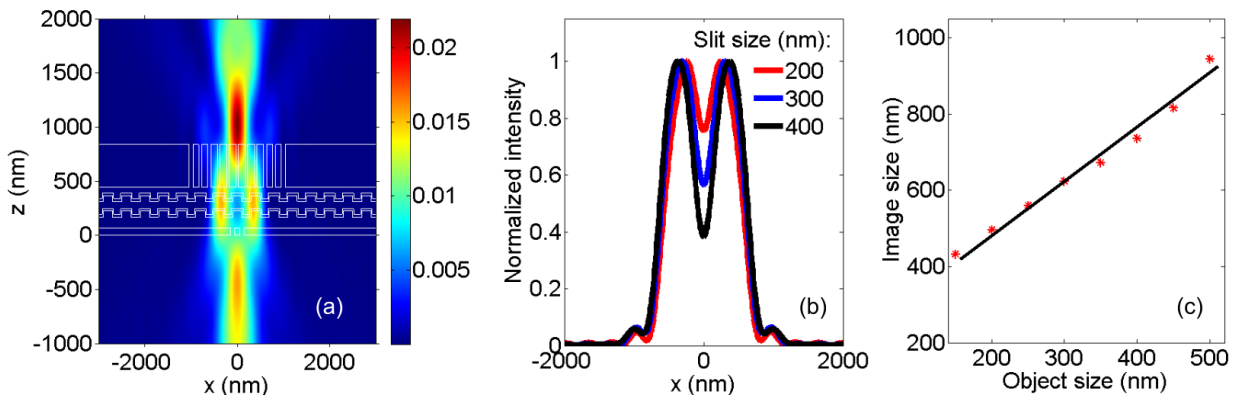


Figure 4.12 Field distributions imaged by the cascaded superlens for pair-slit objects with $d = 25$ nm and other parameters are the same as that shown in figure 4.7: (a) Image distribution in the xz -plane when $w = 200$ nm; (b) Normalized intensity distribution at $z = 250$ nm with different slit distances; (c) Image size as a function of slit size.

If we alter other parameters of the cascaded superlens, a similar field distribution can be obtained as the results shown in Fig. 4.8 or 4.12. Take the intensity distribution of the pair-slit with distance of 200 nm as an example, image distributions at image planes with other parameters are plotted in Fig. 4.13. If not specifically mentioned in the figures, parameters remain the same as those in previous section. The simulation results show that if the parameters

varies about 10 % around the optimized ones, the variation of the image distribution is nearly unchanged considering the size of the image and the field intensity distribution in the xz -plane. The results of which the relation between the slit distance and image size are not linear are not illustrated in the dissertation.

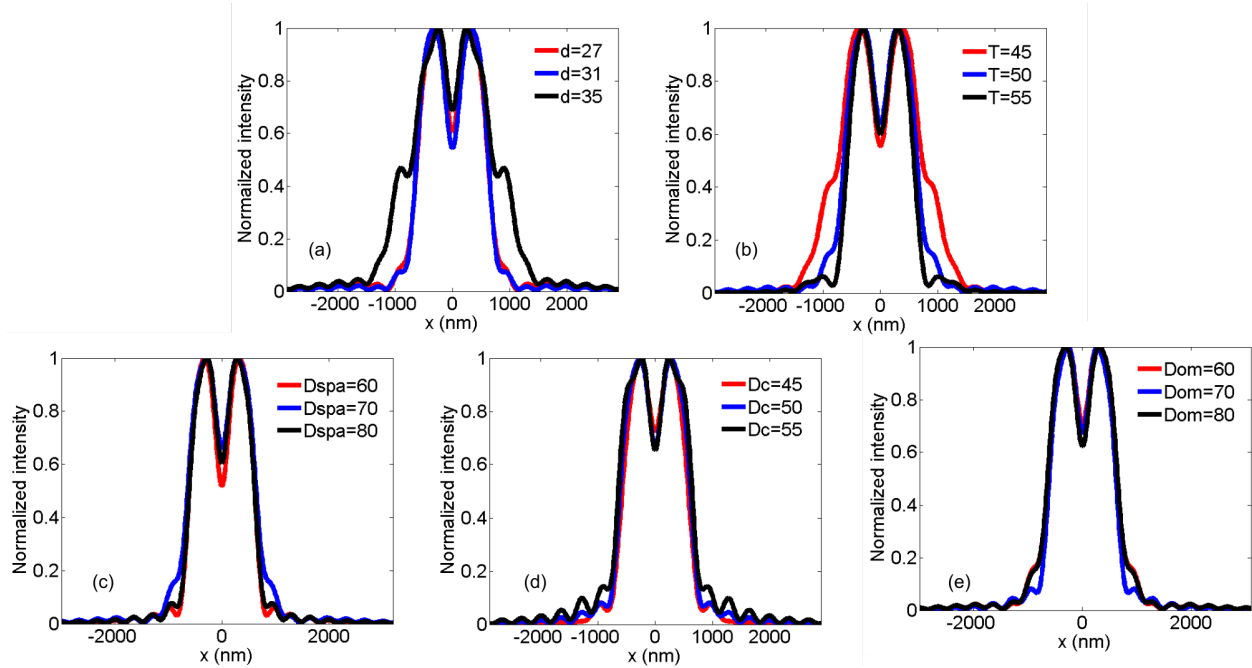


Figure 4.13 Normalized intensity distributions imaged by the cascaded superlens for pair-slit objects ($w = 100$ nm and $X_D = 180$ nm) with varied parameters (nm): (a) Thickness of film in DLMC; (b) Depth of the meander; (c) Distance between two meanders; (d) Distance between the DLMC structure and the PPL structure; (e) Distance between the pair-slit and the cascaded superlens.

5 Fabrication and characterization of the sub-components in the cascaded superlens

Simulation results have shown a possibility for direct imaging of an object with subwavelength features with our designed cascaded superlens. To experimentally verify the calculation results, the structure is going to be fabricated with our existing nano-fabrication facilities. In this chapter, the fabrication facilities and processes will be described first. Afterwards, fabrication and characterization results of the structured sub-components will be presented as a preparation for the stacking of the cascaded superlens.

5.1 Introduction to fabrication facilities and processes

5.1.1 Film deposition techniques

a) Thermal and E-beam evaporation

Vacuum evaporation is a conventional method used to deposit thin metallic or dielectric films on the surface of a substrate, which generally has two steps: the material to be coated is first evaporated; then, the vapor is condensed onto the surface of the substrate [123]. In this dissertation, vacuum evaporation methods were chosen to deposit Ag, Cr and MgF₂ films, which are the key materials used for the cascaded superlens.

The evaporation methods we have used are thermal evaporation and electron beam evaporation (E-beam evaporation). The working principles for the two methods are illustrated in Fig. 5.1. With the thermal evaporation method, the material is filled in a boat of semi-metal, which has a much higher melting temperature than the material itself. A high current intensity flowing through the boat heats the material. As to the E-beam method, electrons are accelerated to a high kinetic energy and directed towards the evaporation material. Upon striking the evapora-

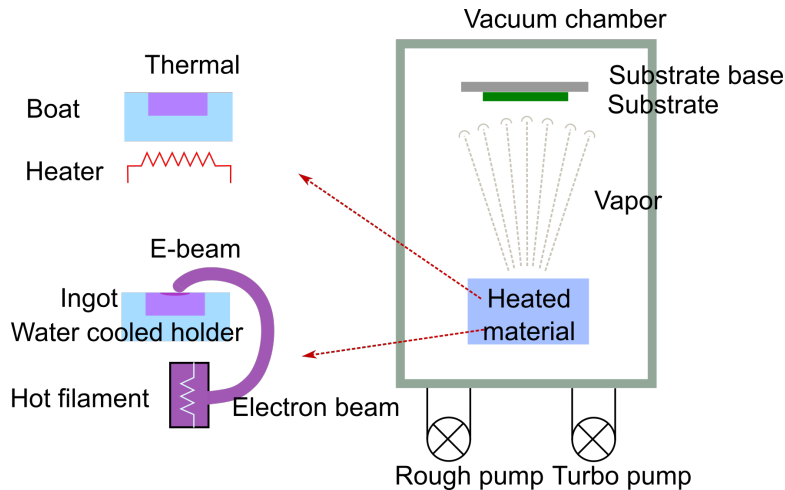


Figure 5.1 Illustration of an evaporation deposition chamber. The top left element is for thermal evaporation and the bottom left is for the E-beam evaporation.

tion material, the kinetic energy of the electrons is partially converted into thermal energy that heats up the evaporation material causing it to melt or sublimate [124]. The resulting vapor is then deposited on the surfaces of samples. In order to get a homogeneous and pure film, the mean free path of the molecules or atoms should be much longer than the distance from the material to the substrate. For this work, both thermal and E-beam evaporation machines (the latter is from Pfeiffer Vacuum, Inc) were used.

b) Spin-coating method

Spin-coating technique is used to obtain uniform coatings of liquid organic materials, which is often applied for photoresist based lithography in the microelectronics industry. Fig. 5.2 illustrates the working principle of a spin-coater.

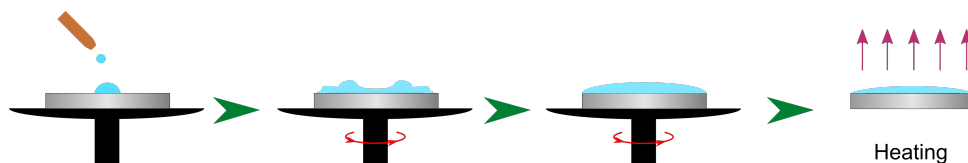


Figure 5.2 Schematic of a spin coating process.

A spin-coater is mainly composed of a rotation stage, the rotation velocity of which is adjustable. The sample to be coated is placed on the center of the stage. The viscous organic liquid is distributed over the whole sample by centrifugal forces induced by the stage rotation. The thickness of the film is inversely proportional to the rotation velocity of the stage and the square root of the duration time of the rotation process [125]. After spin-coating, the sample will be baked to remove the excessive solvent. In fabrication of the cascaded superlens, the

spin-coating is mainly for planarization of the substructures to be fabricated on top of the other, which requires the coating material to be hard enough or resistant enough for further fabrication. For this work, we use a spin-coater M-SPIN 200 from Ram Graber to obtain a thin layer of Spin-on Glass (SOG, IC1-200, Futurrex, Inc) on a glass substrate or on a patterned substrate. The thickness of the SOG was mainly controlled by the portion of solvent n-Butanol (ACROS Organics).

5.1.2 Focused ion beam system for nano-fabrication

Focused Ion Beam (FIB) milling system has been applied extensively for micro- and nano-fabrication in the semiconductor industry and material science research [126–129]. In the fabrication, we use a dual beam FIB system Helios NanoLab 600 from FEI company [130]. It is called dual beam system since it is combined with a Scanning Electron Microscope (SEM), which can be used to monitor the milling results during and after the process.

In our FIB system as shown by the schematic in Fig. 5.3, a liquid gallium source is used to provide charged ions. The Ga source is heated close to its evaporation temperature and is ionized. The ionized particles are then drawn by an annular electrode e.g. extractor, into the chamber of the FIB system. Ions are directed into a magnetic lens system so that they are accelerated under a high voltage to a high velocity [131]. When a magnetic lens is used to focus the ion beam, an extreme strong magnet field or a long focusing distance is needed. Therefore, an electrostatic lens is normally used to decrease the focusing distance as in our FIB system [130]. It is composed of several built-in electrostatic fields toward the center of the column and can focus the ions more effectively. The current of Ga^+ is tunable from 9 pA to 4.3 nA and the acceleration voltage of Ga^+ beam can be varied from 5 kV to 30 kV.

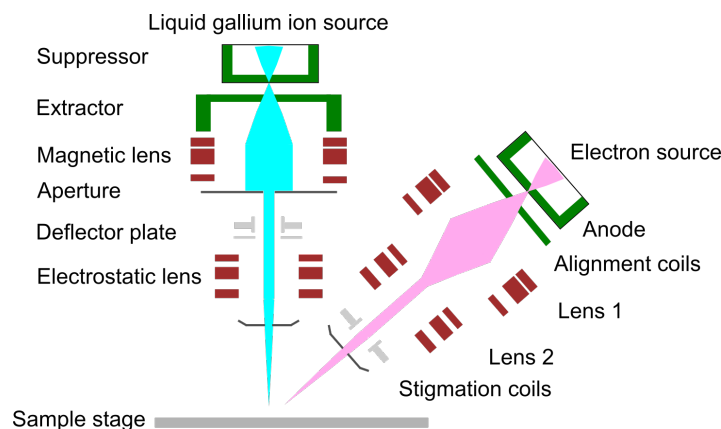


Figure 5.3 A schematic diagram showing the configuration of a dual-beam focused ion beam system.

In this system, the electron and ion beams intersect at an angle of 52° at a particular point near the sample surface. The SEM can provide a high resolution image during or after the FIB milling with less damage to the sample surface compared with the ion beam. The chamber vacuum in operation is around 10^{-6} mbar. Theoretically the best resolution of the electron beam is 1 nm and that of the ion beam is 7 nm.

5.1.3 Optical characterization methods

a) Fourier transformation infrared spectroscopy

The Fourier Transform Infrared (FTIR) Spectrometer is widely used to analyze optical spectral spectrum based on a Michelson interferometer. In this thesis, the FTIR spectrometer Vertex 80v of Bruker Company was used to measure the transmittance spectra of single- or double-layer meander structures. The FTIR can work from far infrared to ultraviolet frequencies. Its spectral resolution can reach 0.2 cm^{-1} at ambient pressure and room temperature. A peak resolution of 0.07 cm^{-1} can be achieved at low pressure and temperature. For our measurements, a wolfram glow lamp as a light source and a CaF_2 beam splitter were used. The lamp emits light in a spectrum range from 1200 cm^{-1} to 15550 cm^{-1} and covers the frequency range we are interested in.

b) Aerial image scanning microscope

An aerial image scanning microscope was built at our institute to measure the transmitted field distributions. Schematic of the self-built setup is shown in Fig. 5.4. The sample is mounted on an *xyz*-piezo stage (TRITOR 102 - XYZ Nanopositioners, piezosystem jena GmbH) and is illuminated by a collimated laser light at $\lambda = 640 \text{ nm}$ (QiOptiq, iFLEX-iRIS). The transmitted light will first pass through an object lens with a focus length of $2 \mu\text{m}$ and $\text{NA} = 1.3$ in oil. Then the beam is divided into two by a beam splitter: one passing through Lens-1 ($f = 100 \text{ mm}$) and collected by a CCD camera (Sony, XC-77RR or FLIR, BFS-U3-51S5M); the other passing through Lens-2 ($f = 164.5 \text{ mm}$) and collected by a photo detector (THORLABS, Avalanche Photodetectors APD120x). By controlling position of the piezo stage, field intensity at corresponding positions can be obtained.

The field distribution collected by the photo detector is integrated with a pinhole (diameter: $25 \mu\text{m}$) located in front of it, which is used to restrict the pupil size in order to obtain a transmitted intensity of a smaller area and protect the detector from optical damage. The power of the incident laser is 50 mW, and behind the pinhole is only 40 nW which is much smaller than the threshold of the detector (1 mW). With the photo detector, detailed information can

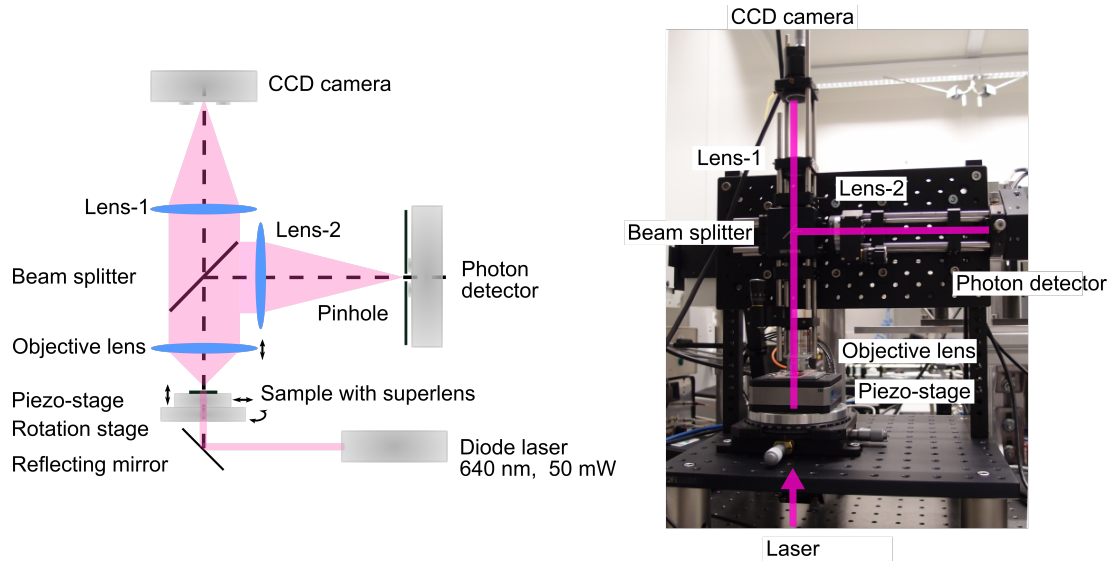


Figure 5.4 Schematic and set-up of an aerial image scanning microscope.

be obtained (step sizes of the piezo stage can be smaller than 25 nm), however, the signal is heavily influenced by noise. The CCD camera on the top side is further applied to measure field distributions along the xy -plane, in the meantime to observe the sample. The pixel size of CCD cameras are 11.5 (Sony) or 3.45 (FLIR) μm with a spatial resolution of 115 or 34.5 nm for this set-up.

5.1.4 Fabrication processes

As the design shown in the former chapter, to realize fabrication of the designed cascaded superlens with available equipment, following nano-fabrication steps will be performed as shown in Fig. 5.5:

1. A layer of 100 nm SOG is first spin-coated on a cleaned glass substrate. The rotation stage is accelerated to 3500 RPM and remains for 30 seconds to distribute the liquid over the whole substrate, thus a homogeneous coating is obtained. The thickness of the coating is mainly controlled by adding different portion of solvent and the coated sample is baked at 200°C in nitrogen for one minute to remove the solvent.
2. Silver and chromium with thicknesses of 20 and 10 nm are evaporated separately on the top of the SOG as a sacrificial layer for FIB milling process, which requires an electrical conductive surface.
3. A periodical grating with a proper duty cycle and ridge height is milled into SOG as a pre-pattern for the meander structure, of which the depth and width can be tuned. The duty

cycle can be roughly checked with SEM imaging, as well as the ridge height. For a more precise characterization, an optical verification process will be conducted additionally.

4. The sacrificial layer is then removed with corresponding chemicals: chromium etch (Technic France) for chromium layer and a mixed acid with a volume ratio of water: hydrochloric acid (37 %): nitric acid (70%) =1: 1: 1 for silver.
5. To obtain a DLMC structure, films in a sequence of Ge (1 nm)/Ag (30 nm)/MgF₂ (80 nm)/Ge (1 nm)/Ag (30 nm)/MgF₂ (5 nm) are deposited. Ge works as a wetting layer to assist the formation of a continuous and smooth silver layer and MgF₂, which has similar refractive index as the SOG, is used to adapt the aspect ratio of the fabricated gratings and as the spatial layer between the two meander layers.
6. Another layer of SOG is spin-coated on the top of the DLMC structure to planarize the surface. For the fabrication of the cascaded superlens, this layer of SOG works as a spacer between the DLMC and the PPL structure. For optical characterization, a layer of SOG helps to improve the transmission efficiency of the DLMC structure.
7. Afterwards, a layer of 395 nm silver and 5 nm chromium are evaporated for fabrication of the PPL structure. The extra chromium is used to protect silver from oxidation.
8. In the end, the fabricated cascaded superlens is obtained after the milling of the PPL structure with FIB.

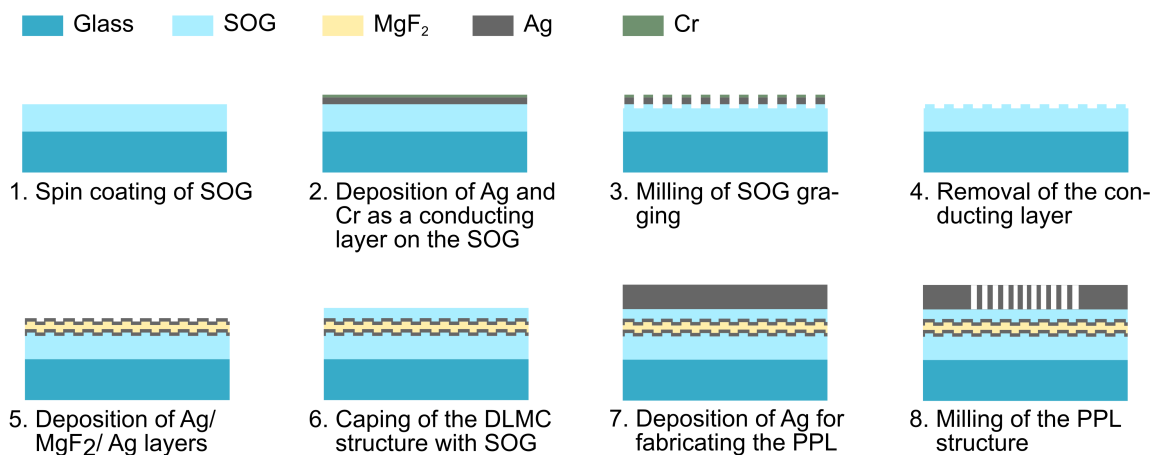


Figure 5.5 Steps of the fabrication process for the cascaded superlens.

5.2 Preparation for the fabrication

Though the fabrication possibility has already been considered during simulation, the sizes of structures in the cascaded superlens are only sub-micrometers, which makes it challenging to accomplish the superlens in experiment. Before fabrication, each of the separate part was tested to avoid undesired defects that may be introduced by the fabrication and the parameters are optimized in the meanwhile.

5.2.1 Challenges in the fabrication process

To experimentally obtain a cascaded structure with desired function, several points have to be taken into account and optimized first:

1. Thickness of silver layer for sacrificial or meander layer is only 20 ~ 30 nm. It is hard to form a continuous film with these thicknesses. The cracks or the clusters appeared in the film will deform the fabricated grating in milling steps and optical properties of the structure. Therefore, before the fabrication, the evaporation results of the thin films are examined and optimized in case of the influence brought by cracks or clusters in the metal film.
2. The width of the slits in the PPL structure is only tens of nanometer, while the depth is 400 nm in our design, which is already an optimized result considering the possibility in fabrication. However, it is a challenge to mill deep slits with such a high aspect ratio in soft materials with low melting temperature like silver, which will result in deformation.
3. For the spacer between object, the DLMC structure and the PPL structure, PC403 was the first choice, due to its better performance in planarization. However, the material is too soft to hold other structures to be fabricated on top of it. Therefore, SOG is an alternative choice and will be tested further.

In the following sections, the solutions to these problems are going to be illustrated.

5.2.2 Deposition of metallic films

A smooth and continuous film will help to guarantee that the optical properties of the fabricated structures behave as the design, especially for the cascaded superlens, the size of which is of nanometers with a film thickness of 20 or 30 nm. To fulfill the requirement, a thermal evaporator was the first choice due to its wide application for both metal and dielectric materials, higher

vacuum (10^{-6} bar) and good performance in deposition of thin film. However, due to some technical reasons, E-beam evaporator was chosen as an alternative, with which the evaporated material is sometimes not as good as that of thermal evaporator but can be optimized with wetting materials.

According to references [132–134], the deposition results of a thin film can be more smooth with less optical loss by the assist of a wetting layer germanium. A preliminary test was conducted to check the film quality of thin film evaporated by E-beam evaporator with the wetting layer. First the SEM images of 30 nm silver film were taken and presented in Fig. 5.6. All the SEM images were captured under same magnification factor. It can be seen that without wetting layer, rough surface with clusters is obvious no matter it was evaporated directly on glass or on SOG. However, an additional layer of Ge is significant in killing the clusters and with which we can obtain a silver film with smoother surface.

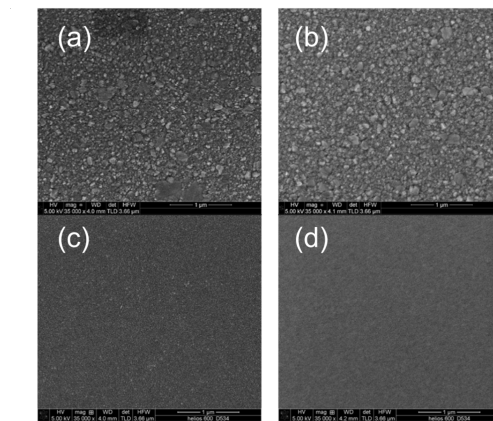


Figure 5.6 SEM images of 30 nm silver films evaporated with E-beam evaporator: (a) On glass; (b) On SOG; (c) On glass with wetting layer; (d) On SOG with wetting layer.

Transmitted spectrum was measured with FTIR to check its optical properties as well, with which the influence of the film quality is more obvious. From the curves illustrated in Fig. 5.7, we can see that the clusters influence the transmitted spectrum by introducing background noise and the measured spectrum of the one with smoother film agrees very well with the simulation, which was calculated with Microsim and the refractive index of glass is 1.48, that of SOG is 1.41 and that of silver is taken from John-Christy model [122]. The layer of Ge was not taken into consideration because 1 nm deposited Ge is too thin to form a continuous film. Thickness of the SOG is 80 nm in Fig. 5.7(b). The comparison between the simulation and measurement further illustrates that a thin layer of Ge (only 1 nm) has nearly no influence to the transmitted spectrum.

In the meanwhile, a thinner film of 20 nm silver was checked as well due to a fact that in the design the thickness of meander is in between 20 to 30 nm. The SEM images and the

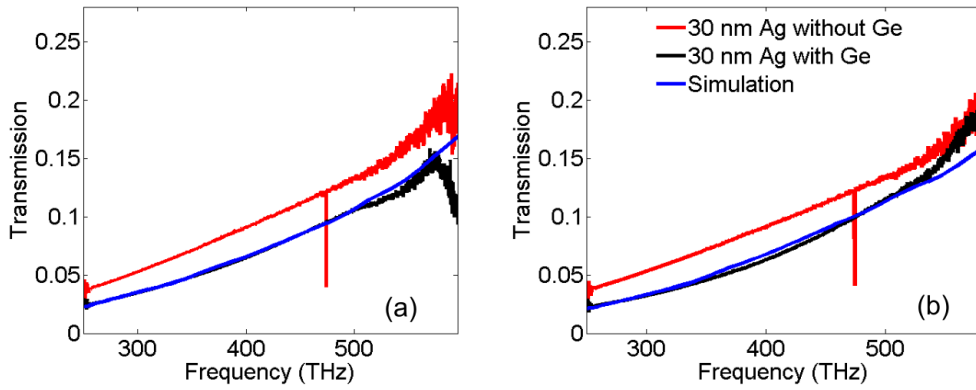


Figure 5.7 Comparison of transmitted spectrum between simulations and measurements of 30 nm silver: (a) on glass substrate; (b) on SOG.

transmitted spectrum comparisons are illustrated in Fig. 5.8. Other than the clusters on 30 nm silver film, when the thickness decreases to 20 nm, cracks appear instead of the clusters and are especially obvious for the one deposited on SOG. These defects influence not only the property of metal film but also the milling results when it is used as sacrificial layer. However, with the wetting layer, these cracks and clusters are killed and the surface of films turns as smooth as that of 30 nm films. A good agreement is obtained between the simulation and measurement.

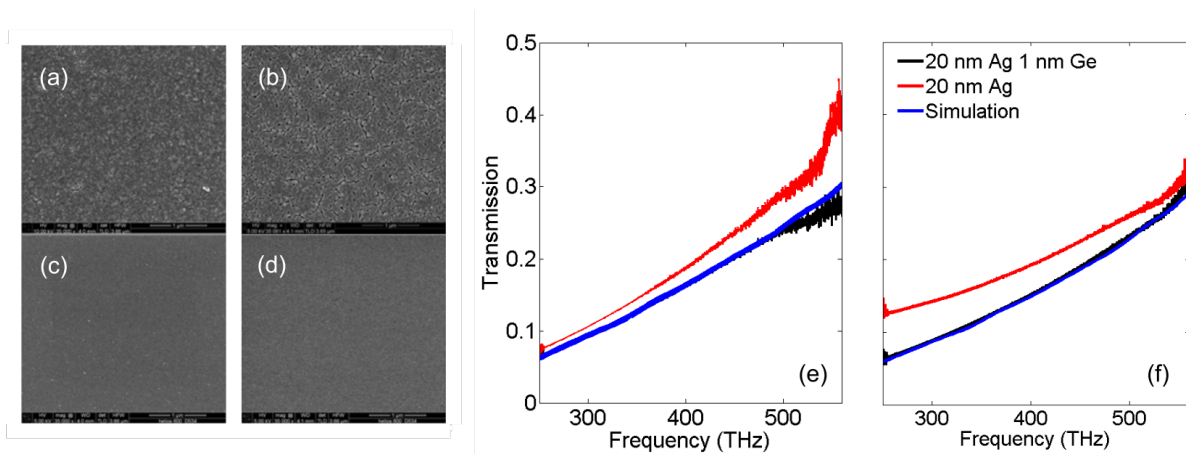


Figure 5.8 (a) - (d) SEM are images of 20 nm silver films evaporated with different conditions and comparison of transmitted spectrum between simulations and measurements: (a) On glass; (b) On SOG; (c) On glass with wetting layer; (d) On SOG with wetting layer. (e) - (f) are spectra of the film evaporated: (e) on glass; (f) on SOG.

For the sacrificial layer, the cracks in the deposited thin film will make the grating milled onto it irregular. A comparison between milling results with continuous and discontinuous film is illustrated in Fig. 5.9, of which the differences of the fabricated grating are obvious. These obstacles will deform the shape of the meander, which is evaporated and formed on the

grating, and the deformation will affect the optical response e.g. the loss of the long range surface plasmon (LRSPP) at higher frequencies.

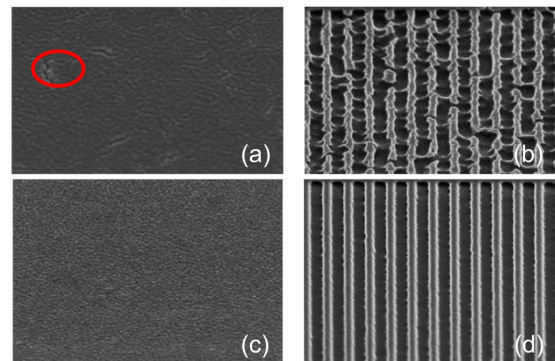


Figure 5.9 Influence of films to the milling results: (a) and (c) are the evaporated films with and without cracks separately; (b) and (d) are milling results on (a) and (c) correspondingly.

To further improve the transmission of silver films, annealing was also suggested [134]. The transmission efficiency increased when the sample was heated at 200°C for 2 or 3 minutes in nitrogen. The influence of the annealing is more obvious when measuring the spectrum of single meander structure as illustrate in Fig. 5.10(b). However, there is abnormal bright and dark spots on the surface of the silver film in SEM image compared with that obtained directly after deposition (e.g. images shown in Fig. 5.8).

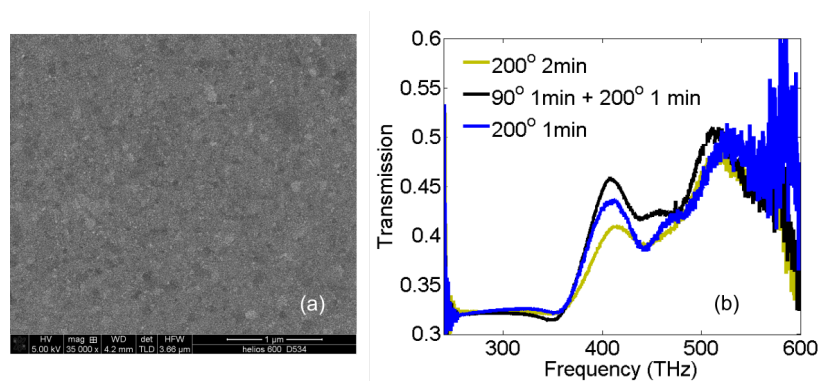


Figure 5.10 (a) SEM image of silver surface after annealing; (b) Spectrum of meander with different annealing time and temperature.

In addition, when the silver is heated on a hot plate less than 200 degree for 1 minutes, the surface remains nearly unchanged and almost no oxidation to silver layer according to references [135–137]. However, when the heating time was extended, some cracks appear as shown in Fig. 5.11(c). During the fabrication, any long last heating process should be avoided as well.



Figure 5.11 SOG spin-coated on meander structure: (a) Image after spin-coating; (b) Image after heating 2 min at 200 degree; (c) Image after heating 5 min at 200 degree.

Considering both of the possibilities of silver oxidization and the time requirement of the SOG under high temperature (spacer between the DLMC and the PPL structures), the annealing was not applied in fabrication of the cascaded superlens.

5.2.3 Focused ion beam milling

The smallest size of the cascaded structure is only tens of nanometers. To obtain a fabrication result that can realize the desired function, milling parameters were tested in advance. Take the PPL structure as an example, a cross section was cut into the structure for a clearer view of the milling results as shown in Fig. 5.12. The cross section image is viewed at a tilted angle of 52° and was prepared by ion beam milled with small current to decrease distortions of the fabricated slit. In the SEM pictures the bright material is silver with same thickness as the design, on top of which there is another layer of 5 nm chromium in afraid of oxidization during the transfer of the vacuum chambers from evaporator to FIB. The fabricated results shown in Fig. 5.12 are milled with same parameter but one is out of focus while the other is in good focus. It can be concluded that focusing of the ion beam is a condition that heavily influence the milling results but cannot be evaluated by measurements. A worse problem is that the size of focus point of the ion beam varies with its lifetime, which requires to adapt the fabrication every time.

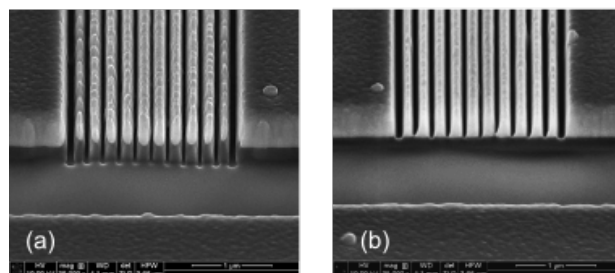


Figure 5.12 Fabricated PPL structures without (a) and with (a) good focus of the ion beam.

Other than the focusing point, milling parameters need to be tested as well, especially for the defined depth. The milled material and size of structure can be defined in the interface of the FIB, however, the real size of the structure is different from the defined ones due to the mutual influence between each other. In the vacuum chamber, the milling results can only be seen by SEM or ion beam image with help of cross section, which in contrary will destroy the shape of the structure and influence its optical response. Therefore, parameters have to be tested and optimized in advance to obtain a structure with desired size. Take the meander structure as an example, the depth of which is only tens of nanometers. The fabricated meanders were preliminary checked by the cross section image. In Fig. 5.13, the three pictures are the cross section of the single layer meander, on top of which are gold serving as a conducting layer evaporated by a sputtering machine (used only for SEM images). The bright lines are the corrugated silver film. In the preparation, a series of parameters were tested to find an optimized combination of the parameters, with which we can obtain a continuous meander with respected aspect ratio.

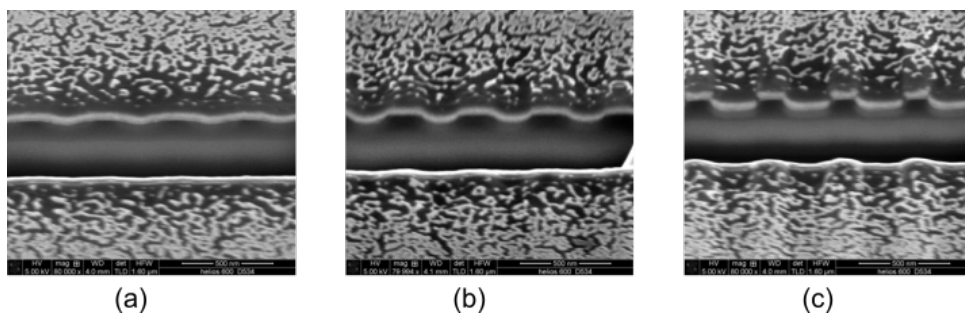


Figure 5.13 Cross section images of single layer meander structures milled with different defined depth (numbers of milling times at same position): (a) 900; (b) 1000; (c) 1100.

The milling results using ion beam are sensitive to the stability of the surroundings. The results with the same milling parameters may be different. Fig. 5.14 shows SEM images of pair-slit milled at different time. Therefore, a test is necessary every time before and during the milling of the large area structures.

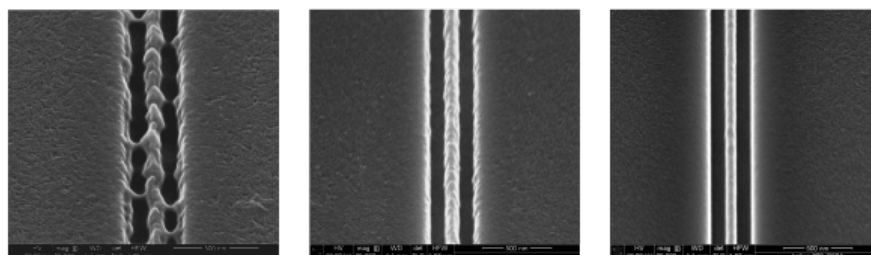


Figure 5.14 Pair-slit milled with the same parameters at different time.

There are still other parameters, such as milling sequence, overlapping steps etc, that will influence the milling results. Since their influences are not as strong as with the given examples, the results are not illustrated or compared in this dissertation. Instead of silver, gold was tested as an alternative material, which is more chemically stable. For example, a smooth and continuous sacrificial layer can be obtained with less gold and without protection layer of Cr, which helps decrease the milling time accordingly with updated milling parameters. However, the thickness of the sacrificial layer influences the milling results as well as illustrated in Fig. 5.15. Considering that gold is much more expensive than silver and there is no obvious improvement for the fabrication when used as sacrificial layer, gold will not be used further in the fabrication.

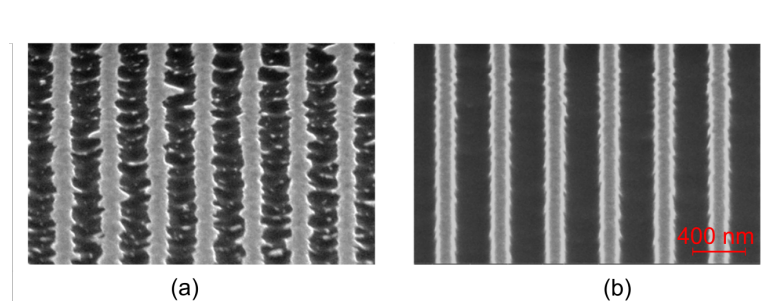


Figure 5.15 Milling results of gratings with different thickness of sacrificial layer: (a) 10 nm Au and 5 nm Cr; (b) 20 nm Ag and 10 nm Cr.

After optimizing the milling process, milled results with optimized parameters and good stability can be obtained as the example shown in Fig. 5.16 published in reference [119]. The fabricated structure, which consists of 16×16 individual meander structure and each with a size of $50 \mu\text{m}^2$, is continuous and homogeneous .

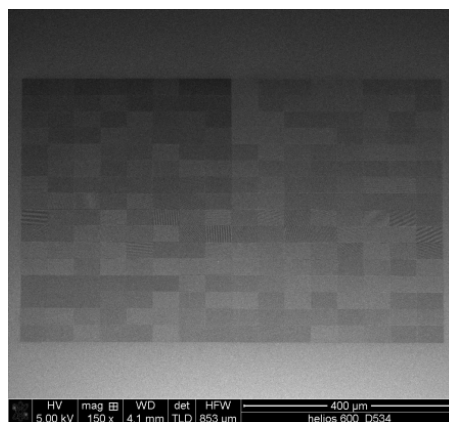


Figure 5.16 $800 \text{ by } 800 \mu\text{m}^2$ meanders with different grating orientation angles.

5.3 Characterization of the fabricated sub-components in the cascaded superlens

the cascaded superlens

Other than the SEM cross section image, optical properties are further measured according to the characters of each sub-components in the cascaded superlens described in subsection 3.1.1 with parameters optimized in section 4.2.2 to check the fabrication results.

5.3.1 Characterization of the fabricated DLMC structures

The optical spectrum of the meander structure is sensitive to its geometrical parameters. Therefore, the transmission spectrum is measured as a compensation for the optimization of the meander structures. A single layer meander structure is fabricated and characterized first as to its basic fabrication process and higher transmission frequency (compared with the double one). Except for the wetting layer of Ge, a thin layer of MgF_2 is evaporated to chamfer the rectangular corner to avoid cracks and to tune the width of grating. After the deposition of silver layer, another layer of MgF_2 is again evaporated to protect the silver film from oxidization. The deposition sequence of the materials is illustrated in Fig. 5.17. Before optical characterization, the surface of both single layer and double layer meander structures was planarized with an additional layer of 80 nm SOG for purpose of a homogeneous dielectric environment, which has functions of protecting silver from oxidation and increase the transmittance [138].



Figure 5.17 (a) Fabrication procedure of one layer silver meander structure; (b) Cross-sectional SEM image of a fabricated single layer meander structure.

The shape of the fabricated structure with optimized parameters is shown by the cross section SEM image in Fig. 5.17(b). The cross section of the corrugated Ag film (the corrugated bright lines in the figure) reveals a smooth meander shaped metal film symmetric in the normal direction. We see that the designed geometrical parameters in terms of metal thickness, grating height and aspect ratio have been achieved.

To further check the optical property of the meander structure, spectrum was measured using FTIR spectrometer at visible and near-infrared wavelength ranges as shown in Fig. 5.18. The

measured structure size is $50 \times 50 \mu\text{m}^2$ and the measured transmittance spectrum in Fig. 5.18(a) is larger than 40% at the passband, which is more than half of the numerical results shown in Fig. 5.18(b). The deviation from the ideal curve may be induced by the surface roughness of the grating sidewalls. However, since the characterization peaks and valleys are obvious in the curve and the transmitted intensity is largely improved during the optimization, it is convinced that the fabricated meander is good enough for further fabrication.

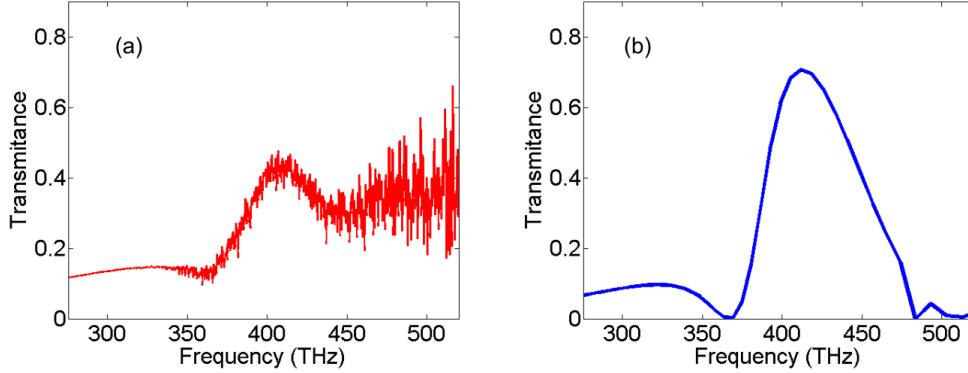


Figure 5.18 (a) Measured spectrum of a fabricated single meander; (b) Simulation with designed parameter ($d=30 \text{ nm}$ and $t=50 \text{ nm}$).

For the fabrication of a double layer meander structure, we first repeated the total fabrication procedure (starting from spin-coating) of the single layer meander structure on top of the first layer with corresponding thickness of spacer of SOG between the two layers. However, the SOG spin-coated on the previously fabricated corrugated film is not thick enough to protect the first layer. When we removed the sacrificial layer of the second grating with chemical etching, part of the silver in the first layer was etched away in the meantime. In addition, it is quite hard to align the ridge of the second layer exactly on top of the first layer when the size of the structure is of hundred nanometers and a position shift will change the optical response of the structure.

An alternative method for fabrication of the second layer meander structure is by deposition further layers of MgF_2/Ag on the first layer in the same film deposition run. MgF_2 has similar refractive index as that of the SOG and is used as a spacer layer. Silver is the metallic corrugated film. The aspect ratio of the top layer is not the same as the bottom one, however, a good conformity of the top layer with the bottom layer can be seen in the cross section image shown in Fig. 5.19 and further checks of the transmittance spectra show that the influence is quite small and can be ignored.

The measured spectra approximately agree with those of the calculated. The noisy signal at shorter wavelengths is due to the weak sensitivity of the silicon photo detector and small size of the structure to be measured. The transmittance peak with the double-layer structure is around 4% instead of approximately the square of the transmittance from the single layer,

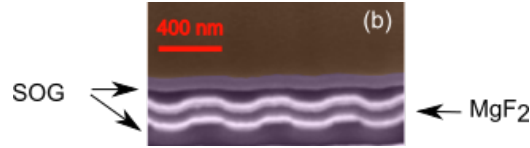


Figure 5.19 A cross section image of a DLMC structure cut by ion beam milling and captured by the SEM.

which is attributed to the near-field interaction as we have shown in [116], since the cavity has only a distance of 70 nm. The discrepancy between the measured and calculated curves can be explained by different illumination configurations. With the FTIR spectrometer, an objective lens with $NA = 0.4$ was used. Hence, the sample was illuminated by a focused light, but not a plane wave as with the simulation. As a result, the measured spectra from the meander structures are rounded at the passband edges. This also red-shifts the spectra since the dispersion of the plasmonic meander structure is negative [116]. When a well collimated light source was used for the measurement, as we have performed in [119], a much better agreement between the simulated and measured curves could be obtained. However, for that measurement a much larger structured area (0.8 by 0.8 mm²) was required. Nevertheless, based on our experience with previous studies, current results demonstrate that the quality of the fabricated DLMC structure is sufficiently good.

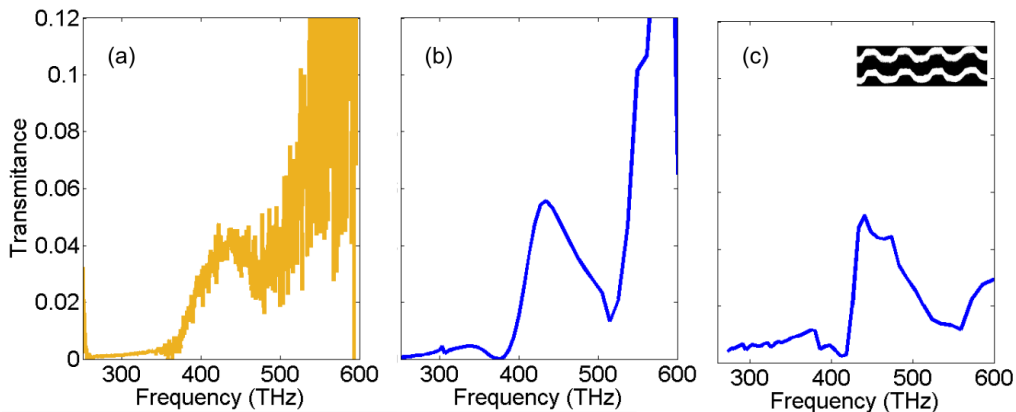


Figure 5.20 Spectrum of a double layer meander structure with designed parameter ($d=30$ nm, $t=50$ nm, period= 400 nm and $D_{spa}=70$ nm): (a) Measurement; (b) Simulation; (c) Calculated spectrum with measured structure. Inlet: binary of the cross section image.

As a supplementation, a further simulation is performed using the structural shape and parameters taken from cross-section image. To derive them, the cross section image is first changed to a binary picture. Then the bright line of the image is taken as silver film and the rest as SOG. In this way, the model for simulation has a more similar shape as the fabricated results compared with the geometrical model. The calculated transmitted spectrum is shown in Fig. 5.20(c),

which is similar to the spectrum in Fig. 5.20(b), except for a blue shift of the spectrum. The simulation result further explains the influence of the structure shape to the spectrum shift between the measured and calculated results as well.

Gold was also tested for the meander structure due to its better chemical stability, with which the noise at higher frequency decreases with same size of the sample and measured parameters as shown in Fig. 5.21. However, the transmission of this part is relative higher and the resonance at LRSPP (about 450 THz) is not as obvious as that of silver.

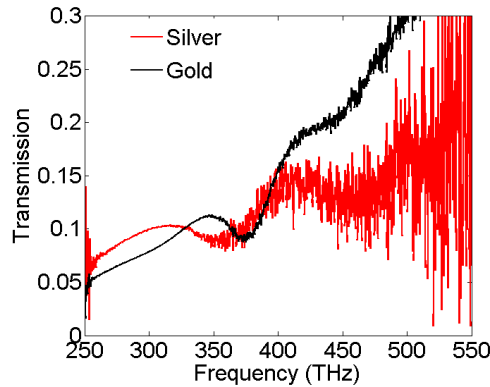


Figure 5.21 Transmittance spectrum of the fabricated DLMC structures with different materials.

5.3.2 Optical verification of the fabricated PPL structure

An SEM image of a fabricated PPL is shown in Fig. 5.22(a). The size of the nano-slits was measured with SEM as well, although with some uncertainty. The measured parameters are close to the design shown in Chapter 3.3 Section 3.3.2. To further investigate the fabrication results, a cross section was cut into the structure as illustrate in Fig. 5.22(b). The sidewalls are straightforward and vertical from top to bottom with well-defined depth. For the fabrication of the PPL structure, the high aspect ratio milled into a soft thick silver film makes it difficult to obtain a fabrication results same as the design. Therefore, the aerial image scanning microscope is used to check the transmitted field distribution of the PPL structure, with which we can clearly test whether the phase compensation introduced by the fabricated nano-slits is in a good quality to realize the focusing function with a plane incident wave or not.

In the characterization process of the PPL structure, two separate PPL structures are milled on the same sample: one for the cross section SEM image and the other for optical verification. As the results illustrated in the former section, the FIB sometimes may be sensitive to the surrounding or the milling time. The two structures were prepared with identical milling parameters one after the other to decrease the aberrations that might be introduced.

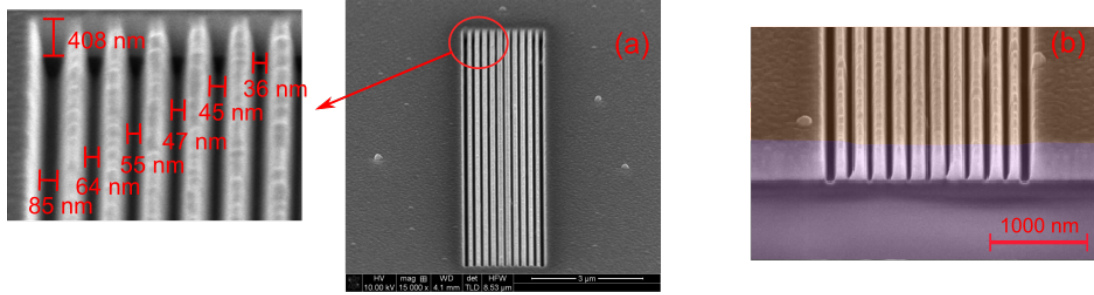


Figure 5.22 (a) SEM image of fabricated PPL with measured parameters; (b) Cross section of the PPL.

The fabricated PPL structure was placed on the piezo stage and protected with immersion oil. In the measurement, the incident light comes from bottom side of the PPL structure and the signals were collected by the photon detector as the set-up introduced in subsection 5.1.3 with steps of the piezo stage: 39 nm horizontally and 5 nm laterally. The simulation result is plotted in Fig. 5.23(b) with the designed parameters introduced in section 3.3 and the measured field distribution in the xz -plane behind the fabricated PPL is plotted in Fig. 5.23(c) for a better comparison. For the measured results, several frames were added together to avoid the measurement error and it can be seen that a well-defined focus with the desired focal length is obtained. For a more clear comparison of the measurements with the simulation results,

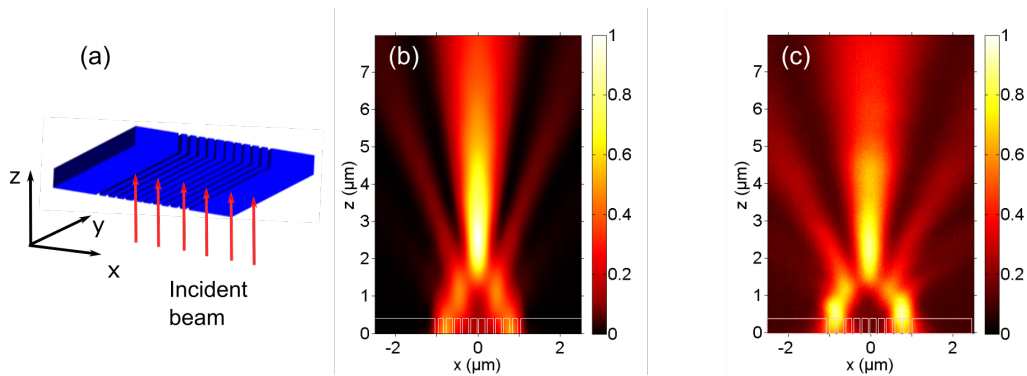


Figure 5.23 Focusing of the PPL: (a) Schematic for the measurement; (b) Simulation results; (c) Measurement results.

intensity variation along different directions are further plotted in the Fig. 5.24. The positions of each curve are shown in the figure caption. By the comparison between the measured and simulated results, we see that a very good agreement is obtained. The fabrication was well controlled and its influence to optical property is in tolerance. PPL structures with other parameters were also fabricated and tested as an alternative and the results are shown in Fig. 5.25. The parameters of each structure are shown in the figure caption.

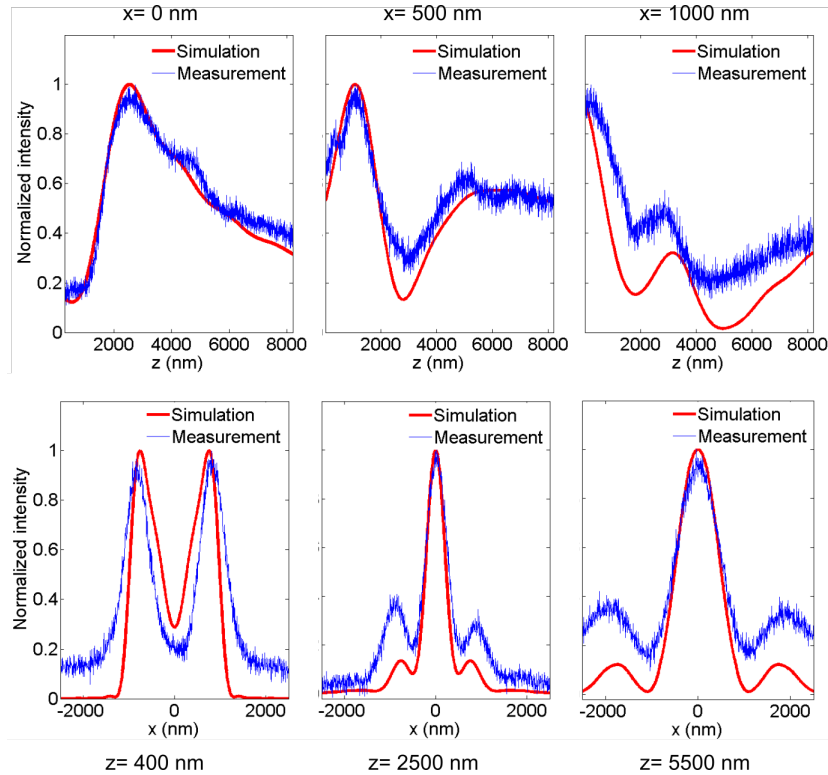


Figure 5.24 Comparison between simulation and measurement: first row along the z -axis and second row along the x -axis with respective position in Fig. 5.23.

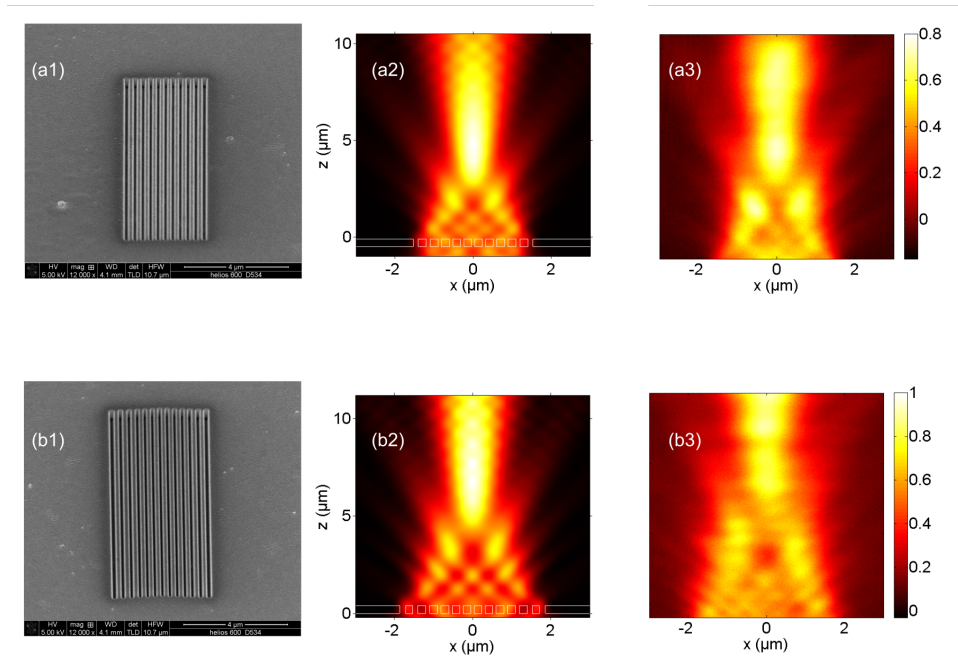


Figure 5.25 (1): SEM images of two alternative PPL; (2) Simulated and (3) measured field distribution of PPL with parameters: (a) Slit-widths of 120, 100, 90, 80, 80, 80, 80, 90, 100, 120 nm with distance of 280 nm and focus of $5 \mu m$; (b) Design of (a) plus extra slits with width of 150 nm at x -position of -1790 and 1790 nm and focus of $7 \mu m$.

At higher position of the measured field (in Fig. 5.25(a3) and (b3)) for the alternative PPL, there is an abnormal bright area at about $z = 8 \mu\text{m}$. This appears for the reason that the oil of immersion lens breaks into two parts while shifting the piezo-stage along z-direction. The focus of the alternative PPL is longer, which requires a larger distance between the objective lens and the PPL structure in the measurement. Furthermore, the obtained detailed features near to the metal surface are obvious for these PPL structures with larger aperture diameter. Same conclusions as the previous PPL structure with smaller focal length can be obtained and indicate a precise nano-fabrication with good repeatability of the PPL structures as well.

5.4 Assembly of the cascaded structure with a dielectric spacer

In between the two parts of the cascaded superlens, a dielectric material is used as a spacer, which is able to planarize the surface of the meander structure as a preparation for the PPL structure to be fabricated on top of the DLMC structure. In the fabrication, PC403 or SOG are used as the spacer. Fig. 5.26 is a cross section image of a fabricated superlens, from which we can see the PPL structure is planar in agreement with the designed shape and the distance between the DLMC structure and the PPL structure is about 100 nm, which is well controlled. The field of view of the cascaded superlens is limited by the PPL structure and it can be changed with proper design. To obtain a clearer view of the structure, an additional color mask is added to the image according to different planes each part locates as illustrated. In this thesis, cross section SEM images will be colored in the same way according to the plane each part belongs.

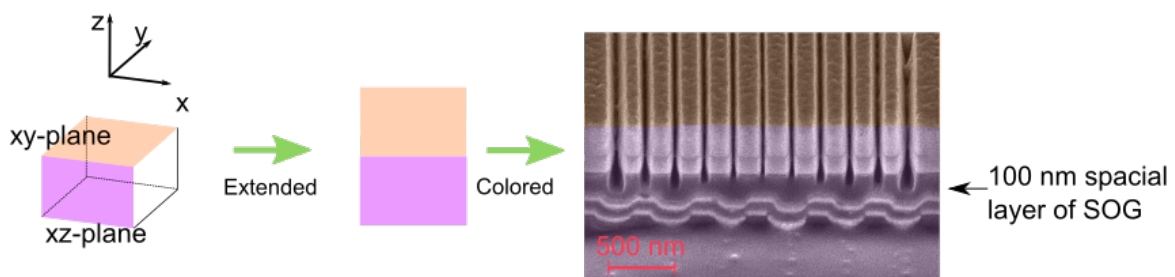


Figure 5.26 Cross section of a cascaded superlens fabricated on a glass substrate with parameters defined in chapter 3.

However, except the spatial layer between the DLMC structure and the PPL structure inside the superlens, in the verification experiment, a pair-slit serving as an object will be fabricated first under the superlens as the fabrication process illustrated in Fig. 5.27.

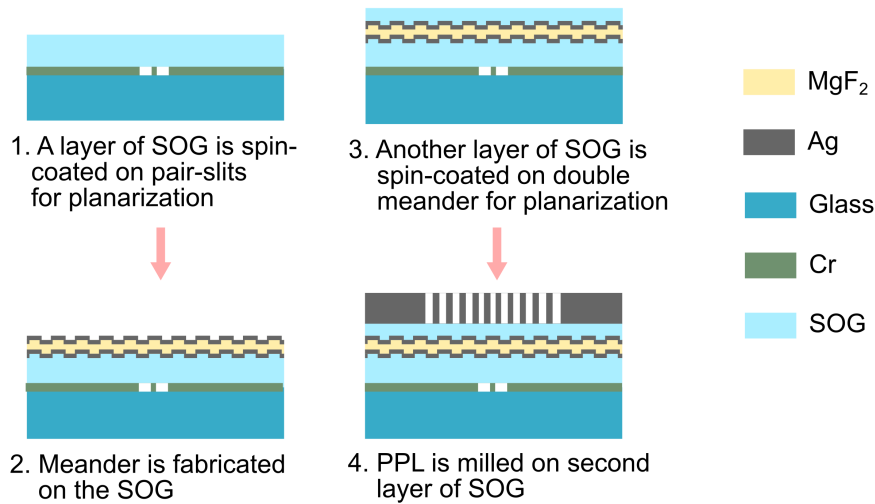


Figure 5.27 Fabrication process for the preliminary experimental verification.

The thickness of chromium for the object is 100 nm to ensure the transmitted field distributes as it is supposed to be and the milling depth is about double of that into the glass substrate. In this case, it is hard to use a thin layer of SOG to flat the object with deep depth. An explanation schematic is plotted in Fig. 5.28(a). To illustrate the influence when the object is not planarized, we use a slit with larger width as an example. The cross section image is shown in Fig. 5.28(b). The cascaded superlens to be fabricated on top of the object is deformed which may affect the optical properties of the superlens. In the verification experiment, the problem was solved by etching the SOG layer with a much thicker depth to ensure the superlens a planar shape as the design.

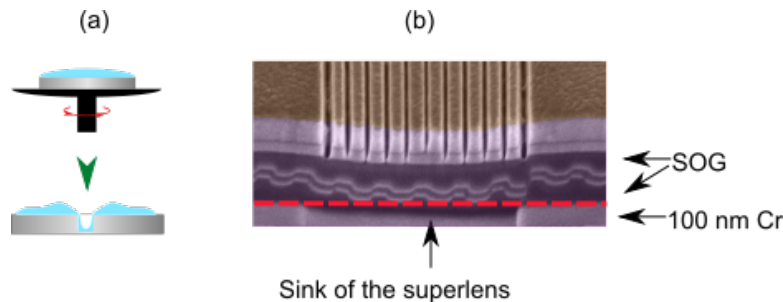


Figure 5.28 (a) Schematic of the spin coating on a slit; (b) Cross section of cascaded superlens fabricated on a groove.

An atomic force microscope (AFM) was used to measure the surface profile after planarization. A pair-slits with depth of 150 nm were milled into chromium layer and 70 nm SOG was spin-coated onto it. The surface profile is shown in Fig. 5.29(a). From the figure, we can see that a thin layer of SOG with desired thickness cannot fulfil the function of planarization for the pair-slit object. To solve the problem, a layer of SOG with thickness much larger than the

depth of slit is used instead. The AFM data shows that with a 700 nm thick SOG, the slits are better filled in the planarization step with a much more flat surface as shown in Fig. 5.29(b).

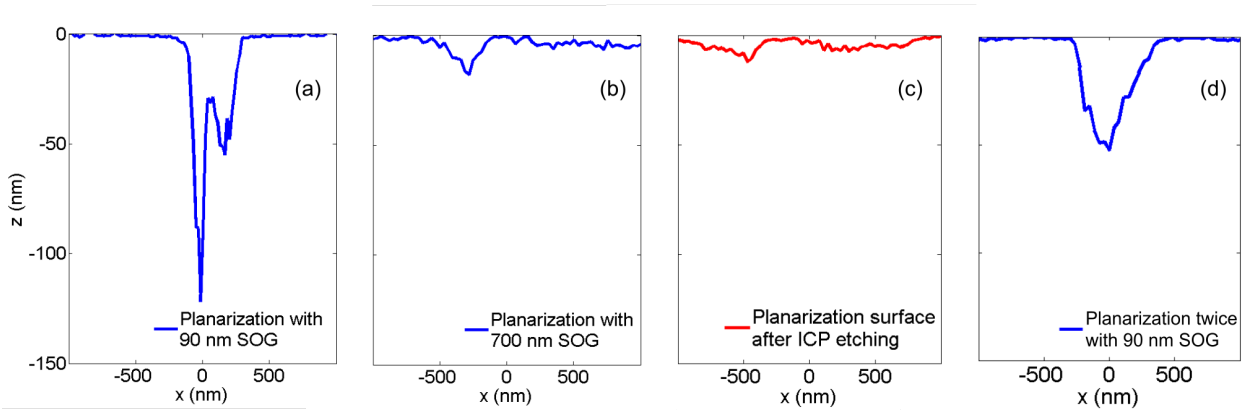


Figure 5.29 Surface roughness measured by AFM: (a) A pair-slits with planarization layer of 90 nm SOG; (b) Planarization by a layer of 700 nm SOG; (c) Etched with ICP-plasma etching to a desired depth; (d) Surface of the object planarized with SOG two times.

The thickness of the SOG is controlled by inductively coupled plasma - reactive ion etching (ICP-RIE, Sentech SI 500) etching process based on the usage of an inductively coupled plasma source, which generates a high-density plasma. Materials are etched with the reactive plasma under low pressure conditions, potentially combined with ion-induced etching. The etching depth can be controlled by the time, chamber pressure etc. The surface profile remains planar after etching as shown in Fig. 5.29(c), which is the desired result.

An alternative way to planarize the deep slit-object is cleaning the SOG layer on top of the object layer and then coating another layer of the SOG. With help of Q-tips, the SOG on top of Cr is removed but parts left in the slits. By repeating the process, the slit-object can be filled with a desired depth of the spatial layer. A result obtained after repeating the process twice is shown in Fig. 5.29(d). The structure with a sink of 50 nm is in tolerance when the total thickness of cascaded superlens is more than 600 nm. Compared with the long testing preparation using ICP, this method is more fast and convenient.

For convenience in the test, the cascaded superlens is fabricated on top of objects. In practical application, the cascaded superlens can be fabricated in advance and then attached to the objects with help of e.g. compress steps. Furthermore, the cascaded superlens can be fabricated with a larger size to obtain a wider view field with a modified design according to the lens size.

In the fabrication, the planarization of each sub-structure additionally adds difficulty to fabricate another structure at the right position on top of the early one. To solve the problem, several rectangular with larger sizes (2×1 or $5 \times 5 \mu m^2$) were milled as a mark to illustrate the

position of each structure. Furthermore, to decrease the alignment problem between each layer, an array of structures with varying distance were milled as an example shown in Fig. 5.30(a). The picture of Fig. 5.30(a) is an SEM image of pair-slit array of 4 by 4 with a lateral distance of $20.1 \mu\text{m}$. After planarization and deposition of the sacrificial layer, grating was going to be milled on top of it with distance of $20 \mu\text{m}$. The final fabricated structure for imaging with a conventional microscope is plotted in Fig. 5.30(b) as well. The marks were re-milled each time after the deposition of metal films.

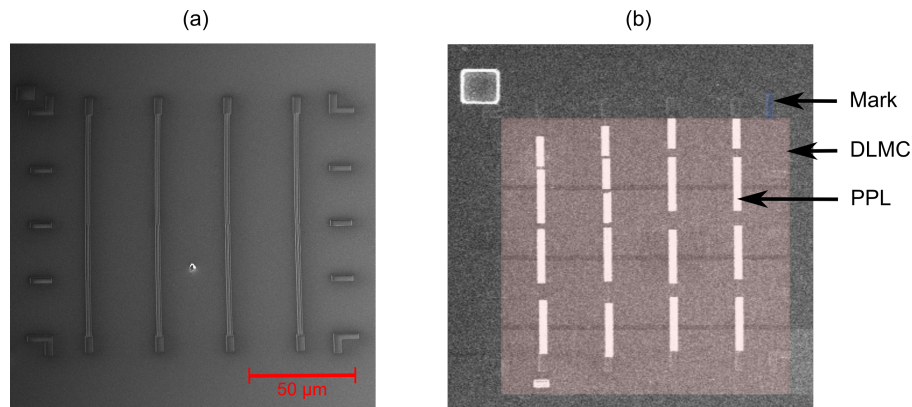


Figure 5.30 (a) Slits array with alignment marks; (b) Top view of the entire structure for optical characterization.

6 Experimental verification of the cascaded superlens

In the preparations for fabrication, each sub-structure of the cascaded superlens has been optimized and characterized separately. Afterwards, the cascaded plasmonic superlens can be formed by stacking the two plasmonic elements together for a systematic study of its imaging properties. In this section, the obtained images with superresolution under an in-hose-built microscope will be illustrated.

6.1 Image of pair-slits under conventional microscope

Before we stacked the cascaded superlens on pair-slits which is used as a standard object in the experiment, field distributions of the objects alone were measured first as a preliminary test. The slit width in the pair-slit object is 100, 200, 300 and 400 nm separately from left to right and the object size is double of the corresponding width as the SEM images shown in Fig. 6.1(a3-d3), which were milled into a 100 nm thick Cr layer on the same substrate.

The field distribution in the far field calculated with Microsim assuming that the incident wave consists of E_x component is shown in Fig. 6.1(a1-d1). Fig. 6.1(a2-d2) shows the measured transmitted intensities of pair-slit with parameters corresponding to the simulations. The field distribution was measured by the photon detector first under the aerial scanning imaging microscope at the wavelength of 640 nm, and the incident wave illuminates the object from the bottom side. The measured step is 40 nm \times 50 nm, vertical and lateral in the xz-plane.

For the object with a slit width of 100 nm and a size of 200 nm, the measured field is strongly noisy due to the weak transmitted light behind the slits and the pinhole in front of the detector for size limitation. However, it can still be seen that the measured field degenerates into a single slit and agrees with the simulation. When the slit width is increased to 300 nm and 400 nm, at the same time the object size is increased to 600 nm and 800 nm, respectively (Fig. 6.1 (c3) and (d3)), the measured intensity is high enough to be compared with the numerical predicted

field distributions, and they agree very well with each other. The asymmetric field distribution in Fig. 6.1(d2) may be induced by a slight width difference of the two slits introduced during fabrication. The comparison results show a good agreement between the simulation and measurement.

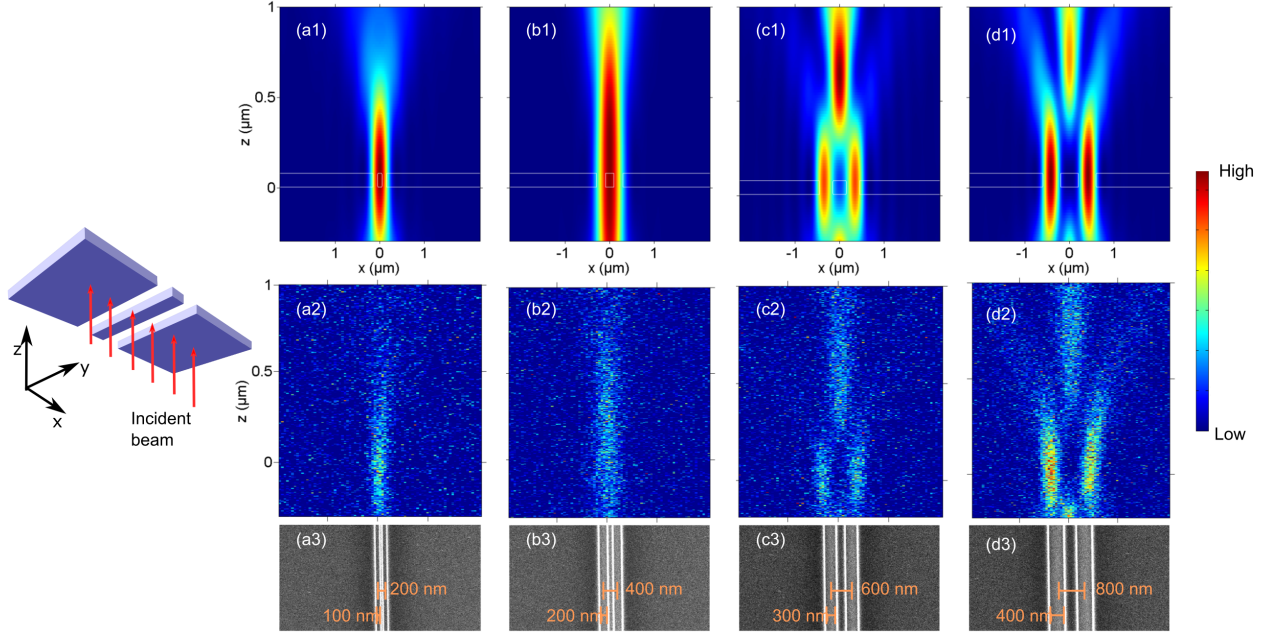


Figure 6.1 Transmitted field distribution of pair-slits: (a-d) Results of pair-slits with different width (100, 200, 300 and 400 nm separately) and object size (200, 400, 600 and 800 nm separately); (1) Simulation results; (2) Measured results with the photon detector; (3) SEM images of the pair-slits with different sizes.

The obtained results of the pair-slit with slit width of 100 nm is noisy. Additional direct microscope images of the pair-slit with width of 100 nm and different object sizes ranging from 200 nm to 400 nm are obtained by a CCD camera as shown in Fig. 6.2. The normalized intensities of the pair-slits are further plotted in Fig. 6.2(d). It can be seen that the obtained image is not resolvable until the object size is increased to 400 nm when the slit width is 100 nm.

According to the measured results, we can see that the image of the pair-slits with size of 400 nm and width of 200 nm is unresolvable. However, the one with the same size but slit width of 100 nm is resolved. This is because the slit in the object is not an ideal point source, but with a size and the size is relative large compared to the object size. In this case, the Abbe diffraction cannot be applied anymore. Considering the intensity of the transmitted light, we will adopt the slit with width of 100 nm, which is unresolvable until the object size is increased to 400 nm, to test the lateral resolution of the cascaded superlens.

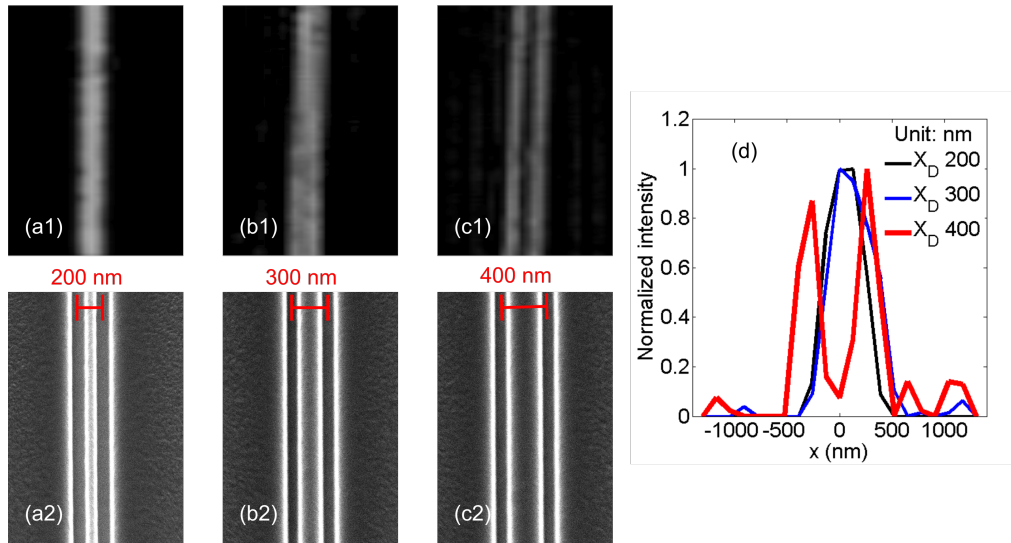


Figure 6.2 Images of pair-slits with slit width of 100 nm with object size of (a) 200 nm; (b) 300 nm and (c) 400 nm: (1) CCD images; (2) SEM images. (d) Normalized intensities from the CCD images.

6.2 Preliminary imaging test of the cascaded superlens

Before examining the lateral resolution of the cascaded superlens, a preliminary test was carried out first with a relative large object: a pair-slit with slit width of 400 nm and object size of 800 nm is used first as an object for its higher transmitted intensity, with which more light can be transmitted through the structure and the superlens can be characterized more profoundly. An SEM cross-sectional image of a fabricated result with a fabricated object is shown in Fig. 6.3.

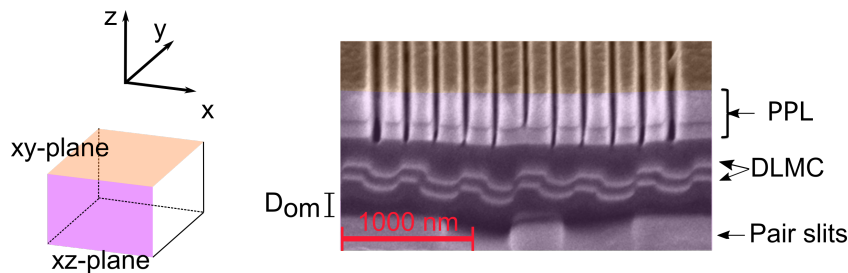


Figure 6.3 SEM cross-sectional image of a fabricated cascaded superlens stacked on top of an object with slit width of 400 nm and object size of 800 nm.

Sequential layers constituting the cascaded superlens and the pair-slit object can be seen in the xz -plane. Due to the larger slit width and smaller D_{OM} , which is 30 nm in this case, the whole lens sink slightly towards the substrate. Nevertheless, it does not influence the field distribution or the lens function as the image illustrated in Fig. 6.4.

A simulation with structural parameters measured from cross section image in Fig. 6.3 is plotted in Fig. 6.5. To further compare the measurement and simulation results, we take the intensity

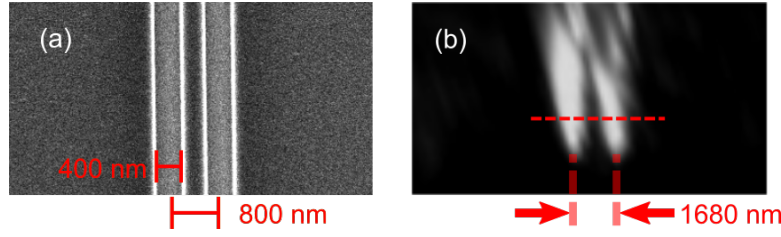


Figure 6.4 (a) Pair-slits used for preliminary test; (b) Image of (a) obtained in far-field with assist of cascaded superlens.

along the red lines in Fig. 6.4(b) and 6.5(a) separately and plot them in Fig. 6.5(b). The measured fields in the xy -plane shown in Fig. 6.4(b) was taken at $z = 1.5 \mu\text{m}$ along the red dashed line in Fig. 6.5(a). A good agreement between the two can be obtained.

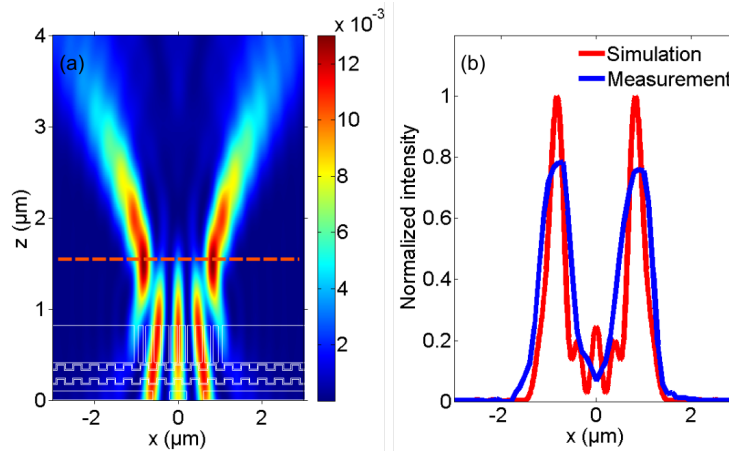


Figure 6.5 (a) Results calculated according to the parameters measured in Fig. 6.3; (b) Comparison of field distribution between simulation and measurement (position of dashed line shown in simulation and measurement separately)

Images at other height ($z = 1$ and $0.5 \mu\text{m}$ separately) are also obtained and are shown in Fig. 6.6. The preliminary test shows a good agreement of the field distribution along xy -plane between simulation and measurement at different height, which demonstrates that the cascaded superlens can be well fabricated to realize the function predicted by the numerical simulation, although complex plasmonic structures are involved.

We notice, however, that the two peaks of the measured image in Fig. 6.4(b) are not parallel with broadening at the upper position in the CCD image. This is induced by a small alignment angle between the object and the DLMC structure introduced during the fabrication. The effect of alignment problem is more obvious when measuring the field distribution of pair-slits stacking with the DLMC structure as an example shown in the Fig. 6.7. The pair-slit ($w = 100 \text{ nm}$ and $X_D = 200 \text{ nm}$) with a position shift of 100 nm to the right relative to the DLMC structure. The influence to the field distribution is obvious with and without position shift

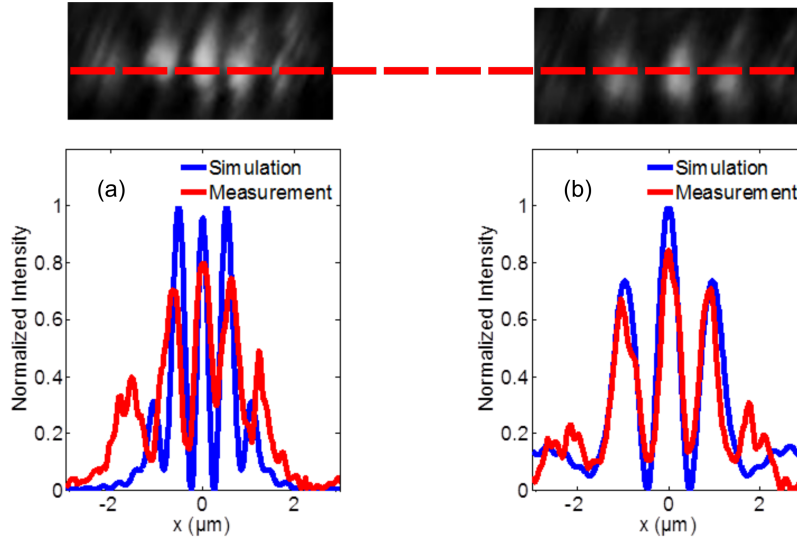


Figure 6.6 CCD images at other height: (a) $z = 1 \mu m$; (b) $z = -0.5 \mu m$. The top row shows the images measured at different z -positions using a CCD camera and the bottom row shows the field plots along the red dashed lines marked in the top row.

considering the simulation results of Fig. 6.7(b) and (c). The conclusion was also validated with experiment: the DLMC structure was stacked on the pair-slit with the same position shift and the image was captured by CCD camera as shown in Fig. 6.7(d) and by the photon detector as shown in Fig. 6.7(e). The CCD image was captured at the z -position along the white dashed line in Fig. 6.7(b) or (e) and a comparison between the simulation and measurement is plotted in (f). The meander structure affects the intensity distribution due to its similar period to the object size, which is a limitation to the cascaded structure. The problem will be discussed and solved later in the following chapter.

Based on the small intensities collected by photon detector shown in Fig. 6.7(c), in the following experiment, only CCD images will be taken and used due to the high SNR (signal to noise ratio) of the system.

6.3 Lateral resolution of the fabricated cascaded superlens

After validating the imaging capability of the cascaded superlens with an object that has a relative larger size and higher transmission, we went further to verify the resolution limit of the superlens discussed in Section 4.2.2. We reduced the size of the object to a slit width of 100 nm and size of 180 nm. A cross section image of the fabricated lens is shown in Fig. 6.8. From the image, we can see that a nearly perfect alignment between the lens and the object has been achieved and the lens itself is in good shape of planar without sinking into the object.

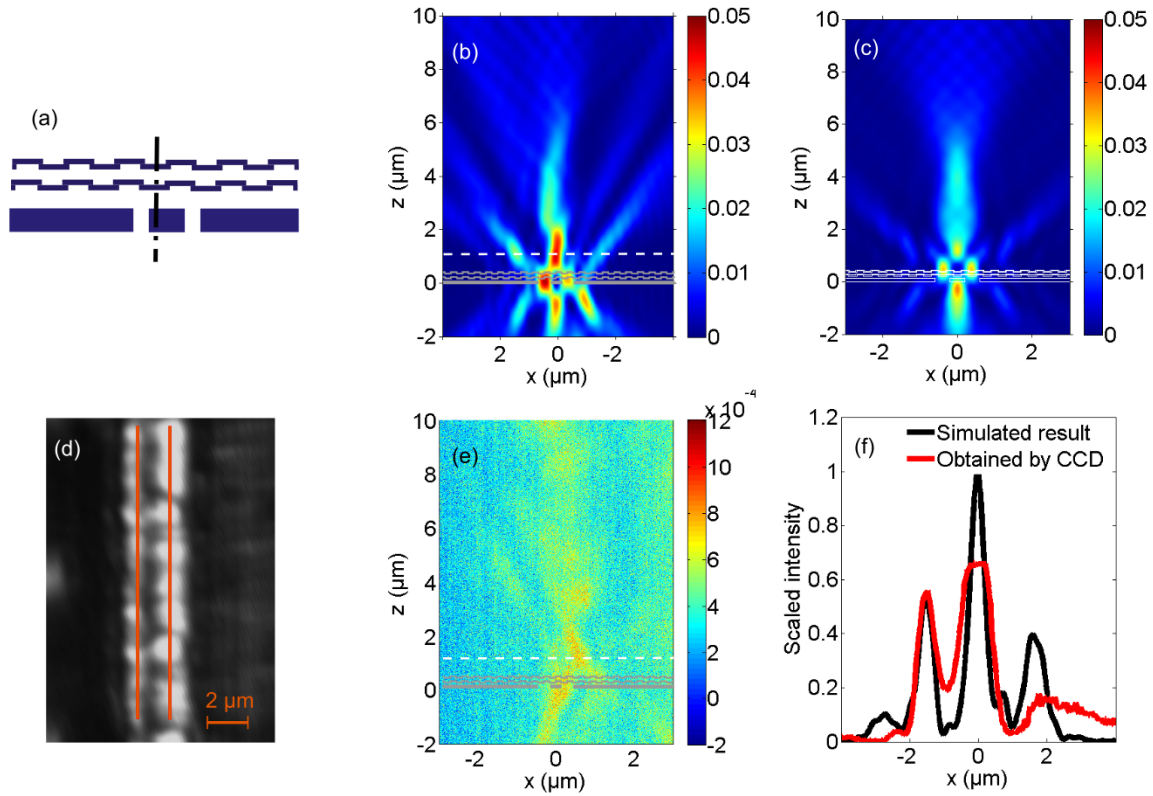


Figure 6.7 Intensity distribution of pair-slit stacking with DLMC structure along xz - plane: (a) Schematic for the disalignment between pair-slit and DLMC; (b) Simulation of the transmitted intensity distribution along xz -plane of the pair-slit stacking with the DLMC structure when the position of pair-slits is shifted 100 nm to the right; (c) Simulation when there is no position shift; (d) Image obtained by CCD camera at position along dashed line in (b); (e) Measured intensity distribution when there is a position shift between the pair-slit and the DLMC structure; (f) Comparison between simulation and measurement along dashed line in (b) and (e).

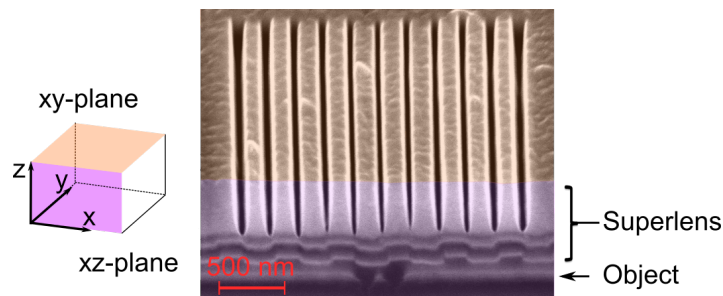


Figure 6.8 Cross section of the superlens fabricated on the object with width of 100 nm and object size of 180 nm.

An SEM image of the object with subwavelength feature is shown in Fig. 6.9(a). The object is measured under the microscope directly first and the obtained image is shown in Fig. 6.9(b). For this object, the obtained image is degenerated to a single slit and definitely unresolvable under the microscope. In contrast, a resolvable image with magnification in the xy -plane can indeed be obtained with assist of the cascaded superlens as shown in Fig. 6.9(c). The distance between the peak intensities (image size) is about 470 nm. In the measurement, the magnification factor of the conventional microscope is taken into consideration. The sizes shown in the figures of the measured results are the ones imaged behind the cascaded superlens, not the real sizes measured with the CCD camera. Additionally, the imperfection of the fabricated slit is also clearly imaged by the lens, which can be attributed to the defects on the object slits and the roughness along the grating and the deposited thin films for meander structure.

Take the intensity along red dashed line in Fig. 6.9(c) and compare it with the simulation results calculated in Fig. 4.8, Section 4.2.2, we see that a good agreement is also achieved as the curves shown in Fig. 6.9(d). In the image, the image width of the two slits is different from each other due to a slight misalignment between the cascaded superlenses and the pair-slit object as predict by the simulation shown in Section 4.1.2. This problem will be solved with a modification of the DLMC structure and the details will be presented in the following chapter.

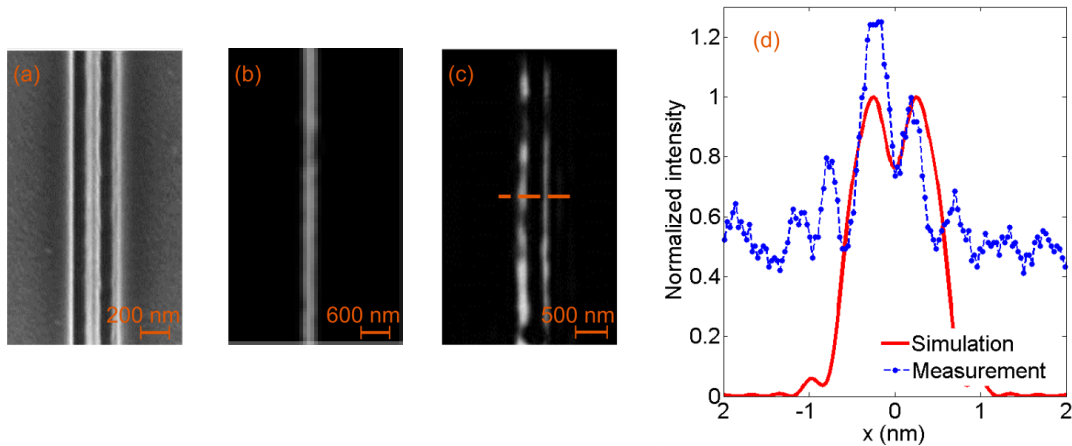


Figure 6.9 (a) SEM image of the object with width of 100 nm and object size of 180 nm from center to center; (b) Image of the object under a conventional microscopy; (c) Image of the object obtained in far-field with assist of the cascaded superlens; (d) Comparison between simulation and measurement: simulation obtained from the figure shown in simulation chapter and measurement data draw along dashed line in CCD image.

Shifting the piezo stage in z -direction to take CCD pictures at different height (with step of 100 nm), we can obtain enough information to draw a field distribution along the xz -plane as shown in Fig. 6.10, which is taken parallel to the red dashed line in Fig. 6.9(c). In the observation

range, the measured data follow approximately the numerical data. The simulation shown in Fig. 6.10(c) is calculated with optimized parameter but a shift of 20 nm to the left of the DLMC structure, which further explains the width difference in the obtained image in Fig. 6.9. In the image of the intensity distribution along the xz -plane, we can see clearly the image position and the diffraction pattern with higher intensity. The distribution of the obtained field is not exactly the same as the simulation prediction. This may be caused by the shape of the meander grating, which is not a perfect rectangular one. However, the results are good enough to demonstrate that the cascaded structure is a lens, namely a cascaded superlens.

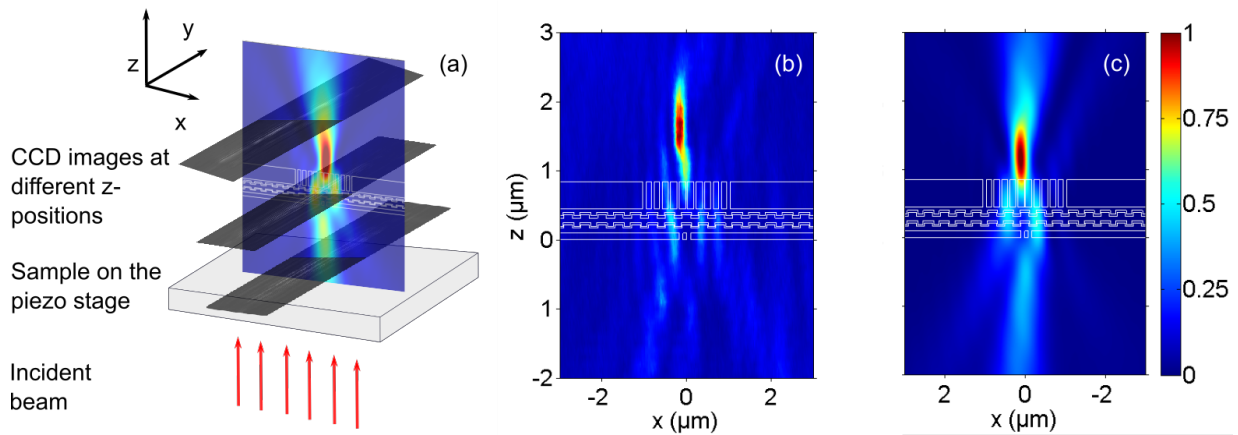


Figure 6.10 Intensity distribution along xz -plane: (a) Schematic of obtaining intensity distribution along xz -plane; (b) Measurement results; (c) Simulation with optimized parameter but a 20 nm position shift of the object.

As to the discontinuity of the image, one of the reasons is the rough sidewalls of the slits in PPL or the grating prepared for meander structure. However, these defects can be avoided by altering the fabrication material or methods.

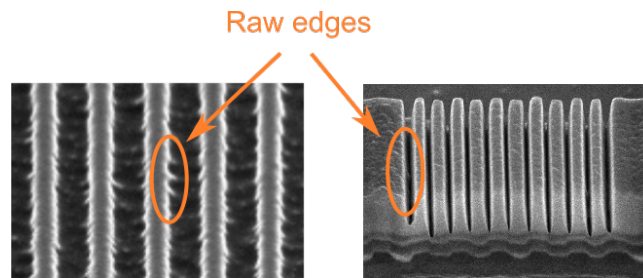


Figure 6.11 Gratings with raw edges.

A pair-slit with angle was further fabricated to evaluate the lateral resolution in experiment. The angle between the two slits is 3° and length is $12 \mu\text{m}$ with object size from 0 up to 550 nm from center to center as shown in the Fig. 6.12(a). The obtained CCD image is replotted to extract the image size at different position and then compared with simulation. The two also reach a good agreement except for some break-ups in the image. One reason for the break-ups

lies in an intrinsic problem of the superlens which is already shown in the simulation results, i.e. Fig. 4.8: the transmitted intensity is different from each other when varying the size of the object.

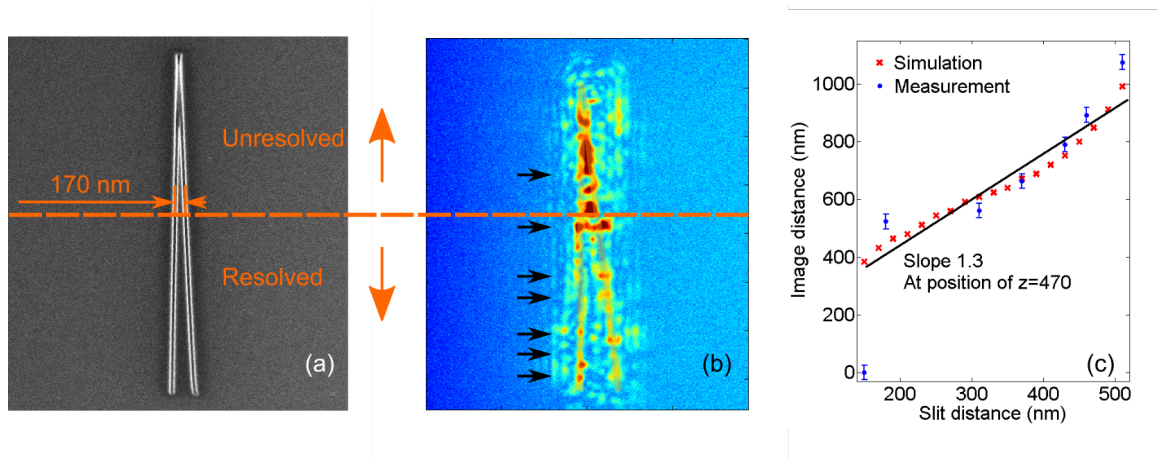


Figure 6.12 (a) Pair-slits with an angle of 3° : width of 100 nm and length of $12 \mu\text{m}$; (b) image of the object shown in (a) with cascaded superlens; (c) comparison between simulation and measurement (at the positions of the black arrows).

In summary, the cascaded superlens has been successfully fabricated. By stacking the superlens on slits, the subwavelength imaging capability of the cascaded superlens has been experimentally demonstrated. The concept to design a superlens with a cascade structure to realize near-field wave transformation and magnification separately is feasible and the simulation results perfectly predict the imaging behavior of the cascaded superlens.

6.4 Lessons learned

The experimental results are in line with the simulations thanks to the precise control of the fabrication procedure, which prove the feasibility for the fabrication of the designed structure and the obtained images show that the transmitted field intensities are high enough to be detected by a CCD camera though the metallic lens has a strong attenuation to the incident light.

For a thin metallic film, the evaporation quality will influence the optical response of the structure. In order to obtain a continuous and smooth film of silver layer with evaporator, adding a wetting layer (Cr or Ge) is an impactful way, which can largely decrease the cracks observed under SEM. The optical property of the film with wetting layer (about 1 nm) is nearly identical with an ideal film (compared with simulation).

Good conformity of the top layer with the bottom layer was obtained inside the double layer meander structure by evaporating the top layer directly after the first one when the gap between the two layers is relative small, which is better than fabricating the structure twice and can efficiently avoid the alignment problem inside the double layer meander structure.

The milling results vary with the used time of the ion beam, it is necessary to optimize the fabrication parameter each time to ensure the obtained structure with desired size.

For the spatial layer, it is hard to directly obtain a planarized film with desired thickness on top of the object. Our solution is to spin-coat a thicker layer (about 700 nm) and then to reduce the thickness via plasma etching.

7 Modification of the cascaded superlens

Previously we have numerically and experimentally demonstrated subwavelength imaging capability of a cascaded superlens. For the cascaded superlens with DLMC structure, the relative position between the object and the DLMC structure influences the image field distribution heavily. In this chapter, a plasmonic cavity lens for near-field coupling is used instead to diminish the problem.

7.1 Introduction to the design of a modified cascaded superlens

Fig. 7.1 shows a modified design of the cascaded superlens. In the design, the DLMC structure is replaced by a simple plasmonic cavity lens (PCL) [90, 139, 140]. To avoid the high loss of as with HMMs [3], the PCL structure in this design still consists of only two layers. To tune the operation wavelength to mid visible wavelength range, the two flat metallic layers are integrated with distributed Bragg reflectors (DBRs), which will be discussed in detail in subsection 7.2.1.

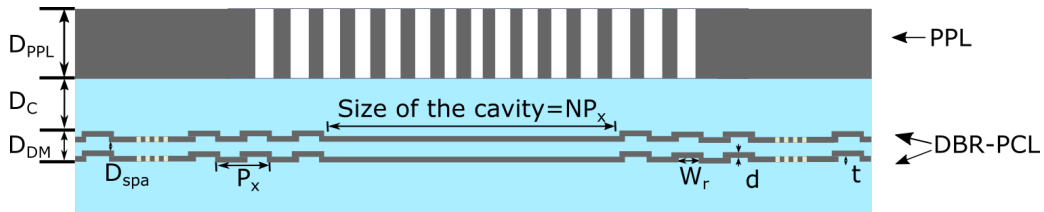


Figure 7.1 Schematic of the modified cascaded superlens.

The function of the DBR-PCL structure is the same as that of the DLMC structure, to couple and amplify evanescent waves emanating from subwavelength objects. The PPL structure has the same function and parameters as describe in subsection 3.3.1.

7.2 Simulation results of the modified cascaded superlens

Simulation results will be illustrated in this section to theoretically demonstrate that the problem can be overcome with the plasmonic cavity lens. In the meanwhile, physical explanations to the modified structures are given as well.

7.2.1 Near-field transmission dispersion of the DBR-PCL structure

To tune the performance wavelength to visible and to enhance the near field transmission, distributed Bragg reflectors (DBR) are integrated to the plasmonic cavity lens (PCL) around the lens center, forming additional lateral cavities for surface waves.

According to the continuity of the transverse wave vector at the interface of two materials, propagation distance of surface wave can be calculated according to equations in Subsection 3.2.1. The surface plasmon along surface between metal and dielectric decreases with $\exp(-2xk''_{spp})$. Taking the distance when its intensity decreases to $1/e$ of the original as the propagating distance, we have:

$$L_{spp} = \frac{1}{2k''_{spp}}. \quad (7.1)$$

The equation can be rewritten as according to Eq. 3.30:

$$L_{spp} = \frac{(\varepsilon'_d)^2}{k_0 \varepsilon''_m} \left(\frac{\varepsilon'_m \varepsilon_d}{\varepsilon'_m + \varepsilon_d} \right)^{-3/2} \quad (7.2)$$

Take silver used in the structure as an example, according to Joannopoulos-Christy [122]: $\varepsilon_m = 0.0555 + 4.3372i$ at 468 THz, $\varepsilon_d = 1.41$, then $L_{spp} = 300 \mu m$.

Thanks to the long propagation distance of surface waves, plasmon can still be excited and reflected with the DBR-PCL structure (schematic shown in Fig. 7.2). By optimizing the parameters, we can obtain a DBR-PCL structure with a near-field dispersion, which covers a wide range of high transverse wave vectors and is used to couple the evanescent waves.

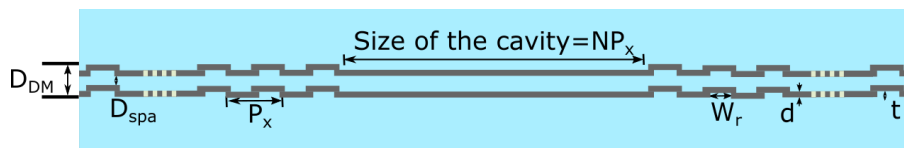


Figure 7.2 Schematic of the DBR-PCL structure.

Here we further calculate the image shift of a single slit ($w = 100$ nm) behind the DLMC structure and the DBR-PCL structure separately to illustrate the benefits of introducing a flat cavity. The curves are plotted in Fig. 7.3. The simulations were performed for the near field and the image positions were taken 2000 nm behind the meander structure. In the figure, the green curve is used to illustrate the position of the DLMC structure in comparison with that of the slit. An abnormal image position clearly shows that the field distribution is influenced by the meander (at position of 0, 50 and 300 nm). However, if the DLMC structure is replaced with the modified one, the position problem is diminished as shown in the figure.

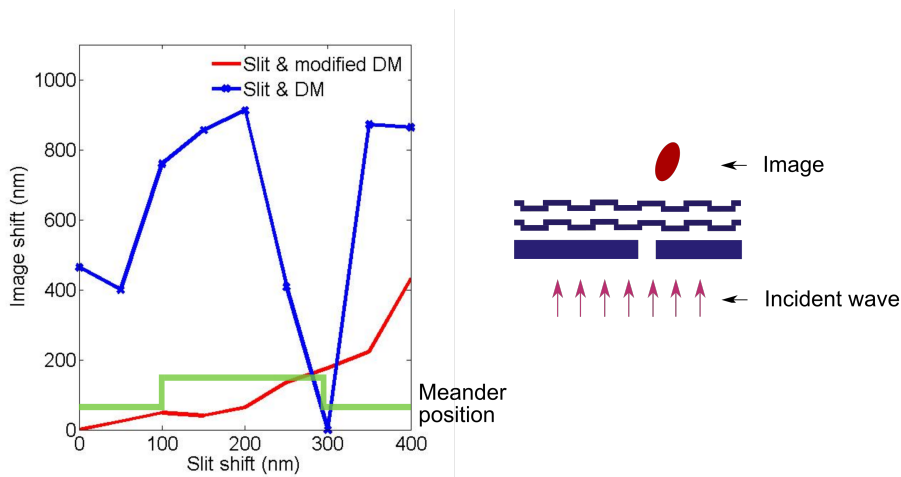


Figure 7.3 Position shift of a single slit coupled with the DLMC structure.

To test the influence of introducing the flat cavity to the DLMC structure, a series of simulations of the dispersion with different size of flat cavity were done and the results are shown in Fig. 7.4. For a clear view of the changes in dispersion distribution and direct comparisons with the previous published paper by our group [35, 116–118], the dispersions are calculated by burying the DBR-PCL in the air with same parameters used in Chapter 3 but with different length of the flat cavity.

Compared with the dispersion of the DLMC structure, a DBR-PCL structure will introduce a lateral Fabry–Pérot, which helps to extend the passband between $k_0 < k_x < 1.5k_0$ (which is the range utilized in the cascaded superlens to obtain subwavelength imaging) to a larger frequency range. The extension enables the superlens to be used under other wavelength or even white light. Fig. 7.5 shows optical responses in larger transverse wave vector range (k_x) from both the DLMC structure and the planar FP cavity (mode along the white dashed line).

For the fact that the experimental verification will be conducted at the frequency of 468 THz, the dispersions as a function of the transverse wave vector with different sizes of the flat cavity are further compared and illustrated in the Fig. 7.5(b). At 468 THz (640 nm), the DBR-PCL structure with a cavity size of $8P_x$ has a relative broader response to waves around $k_x \approx$

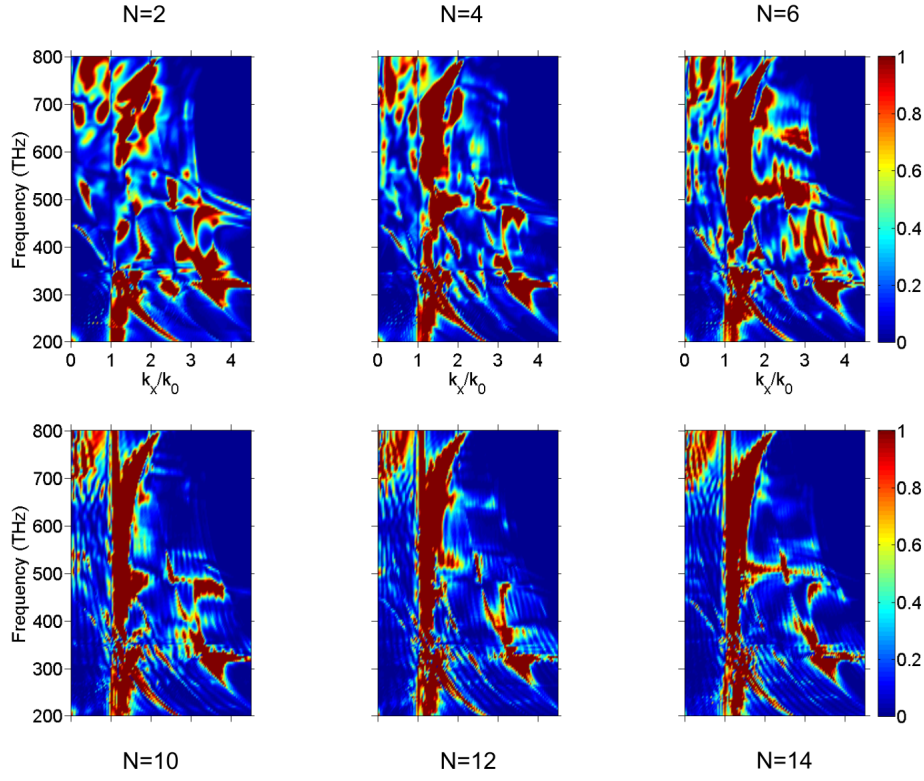


Figure 7.4 Near-field transmission dispersion with different size of flat cavity.

$[1.2k_0, 1.8k_0]$ and is used for our lens design. Size of the inserted flat cavity is shorter than the propagating length of surface wave, which enables the DBR-PCL structure to transfer the evanescent wave or information carried by high k_x component.

In the fabrication, the DLMC structure is buried in SOG instead of air. We change the material and the parameters to optimize the dispersion at the frequency of 468 THz. The range of the parameters are determined considering fabrication possibility, especially for t , which may introduce cracks when t is large and the film is thin as we have discussed in Chapter 5. The tested parameters are illustrated in Table 7.1 for parameter optimization.

Table 7.1 Variation parameters used for simulating the dispersion property of DBR-PCL to optimize the parameters.

| Unit: nm | Start | Step | End | Optimized |
|------------------|-------|------|-----|-----------|
| D_{spa} | 70 | 10 | 120 | 90 |
| d | 10 | 5 | 30 | 25 |
| t | 40 | 10 | 100 | 90 |
| W_r | 160 | 20 | 240 | 180 |

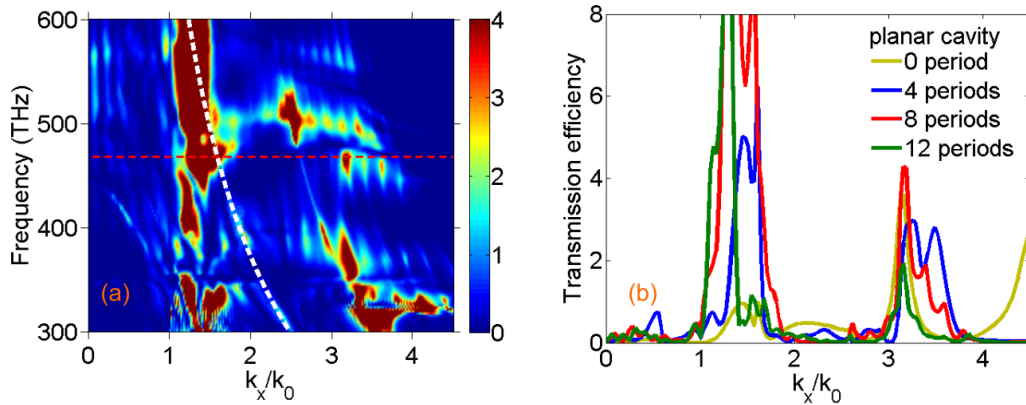


Figure 7.5 (a) Near-field transmission dispersion of DBR-PCL structure calculated as function of frequency and k_x/k_0 with $N = 8$ for the size of the cavity. White dashed lines: one of the lateral Fabry-Pérot modes induced by the planar cavity; (b) Dispersion of the DBR-PCL structure with different size of planar cavity at $f = 468$ THz ($N = 0, 4, 8, 12$).

To illustrate the influence of each parameter to the near-field transmitted spectrum, several results are plotted in Fig. 7.6. Fig. 7.6(a) is the dispersion with different size of the flat cavity. Different from the results for the structure buried in air, the resonances introduced by the flat cavity is more obvious and the width of the peaks in the curve is larger and the number of the FP resonant peaks increases with the length of the cavity. For the DBR-PCL structure, there are some high transmission peaks around $k_x = 1.2 - 2k_0$ as shown in Fig. 7.6. These resonances may not be favorable for near-field imaging due to the strong interference of the surface waves [90]. The dispersion with less resonant peaks is desired, and under this condition the simulation results of the one with $N = 2$ is better. However, considering the field of view and the width of the pass band, $N = 8$ is used for the second design. The same principle is used to determine the parameters of D_{spa} and the curves are plotted separately in Fig. 7.6(c). The grating height with $t = 90$ nm instead of 70 nm is chosen, due to the fact that the pass band of the former is broader than the later considering the propagation waves with $k_x \leq k_0$. The principle is used to determine the film thickness d as well. The optimized parameters for the DBR-PCL structure within the range shown in Table 7.1 are shown in the figure caption of Fig. 7.6.

The modified structure can not only decrease the effects of grating to the image but also extend its application frequencies, for the reason that the inserted flat cavity generates more surface modes. Take the dispersion distribution of the DBR-PCL buried in the SOG with the optimized parameters as an example (shown in Fig. 7.7), the modified structure has a wider range of incident wavelength especially for the range from 350 THz to 700 THz, inside which the amplitude of high spatial frequency can be amplified. The dispersion illustrates a potential application to use the structure under white light incident wave.

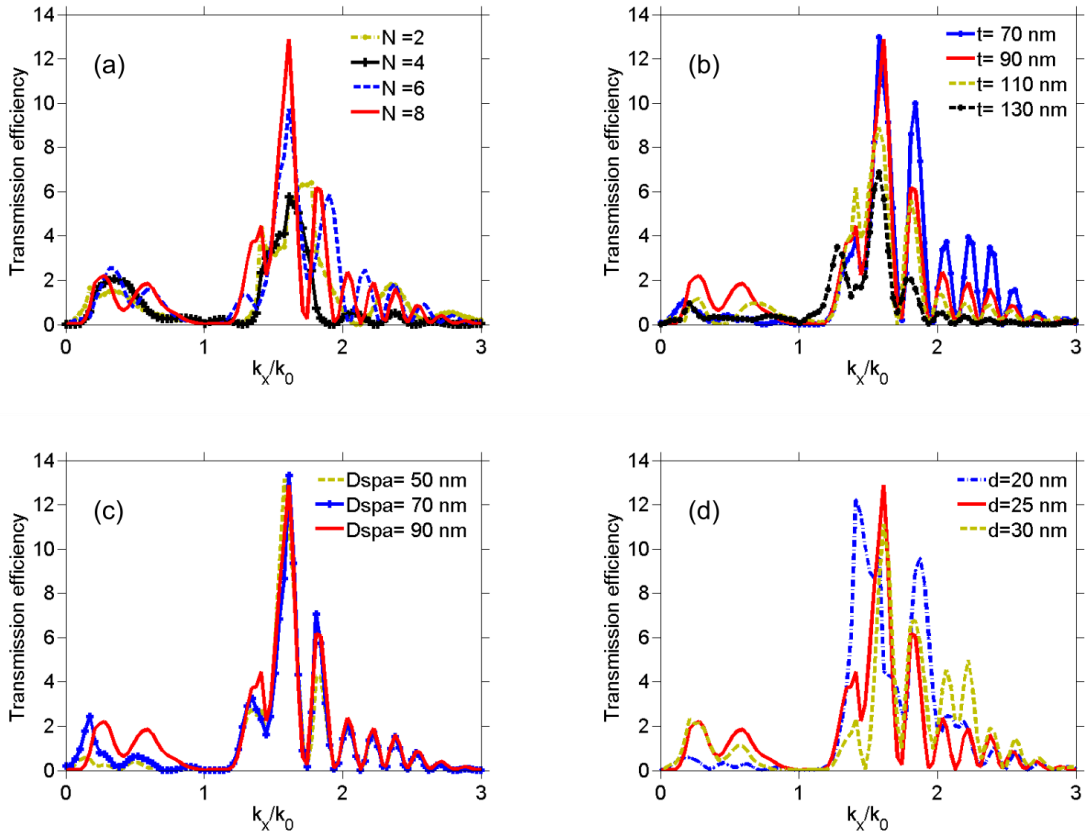


Figure 7.6 Near-field transmission dispersion of the DBR-PCL structure with varied parameters: $P_x = 400$, $D_{spa} = 90$, $d = 25$, $W_r = 180$ and $t = 90$ (unit: nm), $N = 8$ when not specially mentioned.

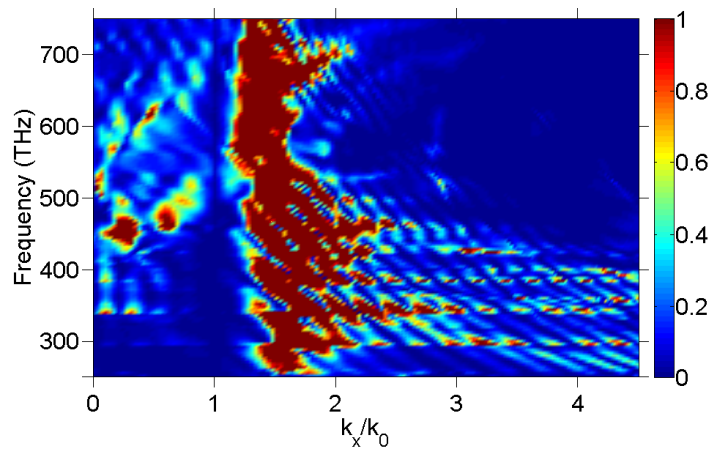


Figure 7.7 Near-field transmission dispersion of the DBR-PCL structure with an 8 period flat cavity buried in SOG with parameters: $P_x = 400$, $D_{spa} = 90$, $d = 25$, $W_r = 180$ and $t = 90$ (unit: nm).

7.2.2 Near-field transmission dispersion of the modified cascaded superlens

Transmitted angular spectra at 468 THz of the modified superlens were calculated further to test how the inserted flat cavity works to decrease the image variation in case of alignment problem between the DBR-PCL and the PPL structures inside the superlens. The simulations are performed under the incident wave at the frequency of 468 THz and are shown in Fig. 7.8. When there is a slight lateral shift between the two elements, such as 20 nm, which occurs very possibly in the fabrication, the transmission spectrum is further randomized as shown by the black curve in Fig. 7.8. The conclusion offers feasibility for the fabrication of superlens relating to the tolerance of alignment between the PPL structure and the DBR-PCL structure.

As we can see in Fig. 7.7 and 7.8, that the DBR-PCL structure alone can still generate some resonance peaks, however, when it is combined with the PPL structure, the transmission peaks from both elements are suppressed greatly and the resonances in the lateral cavities are randomized.

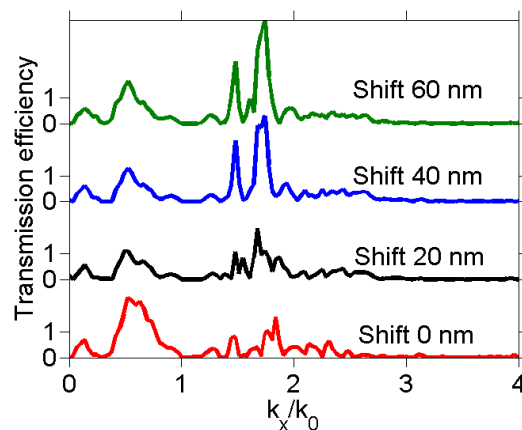


Figure 7.8 Near-field transmission dispersion at 486 THz with relative position shift between the PPL structure and the DBR-PCL structure when D_c is 50 nm.

7.2.3 Numerical study of the modified cascaded superlens

In this subsection, the imaging behavior of the modified cascaded system will be simulated. Here we use a single slit in a chromium layer as an object to perform the simulation as shown by the schematic in Fig. 7.9. By changing the position of the slit ($X_d/2$), image in the far field is supposed to shift as well.

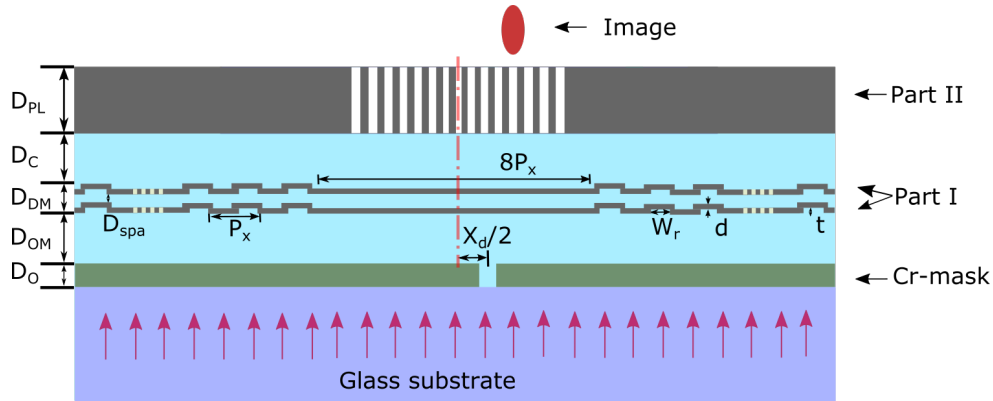


Figure 7.9 Schematic of the superlens with planar and vertical cavities; Slit position: $X_d/2$.

The simulation results calculated with Microsim are plotted in Fig. 7.10. Considering the interaction between the PPL and the DBR-PCL structures and the fabrication possibility, parameters are optimized further as shown in the figure caption. Fig. 7.10(a) is the field distribution when shifting the single-slit 100 nm to the right ($X_d/2 = 100$ nm) and (b) is the image position as a function of the slit position. A nearly linear relationship between the two can be obtained from the simulation results.

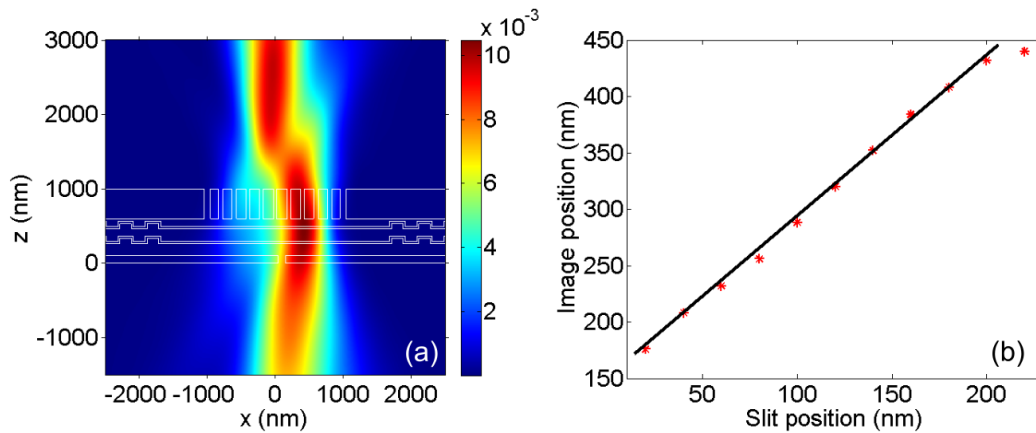


Figure 7.10 Simulation results using a single-slit as an object: (a) Image distribution of a single slit with position shift of 100 nm to the right; (b) Image shift as a function of slit position. Simulation parameters: $D_{PL} = 400$, $D_C = 40$, $D_{DM} = 320$, $D_{OM} = 160$, $D_O = 100$, $D_{spa} = 100$, $P_x = 400$, $W_r = P_x/2 - d$, $d = 30$, $t = 70$ (unit: nm) and $N = 8$.

Furthermore, another series of simulations using pair-slit as an object are performed to evaluate the imaging behavior of the modified cascaded system as a predication to the experimental verification. Lateral resolution and influence of alignment of the modified cascaded structure is then checked according to the field distribution in the far field.

The simulation results are shown in Fig. 7.11. Fig. 7.11(a) is the far-field transmitted intensity distribution of cascaded superlens coupled with the pair-slit object with a size of 200 nm, from which clear image of the pair-slits can be seen. Take $z = 920$ nm as the image plane, the variation between slits and images is obtained and shown in Fig. 7.11(b). The intensity distribution along x-axis at $z = 920$ nm is further plotted in Fig. 7.11(c), which helps to determine the lateral resolution of the modified cascaded superlens. Subwavelength imaging with magnification is numerically demonstrated with the modified cascaded superlens. The normalized image profile of the pair-slits with size of 200 nm results in an image contrast of 0.89. Although this value is larger than the Rayleigh criterion, it is sufficient for our CCD camera and we take this value as the resolving power of our modified cascaded superlens.

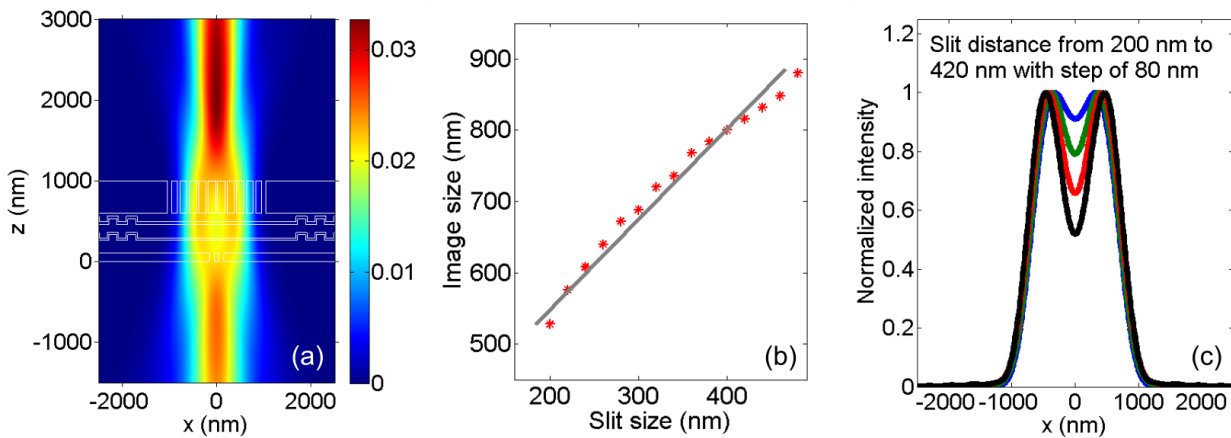


Figure 7.11 Simulation results of image distribution with $D_{DM}=150$ nm: (a) Intensity distribution of pair-slit integrated with superlens; (b) Image size as a function of object size at $z = 920$ nm; (c) Intensity distribution of different slits along plane of $z = 920$ nm.

Field distribution of the pair object with same size ($w = 100$ nm and $X_d = 200$ nm) of Fig. 7.11(a) is also calculated when there is a position shift of the sub-structure in the modified cascaded superlens. As illustrated in the former section, the image distribution of the cascaded superlens is more sensitive to the position of the meander structure. In this chapter the DBR-PCL is used to illustrate that the influence of the relative position shift has been diminished and the results are shown in Fig. 7.12. The change of the image is not obvious even the position shift of the DBR-PCL structure is increased to 550 nm, which can be efficiently avoided during fabrication. The calculation results show that it will be easier to fabricate the modified cascaded superlens.

Tolerance for the fabrication are further tested by calculating field distribution with varied parameters. Take the intensity distribution of the pair-slit with size of 200 nm as an example, image distributions are plotted in Fig. 7.13. Structural parameters of the modified superlens are

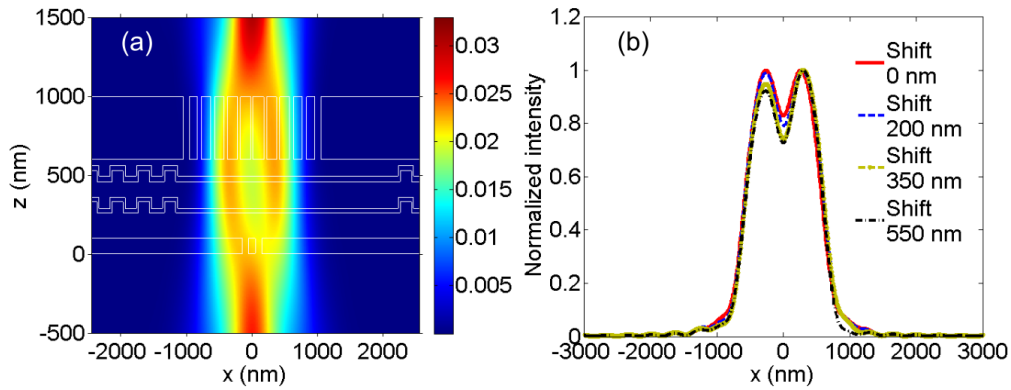


Figure 7.12 Image of pair-slit with width of 100 nm and distance of 200 nm with position of the DBR-PCL structure: (a) Transmission distribution of the pair-slit when the position of the DBR-PCL is shifted 550 nm to the left; (b) The field distribution at the image plane.

same as those shown in Fig. 7.10 if not mentioned in the figure caption. We can obtain a same conclusion as that of the cascaded superlens: if the parameters varies about ten percent around the optimized ones, the variation of the image distribution is nearly unchanged considering the size of the image and the field intensity distribution in the xz -plane except for the height of the grating. Due to the introduction of the flat cavity in center position of the meander structure, the image distribution is more sensitive to the grating height especially when we decrease it. For example, when t is decreased to 65 nm, the image of the pair-slit with size of 200 nm is unresolvable as shown in Fig. 7.13(b).

7.3 Fabrication and experimental verification of the modified cascaded superlens

After simulation, the modified cascaded superlens was fabricated to experimentally demonstrate its imaging capability.

7.3.1 Fabrication of the modified meander structure

The milled result of the grating for DBR-PCL is illustrated in Fig. 7.14. The area in the middle is all milled away as a preparation for the flat cavity. By depositing the materials of Ge(1 nm)/Ag(30 nm)/MgF₂(150 nm)/ Ge(1 nm)/ Ag(30 nm) sequentially, we can obtain the DBR-PCL structure.

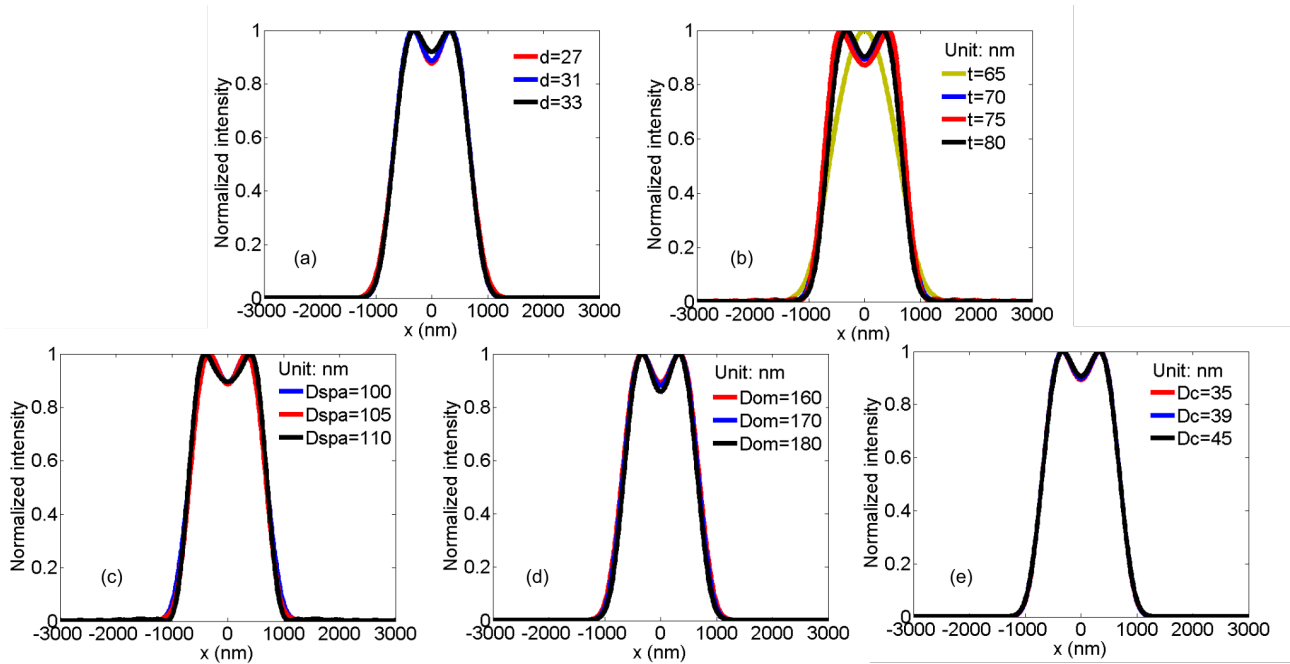


Figure 7.13 Normalized intensity distribution of the modified cascaded superlens when the distance of pair-slit is 200 nm with varied parameters: (a) Thickness of silver film in DLMC; (b) Height of grating; (c) Distance between two meanders; (d) Coupled distance between DLMC and PPL; (e) Distance between pair-slit and cascaded superlens.

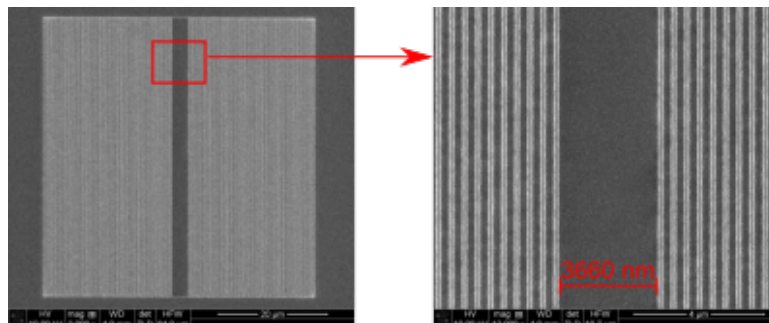


Figure 7.14 SEM images of modified gratings prepared for meander with flat cavity.

The characterization results of the DBR-PCL structure are plotted in Fig. 7.15. The cross section images of the PCL and the DBR structure shown in Fig. 7.15(a) and (b) are taken separately. From the cross section image of the DBR structure, we can see that the fabricated structure is still continuous and symmetric with thin silver film when the grating height is increased to 70 nm. To further characterize the fabrication result, we measured the transmitted spectrum using a FTIR and the result (black curve) is plotted in Fig. 7.15(c). The blue curve is the simulation result. The peak at frequency of 440 THz in the measured curve is not as high as that of the simulation. This may due to the rough surface of the fabricated structure.

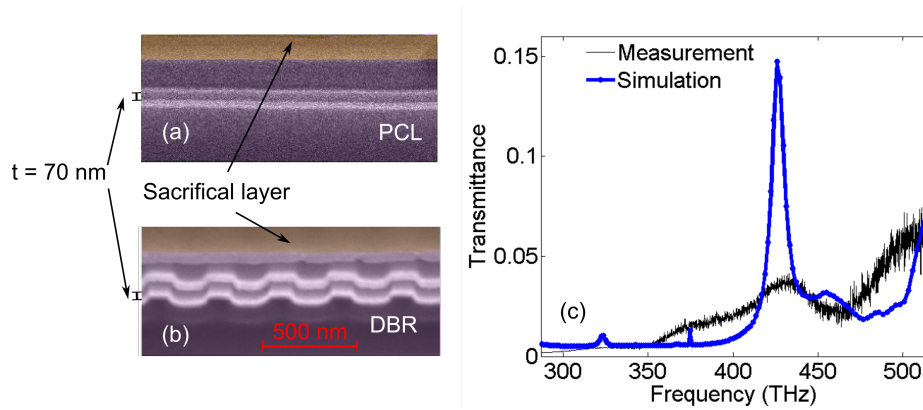


Figure 7.15 (a) SEM cross-section image of the PCL structure; (b) SEM cross-section image of the DBR structure with depth of 70 nm; (c) Comparison between the measured and simulated transmitted spectrum of the DBR-PCL structure.

7.3.2 Imaging tests of the modified cascaded superlens

For the imaging test of the cascaded superlens with the modified design, all the testing procedures and set-ups were the same as those for the original design expect for the DBR-PCL component.

The SEM images of the pair-slit with width of 100 nm and size of 200 nm, grating with flat cavity and the PPL structures are shown in Fig. 7.16(a-c). The grating with flat cavity fabricated on top of the pair-slit object is shown in Fig. 7.16(d1-d3).

In the experiments, the positions of the DBR-PCL structure are laterally shifted compared to that of the pair-slit object to test if the critical alignment problem can be solved with the modified cascaded superlens. By further depositing meander material and stacking PPL structure sequentially, samples for experiment verification were finished. Images obtained by CCD camera in the far field are illustrated in Fig. 7.16(e1-e3) with corresponding position shifts shown in Fig. 7.16(d1-d3). The obtained images of the object are all well resolved.

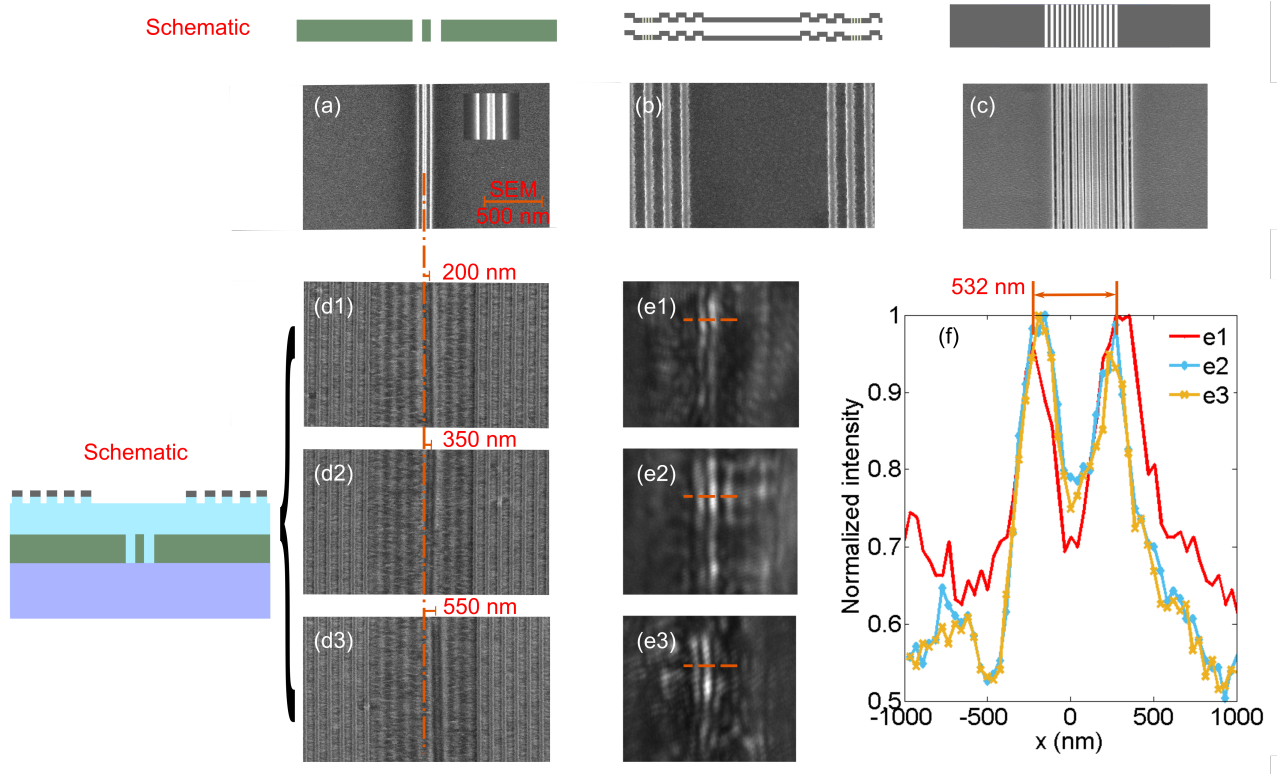


Figure 7.16 (a): Image of pair-slit with width of 100 nm and distance of 200 nm from center to center; (b): Grating prepared for DBR-PCL; (c) SEM image of PPL (modified cascaded structure); (d) Position shift of pair-slit corresponding to meander; (e) Image obtained by CCD camera after stacking the superlenses on pair-slit at corresponding position; (f) Normalized intensity distribution of the obtained image in (e) along dashed line.

The images are not as straight as the objects and there is a noisy background. The problem may come from the rough surface of the flat cavity due to FIB milling. The surface of the fabricated structure is not as smooth as results when the DBR-PCL structure is fabricated separately (figure 7.16(b)). It is worth to mention that when the DBR-PCL structure is reversed along the z-direction, it can still fulfill the function of coupling and support the propagation the evanescent waves. Nevertheless, the structural parameters need to be adjusted slightly. In this case, the flat center does not need to be structured and the surface roughness can be avoided.

The relative intensity distribution along the dashed lines was further plotted to examine the image size as shown in Fig. 7.16(f) with lateral object shifts shown in (d). Thanks to the auto acquisition control of the CCD program, image contrast of the object with 200 nm is much higher than the simulated result. The measured image size is 532 nm in average, which is in accordance with simulation results of 528 nm at z-position of 920 nm. The slight differences of the measured image size may be introduced by fabrication or measurement error. For instance, the imaging depth is limited as can be seen from the calculated image field distribution shown in Fig. 7.11(a). At some position, a slight change of the image position along the z-axis may change the size of the object.

The inhomogeneous linewidth of the image may come from the inhomogeneous slit width milled into the PPL structure. Since the thickness of the PPL slab is 400 nm and the minimum slit width is 34 nm, the milling aspect ratio at the lens center approaches 1/10. A slight milling distortion may induce such a consequence. Nevertheless, this problem can be solved when the PPL is replaced by a large area dielectric metalens [141].

In summary, we have simulated and fabricated the modified cascaded superlens to diminish the alignment problem. The modified superlens will be more practical in application. Moreover, the simulation results were validated by experiments. When 360 nm is taken as the resolution limit of our microscope as obtained from the calculation, in the presence of the superlens the resolution of our microscope has been improved by a factor of 1.8.

8 Summary and outlook

8.1 Summary

In this dissertation, a cascaded superlens for far-field imaging was studied and fabricated based on a concept to realize coupling the evanescent waves and compressing the transverse wave vector separately. In the design, we chose a double layer meander (DLMC) structure and a planar plasmonic lens (PPL) structure as the sub-components. Both numerical simulation and experimental verification were carried out.

With the excited SPPs via periodical corrugated metallic films, the DLMC structure has a near-field dispersion with a broad coverage of transverse wavevectors, which is used to couple evanescent waves. The PPL structure composed of a nanoscale slit array is used to provide phase compensation for image magnification, the wave propagating constant of which is determined by the slit size.

An in-house software package MicroSim based on the RCWA method is used for the simulation. The parameters are optimized considering the fabrication possibilities, with which a lateral resolution of 180 nm at the incident wavelength of 640 nm is numerically achieved.

Nano-fabrication of the superlens with high precision has been accomplished through a step-by-step optimization procedure. Each fabrication step has been characterized and optimized separately. Resolved images have been obtained in the far field when the cascaded superlens is stacked on pair-slit objects fabricated in a chromium layer. A good agreement between the measured transmitted intensity and the simulated results has been obtained. The cascaded superlens with imaging properties as predicted by numerical calculations has been achieved thanks to the well-controlled nano-fabrication procedures. The achieved lateral resolution of the fabricated superlens at the wavelength of 640 nm is 180 nm (nearly one fourth of the incident wavelength), which is same as our simulation prediction. The simulation results show that the transmission efficiency is about 3%, which is acceptable although several layers of metals are used. Furthermore, the image can be directly obtained with a CCD camera. The obtained results pave the way for further nano-fabrication with similar structure or sizes.

Our numerical studies have shown that the PPL structure is not suitable to be used as an imaging device when it is placed in the near field of an object. However, when it is combined with the DLMC structure, near field interactions between the PPL and the DLMC structure suppress the strong grating diffraction of the periodical structures. Nevertheless, the imaging of the cascaded superlens is still sensitive to the relative position between the DLMC structure and the object. This can be attributed to near-field interactions between the object and the corrugated film in the DLMC structure. To solve this problem, a planar cavity lens integrated with distributed Bragg reflectors (DBR-PCL) is used to replace the DLMC structure. In both the numerical and the experimental verification, we have obtained an image with lateral resolution of 200 nm at the wavelength of 640 nm, a similar resolving power as with the original design. Furthermore, we have changed the relative position between the pair-slit object and the DBR-PCL structure. The obtained results show that there is nearly no intensity difference between the two peaks of the images of the object. The simulation and experiment results show that the problem of the position sensitivity has been solved with the modified design.

8.2 Outlook

For the superlens with the DBR-PCL structure, the dispersion with a wide coverage of the transverse wave vector extends to frequencies ranging from 350 to 700 THz, which shows a potential for the superlens to be used under other incident wavelengths, maybe even under white light. However, several parameters need to be modified further because the optical response of both the DBR-PCL and the PPL structure are sensitive to the wavelength.

For the transmission dispersions of the DLMC or DBR-PCL structure which work as near-field transfer function, there are some peaks diffracted by the period of grating in the structures. These peaks will scatter the spatial information, therefore influence the imaging results. The dispersion could be further flattened by a meander structure with random grating periods (e.g. with an average periodicity of 400 nm at the wavelength of 640 nm). In the meanwhile, the randomly distributed meander structure may have a near-field dispersion with a broader transverse wave vector coverage.

The material used in the cascaded superlens is silver, which is suitable for fabrication with our facility at 640 nm but easy to be oxidized. It will be more suitable for application if the material has more stable chemical properties, e.g. with gold. Furthermore, dielectric materials such as polymers with lower attenuation is another choice. In addition, there is a chance to simplify the structure and to improve the transmission efficiency during the process of optimizing the structural parameters for desired optical properties.

The cascaded superlens studied in this dissertation is one-dimensional. If we replace the straight grating with circular ones, the superlens can be modified into be a two-dimensional superlens for a circular polarized incident light as shown in Fig. 8.1(a). We have tried to fabricate a circular PPL structure shown in Fig. 8.1(b).

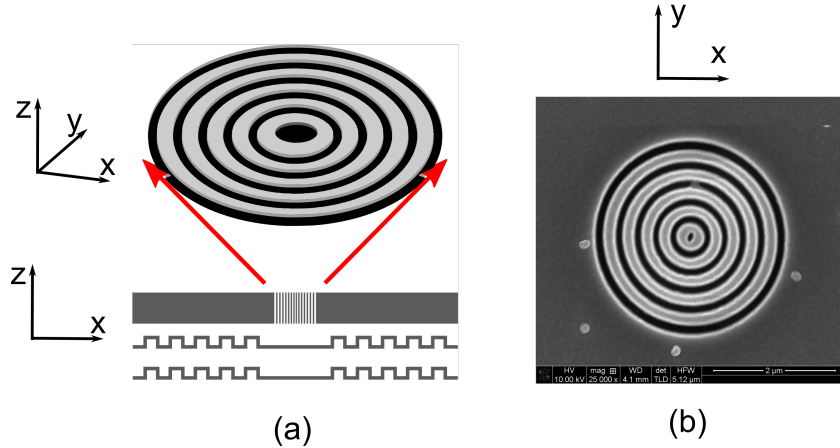


Figure 8.1 (a) Schematic of a two-dimensional cascaded superlens; (b) SEM image of a fabricated two-dimensional PPL structure.

Furthermore, the DLMC or the DBR-PCL structure can be replaced by any other plasmonic metasurfaces when they have an effective material dispersion suitable for near-field wave transformation or coupling, namely a relative smooth bandlimited near-field transmission in a possibly large spatial frequency range [28, 106, 142]. For the cascaded superlens, the transmission is relative low and the aperture size is only $2.1 \mu\text{m}$, which is mainly limited by the size of the PPL structure. It would be of great interest to replace the PPL structure by other types of planar lenses, e.g the ones proposed very recently [78, 143, 144], to further improve transmission or the view field of the lens.

Bibliography

- [1] Hans Blom and Jerker Widengren. Stimulated emission depletion microscopy. *Chemical reviews*, 117(11):7377–7427, 2017.
- [2] Junsuk Rho, Ziliang Ye, Yi Xiong, Xiaobo Yin, Zhaowei Liu, Hyeunseok Choi, Guy Bartal, and Xiang Zhang. Spherical hyperlens for two-dimensional sub-diffractive imaging at visible frequencies. *Nature communications*, 1:143, 2010.
- [3] Tengfei Li, Vivek Nagal, David H Gracias, and Jacob B Khurgin. Limits of imaging with multilayer hyperbolic metamaterials. *Optics Express*, 25(12):13588–13601, 2017.
- [4] Changbao Ma and Zhaowei Liu. Designing super-resolution metalenses by the combination of metamaterials and nanoscale plasmonic waveguide couplers. *Journal of Nanophotonics*, 5(1):051604, 2011.
- [5] John Brian Pendry. Negative refraction makes a perfect lens. *Physical review letters*, 85(18):3966, 2000.
- [6] Xiang Zhang and Zhaowei Liu. Superlenses to overcome the diffraction limit. *Nature materials*, 7(6):435–441, 2008.
- [7] Mankei Tsang and Demetri Psaltis. Magnifying metamaterial lens design by coordinate transformation. In *Quantum Electronics and Laser Science Conference*, page QFL5. Optical Society of America, 2008.
- [8] Robert T Thompson and Steven A Cummer. Transformation optics. In *Advances in Imaging and Electron Physics*, volume 171, pages 195–295. Elsevier, 2012.
- [9] Zubin Jacob, Leonid V Alekseyev, and Evgenii Narimanov. Optical hyperlens: far-field imaging beyond the diffraction limit. *Optics Express*, 14(18):8247–8256, 2006.
- [10] JB Pendry and S Anantha Ramakrishna. Near-field lenses in two dimensions. *Journal of Physics: Condensed Matter*, 14(36):8463, 2002.

- [11] Zhaowei Liu, Hyesog Lee, Yi Xiong, Cheng Sun, and Xiang Zhang. Far-field optical hyperlens magnifying sub-diffraction-limited objects. *Science*, 315(5819):1686–1686, 2007.
- [12] Weiwei Wan, Joseph Louis Ponsetto, and Zhaowei Liu. Numerical study of hyperlenses for three-dimensional imaging and lithography. *Optics Express*, 23(14):18501–18510, 2015.
- [13] Kai Yan, Ling Liu, Na Yao, Kaipeng Liu, Wenjuan Du, Wei Zhang, Wei Yan, Changtao Wang, and Xiangang Luo. Far-field super-resolution imaging of nano-transparent objects by hyperlens with plasmonic resonant cavity. *Plasmonics*, 11(2):475–481, 2016.
- [14] Nicholas Fang, Hyesog Lee, Cheng Sun, and Xiang Zhang. Sub-diffraction-limited optical imaging with a silver superlens. *Science*, 308(5721):534–537, 2005.
- [15] Lorenzo Ferrari, Chihhui Wu, Dominic Lepage, Xiang Zhang, and Zhaowei Liu. Hyperbolic metamaterials and their applications. *Progress in Quantum Electronics*, 40:1–40, 2015.
- [16] Prashant Shekhar, Jonathan Atkinson, and Zubin Jacob. Hyperbolic metamaterials: fundamentals and applications. *Nano convergence*, 1(1):14, 2014.
- [17] Linhua Xu, Gaige Zheng, Kun Cao, Wei Su, and Yuzhu Liu. Subwavelength imaging through one-dimensional metallodielectric photonic crystals at optical frequencies. *Optik-International Journal for Light and Electron Optics*, 125(14):3583–3586, 2014.
- [18] Yi Xiong, Zhaowei Liu, Stéphane Durant, Hyesog Lee, Cheng Sun, and Xiang Zhang. Tuning the far-field superlens: from uv to visible. *Optics Express*, 15(12):7095–7102, 2007.
- [19] Jingjing Zhang. Evolutionary optimization of compact dielectric lens for farfield sub-wavelength imaging. *Scientific reports*, 5:10083, 2015.
- [20] Dongdong Li, Dao Hua Zhang, Changchun Yan, and Zhengji Xu. Figure of merit for optimization of metal–dielectric multilayer lenses. *IEEE Transactions on Nanotechnology*, 13(3):452–457, 2014.
- [21] Zhaowei Liu, Stéphane Durant, Hyesog Lee, Yuri Pikus, Nicolas Fang, Yi Xiong, Cheng Sun, and Xiang Zhang. Far-field optical superlens. *Nano Letters*, 7(2):403–408, 2007.
- [22] Stéphane Durant, Zhaowei Liu, Jennifer M Steele, and Xiang Zhang. Theory of the transmission properties of an optical far-field superlens for imaging beyond the diffraction limit. *JOSA B*, 23(11):2383–2392, 2006.

-
- [23] Kedi Wu and Guo Ping Wang. Two-dimensional fibonacci grating for far-field super-resolution imaging. *Scientific reports*, 6:38651, 2016.
- [24] Feifei Wei, Dylan Lu, Hao Shen, Weiwei Wan, Joseph Louis Ponsetto, Eric Huang, and Zhaowei Liu. Wide field super-resolution surface imaging through plasmonic structured illumination microscopy. *Nano letters*, 14(8):4634–4639, 2014.
- [25] Feng Hu, Michael G Somekh, Darren J Albutt, Kevin Webb, Emilia Moradi, and Chung W See. Sub-100 nm resolution microscopy based on proximity projection grating scheme. *Scientific reports*, 5:8589, 2015.
- [26] C Jouvaud, A Ourir, and J de Rosny. Far-field imaging with a multi-frequency metalens. *Applied Physics Letters*, 104(24):243507, 2014.
- [27] Ren Wang, Bing-Zhong Wang, Zhi-Shuang Gong, and Xiao Ding. Far-field subwavelength imaging with near-field resonant metalens scanning at microwave frequencies. *Scientific reports*, 5:11131, 2015.
- [28] Changbao Ma and Zhaowei Liu. A super resolution metalens with phase compensation mechanism. *Applied Physics Letters*, 96(18):183103, 2010.
- [29] Changbao Ma, Marco A Escobar, and Zhaowei Liu. Extraordinary light focusing and fourier transform properties of gradient-index metalenses. *Physical Review B*, 84(19):195142, 2011.
- [30] Lukas Novotny and Bert Hecht. *Principles of nano-optics*. Cambridge university press, 2012.
- [31] Haofei Shi, Changtao Wang, Chunlei Du, Xiangang Luo, Xiaochun Dong, and Hongtao Gao. Beam manipulating by metallic nano-slits with variant widths. *Optics Express*, 13(18):6815–6820, 2005.
- [32] Lieven Verslegers, Peter B Catrysse, Zongfu Yu, Justin S White, Edward S Barnard, Mark L Brongersma, and Shanhui Fan. Planar lenses based on nanoscale slit arrays in a metallic film. *Nano letters*, 9(1):235–238, 2008.
- [33] Hadiseh Nasari and Mohammad Sadegh Abrishamian. Electrically tunable light focusing via a plasmonic lens. *Journal of Optics*, 14(12):125002, 2012.
- [34] Gang Wu, Jianjun Chen, Ru Zhang, Jinghua Xiao, and Qihuang Gong. Highly efficient nanofocusing in a single step-like microslit. *Optics Letters*, 38(19):3776–3779, 2013.

- [35] Liwei Fu, Philipp Schau, Karsten Frenner, and Wolfgang Osten. A cascaded plasmonic superlens for near field imaging with magnification. *Proc. SPIE*, 9526:95260Z, 2015.
- [36] Aurélie Jost and Rainer Heintzmann. Superresolution multidimensional imaging with structured illumination microscopy. *Annual Review of Materials Research*, 43:261–282, 2013.
- [37] Alexander V Kildishev and Vladimir M Shalaev. Engineering space for light via transformation optics. *Optics Letters*, 33(1):43–45, 2008.
- [38] Katherine A Willets, Andrew J Wilson, Vignesh Sundaresan, and Padmanabh B Joshi. Super-resolution imaging and plasmonics. *Chemical reviews*, 117(11):7538–7582, 2017.
- [39] Dylan Lu and Zhaowei Liu. Hyperlenses and metalenses for far-field super-resolution imaging. *Nature Communications*, 3:1–9, 2012.
- [40] Xiang Hao, Cuifang Kuang, Zhaotai Gu, Yifan Wang, Shuai Li, Yulong Ku, Yanghui Li, Jianhong Ge, and Xu Liu. From microscopy to nanoscopy via visible light. *Light: Science & Applications*, 2(10):e108, 2013.
- [41] Ernst Abbe. Beiträge zur Theorie des Mikroskops und der mikroskopischen Wahrnehmung. *Archiv für mikroskopische Anatomie*, 9(1):413–418, 1873.
- [42] Ernst HK Stelzer. Light microscopy: Beyond the diffraction limit? *Nature*, 417(6891):806–807, 2002.
- [43] Qiang Wu, GD Feke, Robert D Grober, and LP Ghislain. Realization of numerical aperture 2.0 using a gallium phosphide solid immersion lens. *Applied Physics Letters*, 75(26):4064–4066, 1999.
- [44] Zeiss. Oil immersion and refractive index, 2018. [Online; accessed 18-January-2018].
- [45] Alexander Egner, Sophie Verrier, Alexander Goroshkov, Hans-Dieter Söling, and Stefan W Hell. 4pi-microscopy of the golgi apparatus in live mammalian cells. *Journal of structural biology*, 147(1):70–76, 2004.
- [46] Wolfgang Osten and Nadya Reingand. *Optical imaging and metrology: advanced technologies*. John Wiley & Sons, 2012.
- [47] Yochai Blau, Doron Shterman, Guy Bartal, and Bergin Gjonaj. Double moiré structured illumination microscopy with high-index materials. *Optics Letters*, 41(15):3455–3458, 2016.

-
- [48] Mark AA Neil, Rimas Juškaitis, and Tony Wilson. Method of obtaining optical sectioning by using structured light in a conventional microscope. *Optics Letters*, 22(24):1905–1907, 1997.
- [49] EJKTDJSRL Betzig, JK Trautman, TD Harris, JS Weiner, and RL Kostelak. Breaking the diffraction barrier: optical microscopy on a nanometric scale. *Science*, 251(5000):1468–1470, 1991.
- [50] Dejan Karadaglić and Tony Wilson. Image formation in structured illumination wide-field fluorescence microscopy. *Micron*, 39(7):808–818, 2008.
- [51] Mats GL Gustafsson. Nonlinear structured-illumination microscopy: wide-field fluorescence imaging with theoretically unlimited resolution. *Proceedings of the National Academy of Sciences of the United States of America*, 102(37):13081–13086, 2005.
- [52] Th Lacoste, Th Huser, R Prioli, and H Heinzelmänn. Contrast enhancement using polarization-modulation scanning near-field optical microscopy (pm-snom). *Ultramicroscopy*, 71(1):333–340, 1998.
- [53] Max Eisele. s-snom based microscopy and spectroscopy for nanoscale material characterization. *Bulletin of the American Physical Society*, 62, 2017.
- [54] Viktor Palm, Martti Pärs, Ardi Loot, Mihkel Rähn, and Vladimir Hizhnyakov. On mesoscopic effect of spectral modulation and its potential influence on hyperspectral snom imaging results. *Microscopy and imaging science: practical approaches to applied research and education*, pages 610–619, 2017.
- [55] Angela E Klein, Norik Janunts, Sören Schmidt, Shakeeb Bin Hasan, Christoph Etrich, Stefan Fasold, Thomas Kaiser, Carsten Rockstuhl, and Thomas Pertsch. Dual-snom investigations of multimode interference in plasmonic strip waveguides. *Nanoscale*, 9(20):6695–6702, 2017.
- [56] Stefan W Hell and Jan Wichmann. Breaking the diffraction resolution limit by stimulated emission: stimulated-emission-depletion fluorescence microscopy. *Optics Letters*, 19(11):780–782, 1994.
- [57] Birka Hein, Katrin I Willig, and Stefan W Hell. Stimulated emission depletion (sted) nanoscopy of a fluorescent protein-labeled organelle inside a living cell. *Proceedings of the National Academy of Sciences*, 105(38):14271–14276, 2008.
- [58] Peng Gao and G. Ulrich Nienhaus. Precise background subtraction in stimulated emission double depletion nanoscopy. *Optics Letters*, 42(4):831, 2017.

- [59] Peng Gao, Benedikt Prunsche, Lu Zhou, Karin Nienhaus, and G. Ulrich Nienhaus. Background suppression in fluorescence nanoscopy with stimulated emission double depletion. *Nature Photonics*, 11(3):163–169, 2017.
- [60] Bo Huang, Wenqin Wang, Mark Bates, and Xiaowei Zhuang. Three-dimensional super-resolution imaging by stochastic optical reconstruction microscopy. *Science*, 319(5864):810–813, 2008.
- [61] Michael J Rust, Mark Bates, and Xiaowei Zhuang. Sub-diffraction-limit imaging by stochastic optical reconstruction microscopy (storm). *Nature methods*, 3(10):793–796, 2006.
- [62] Jennifer Lippincott-Schwartz and George H Patterson. Development and use of fluorescent protein markers in living cells. *Science*, 300(5616):87–91, 2003.
- [63] Hari Shroff, Catherine G Galbraith, James A Galbraith, and Eric Betzig. Live-cell photoactivated localization microscopy of nanoscale adhesion dynamics. *Nature methods*, 5(5):417–423, 2008.
- [64] Wei Ting Chen, Alexander Y Zhu, Mohammadreza Khorasaninejad, Zhujun Shi, Vyshakh Sanjeev, and Federico Capasso. Immersion meta-lenses at visible wavelengths for nanoscale imaging. *Nano letters*, 17(5):3188–3194, 2017.
- [65] Lianlin Li, Fang Li, Tie Jun Cui, and Kan Yao. Far-field imaging beyond diffraction limit using single sensor in combination with a resonant aperture. *Optics Express*, 23(1):401–412, 2015.
- [66] Mohammadreza Khorasaninejad, Alexander Yutong Zhu, Charles Roques-Carmes, Wei Ting Chen, Jaewon Oh, Ishan Mishra, Robert C Devlin, and Federico Capasso. Polarization-insensitive metalenses at visible wavelengths. *Nano letters*, 16(11):7229–7234, 2016.
- [67] Patrice Genevet, Federico Capasso, Francesco Aieta, Mohammadreza Khorasaninejad, and Robert Devlin. Recent advances in planar optics: from plasmonic to dielectric metasurfaces. *Optica*, 4(1):139, 2017.
- [68] Francesco Aieta, Patrice Genevet, Mikhail Kats, and Federico Capasso. Aberrations of flat lenses and aplanatic metasurfaces. *Optics Express*, 21(25):31530–31539, 2013.
- [69] Jiao Lin, Patrice Genevet, Mikhail A Kats, Nicholas Antoniou, and Federico Capasso. Nanostructured holograms for broadband manipulation of vector beams. *Nano letters*, 13(9):4269–4274, 2013.

-
- [70] Lingling Cao, Yong-Hong Ye, Ling Yao, and Minglei Guo. Dependence of focal position on the microscale spherical lens imaging. *Optics Communications*, 353:184–188, 2015.
- [71] Lin Li, Wei Guo, Yinzhou Yan, Seoungjun Lee, and Tao Wang. Label-free super-resolution imaging of adenoviruses by submerged microsphere optical nanoscopy. *Light: Science & Applications*, 2(9):e104, 2013.
- [72] Xiang Hao, Cuifang Kuang, Xu Liu, Haijun Zhang, and Yanghui Li. Microsphere based microscope with optical super-resolution capability. *Applied Physics Letters*, 99(20):203102, 2011.
- [73] Hui Yang, Raphaël Trouillon, Gergely Huszka, and Martin AM Gijs. Super-resolution imaging of a dielectric microsphere is governed by the waist of its photonic nanojet. *Nano letters*, 16(8):4862–4870, 2016.
- [74] Zengbo Wang, Wei Guo, Lin Li, Boris Luk’yanchuk, Ashfaq Khan, Zhu Liu, Zaichun Chen, and Minghui Hong. Optical virtual imaging at 50 nm lateral resolution with a white-light nanoscope. *Nature communications*, 2:218, 2011.
- [75] Arash Darafsheh, Gary F Walsh, Luca Dal Negro, and Vasily N Astratov. Optical super-resolution by high-index liquid-immersed microspheres. *Applied Physics Letters*, 101(14):141128, 2012.
- [76] Yinzhou Yan, Lin Li, Chao Feng, Wei Guo, Seoungjun Lee, and Minghui Hong. Microsphere-coupled scanning laser confocal nanoscope for sub-diffraction-limited imaging at 25 nm lateral resolution in the visible spectrum. *Acs Nano*, 8(2):1809–1816, 2014.
- [77] Hou-Tong Chen, Antoinette J Taylor, and Nanfang Yu. A review of metasurfaces: physics and applications. *Reports on Progress in Physics*, 79(7):076401, 2016.
- [78] Yang Li, Xiong Li, Mingbo Pu, Zeyu Zhao, Xiaoliang Ma, Yanqin Wang, and Xiang-gang Luo. Achromatic flat optical components via compensation between structure and material dispersions. *Scientific reports*, 6:19885, 2016.
- [79] Guoxing Zheng, Ruiying Zhang, Song Li, Ping’an He, Hui Zhou, and Yan Shi. A hyperlens-embedded solid immersion lens for beam focusing beyond the diffraction limit. *IEEE Photonics Technology Letters*, 23(17):1234–1236, 2011.
- [80] RA Shelby, DR Smith, SC Nemat-Nasser, and Sheldon Schultz. Microwave transmission through a two-dimensional, isotropic, left-handed metamaterial. *Applied Physics Letters*, 78(4):489–491, 2001.

- [81] Jason Valentine, Shuang Zhang, Thomas Zentgraf, Erick Ulin-Avila, Dentcho A Genov, Guy Bartal, and Xiang Zhang. Three-dimensional optical metamaterial with a negative refractive index. *Nature*, 455(7211):376–379, 2008.
- [82] Chen Zhao, Yun-song Zhou, Yan Zhang, and Huai-yu Wang. The imaging properties of the metal superlens. *Optics Communications*, 368:180–184, 2016.
- [83] Amir Arbabi, Yu Horie, Mahmood Bagheri, and Andrei Faraon. Dielectric metasurfaces for complete control of phase and polarization with subwavelength spatial resolution and high transmission. *Nature nanotechnology*, 10(11):937–943, 2015.
- [84] Nicholas Fang, Hyesog Lee, Cheng Sun, and Xiang Zhang. Sub-diffraction-limited optical imaging with a silver superlens. *Science*, 308(5721):534–537, 2005.
- [85] Richard A Shelby, David R Smith, and Seldon Schultz. Experimental verification of a negative index of refraction. *Science*, 292(5514):77–79, 2001.
- [86] David R Smith, Willie J Padilla, DC Vier, Syrus C Nemat-Nasser, and Seldon Schultz. Composite medium with simultaneously negative permeability and permittivity. *Physical review letters*, 84(18):4184, 2000.
- [87] WH Wee, YJ Ye, and Yu Luo. Towards a practical compact magnifying superlens—a simple simplicial design. *Journal of Optics*, 18(4):044011, 2016.
- [88] David R Smith. How to build a superlens. *Science*, 308(5721):502–503, 2005.
- [89] Erik Mårzell, Robin Svärd, Miguel Miranda, Chen Guo, Anne Harth, Eleonora Lorek, Johan Mauritsson, Cord L Arnold, Hongxing Xu, Anne L’Huillier, et al. Direct sub-wavelength imaging and control of near-field localization in individual silver nanocubes. *Applied Physics Letters*, 107(20):201111, 2015.
- [90] Fuyang Xu, Genhua Chen, Chinhua Wang, Bing Cao, and Yimin Lou. Superlens imaging with a surface plasmon polariton cavity in imaging space. *Optics Letters*, 38(19):3819–3822, 2013.
- [91] Changtao Wang, Ping Gao, Zeyu Zhao, Na Yao, Yanqin Wang, Ling Liu, Kaipeng Liu, and Xiangang Luo. Deep sub-wavelength imaging lithography by a reflective plasmonic slab. *Optics Express*, 21(18):20683–20691, 2013.
- [92] Atsushi Ono, Jun-ichi Kato, and Satoshi Kawata. Subwavelength optical imaging through a metallic nanorod array. *Physical review letters*, 95(26):267407, 2005.

-
- [93] Gennady Shvets, S Trendafilov, JB Pendry, and A Sarychev. Guiding, focusing, and sensing on the subwavelength scale using metallic wire arrays. *Physical review letters*, 99(5):053903, 2007.
- [94] Yan Zhao, George Palikaras, Pavel A Belov, Rostyslav F Dubrovka, Constantin R Simovski, Yang Hao, and Clive G Parini. Magnification of subwavelength field distributions using a tapered array of metallic wires with planar interfaces and an embedded dielectric phase compensator. *New Journal of Physics*, 12(10):103045, 2010.
- [95] Seunghoon Han, Yi Xiong, Dentcho Genov, Zhaowei Liu, Guy Bartal, and Xiang Zhang. Ray optics at sub-wavelength scale. In *Plasmonics and Metamaterials*, page MMB2. Optical Society of America, 2008.
- [96] Mahmoud El Maklizi, Mostafa Hendawy, and Mohamed a Swillam. Super-focusing of visible and UV light using a meta surface. *Journal of Optics*, 16(10):105007, 2014.
- [97] BDF Casse, WT Lu, YJ Huang, E Gultepe, L Menon, and S Sridhar. Super-resolution imaging using a three-dimensional metamaterials nanolens. *Applied Physics Letters*, 96(2):023114, 2010.
- [98] Abdelwaheb Ourir, Geoffroy Lerosey, Fabrice Lemoult, Mathias Fink, and Julien de Rosny. Far field subwavelength imaging of magnetic patterns. *Applied Physics Letters*, 101(11):111102, 2012.
- [99] Camille Jouvaud, Abdelwaheb Ourir, and Julien de Rosny. Surface waves radiation by finite arrays of magnetoelectric resonators. *Progress In Electromagnetics Research*, 132:177–198, 2012.
- [100] Shubin Li, Changhe Zhou, Hongchao Cao, Jun Wu, and Junjie Yu. Mode conversion and coupling in a slanted grating. *Optics Letters*, 39(7):1976–1979, 2014.
- [101] Stéphane Durant, Zhaowei Liu, Nicholas Fang, and Xiang Zhang. Theory of optical imaging beyond the diffraction limit with a far-field superlens. *Plasmonics: Metallic Nanostructures and Their Optical Properties IV, Proc. SPIE*, 6323:63231H, 2006.
- [102] Zhaowei Liu, Hyesog Lee, Yi Xiong, Cheng Sun, and Xiang Zhang. Far-field optical hyperlens magnifying sub-diffraction-limited objects. *Science*, 315(5819):1686–1686, 2007.
- [103] Hyesog Lee, Zhaowei Liu, Yi Xiong, Cheng Sun, and Xiang Zhang. Development of optical hyperlens for imaging below the diffraction limit. *Optics Express*, 15(24):15886–15891, 2007.

- [104] Igor I Smolyaninov, Yu-Ju Hung, and Christopher C Davis. Magnifying superlens in the visible frequency range. *Science*, 315(5819):1699–1701, 2007.
- [105] Xiao Ming Goh, Ling Lin, and Ann Roberts. Plasmonic lenses for wavefront control applications using two-dimensional nanometric cross-shaped aperture arrays. *JOSA B*, 28(3):547–553, 2011.
- [106] L. E. Helseth. The almost perfect lens and focusing of evanescent waves. *Optics Communications*, 281(8):1981–1985, 2008.
- [107] Heng-He Tang and Pu-Kun Liu. Long-distance super-resolution imaging assisted by enhanced spatial fourier transform. *Optics Express*, 23(18):23613–23623, 2015.
- [108] Alessandro Salandrino and Nader Engheta. Far-field subdiffraction optical microscopy using metamaterial crystals: Theory and simulations. *Physical Review B*, 74(7):075103, 2006.
- [109] MG Moharam and TK Gaylord. Rigorous coupled-wave analysis of planar-grating diffraction. *JOSA*, 71(7):811–818, 1981.
- [110] MG Moharam and TK Gaylord. Rigorous coupled-wave analysis of grating diffraction—e-mode polarization and losses. *JOSA*, 73(4):451–455, 1983.
- [111] MG Moharam, TK Gaylord, Eric B Grann, and Drew A Pommet. Formulation for stable and efficient implementation of the rigorous coupled-wave analysis of binary gratings. *JOSA A*, 12(5):1068–1076, 1995.
- [112] Lifeng Li. Use of fourier series in the analysis of discontinuous periodic structures. *JOSA A*, 13(9):1870–1876, 1996.
- [113] NP Van der Aa and RMM Mattheij. Computing shape parameter sensitivity of the field of one-dimensional surface-relief gratings by using an analytical approach based on rewa. *JOSA A*, 24(9):2692–2700, 2007.
- [114] MG Moharam, Drew A Pommet, Eric B Grann, and TK Gaylord. Stable implementation of the rigorous coupled-wave analysis for surface-relief gratings: enhanced transmittance matrix approach. *JOSA A*, 12(5):1077–1086, 1995.
- [115] JR Sambles, GW Bradbery, and Fuzi Yang. Optical excitation of surface plasmons: an introduction. *Contemporary physics*, 32(3):173–183, 1991.
- [116] Liwei Fu, Philipp Schau, Karsten Frenner, Wolfgang Osten, Thomas Weiss, Heinz Schweizer, and Harald Giessen. Mode coupling and interaction in a plasmonic micro-cavity with resonant mirrors. *Physical Review B*, 84(23):235402, 2011.

-
- [117] Philipp Schau, Karsten Frenner, Liwei Fu, Heinz Schweizer, Harald Giessen, and Wolfgang Osten. Design of high-transmission metallic meander stacks with different grating periodicities for subwavelength-imaging applications. *Optics Express*, 19(4):3627–3636, 2011.
- [118] Philipp Schau, Liwei Fu, Karsten Frenner, Martin Schäferling, Heinz Schweizer, Harald Giessen, Luis Miguel Gaspar Venancio, and Wolfgang Osten. Polarization scramblers with plasmonic meander-type metamaterials. *Optics Express*, 20(20):22700–22711, 2012.
- [119] Liwei Fu, Audrey Berrier, Huiyu Li, Philipp Schau, Karsten Frenner, Martin Dreschel, and Wolfgang Osten. Depolarization of a randomly distributed plasmonic meander metasurface characterized by mueller matrix spectroscopic ellipsometry. *Optics Express*, 24(24):28056–28064, 2016.
- [120] Reuven Gordon and Alexandre G Brolo. Increased cut-off wavelength for a subwavelength hole in a real metal. *Optics Express*, 13(6):1933–1938, 2005.
- [121] Joseph W Goodman. *Introduction to Fourier optics*. Roberts and Company Publishers, 2005.
- [122] Peter B Johnson and R-W Christy. Optical constants of the noble metals. *Physical review B*, 6(12):4370, 1972.
- [123] Hans Lüth. *Solid surfaces, interfaces and thin films*, volume 4. Springer, 2001.
- [124] Joy George. *Preparation of thin films*. CRC Press, 1992.
- [125] Harry J Levinson. *Principles of lithography*, volume 146. SPIE press, 2005.
- [126] Steve Reyntjens and Robert Puers. A review of focused ion beam applications in microsystem technology. *Journal of micromechanics and microengineering*, 11(4):287, 2001.
- [127] Richard Wirth. Focused ion beam (fib) combined with sem and tem: Advanced analytical tools for studies of chemical composition, microstructure and crystal structure in geomaterials on a nanometre scale. *Chemical Geology*, 261(3):217–229, 2009.
- [128] Alfred Wagner. Applications of focused ion beams. *Nuclear Instruments and Methods in Physics Research*, 218(1-3):355–362, 1983.
- [129] Joseph I Goldstein, Dale E Newbury, Joseph R Michael, Nicholas WM Ritchie, John Henry J Scott, and David C Joy. Focused ion beam applications in the sem laboratory. In *Scanning Electron Microscopy and X-Ray Microanalysis*, pages 517–528. Springer, 2018.

- [130] FEI. *Helios NanoLab 400/400S/400 ML/600 System User's Guide*. 2009.
- [131] Nan Yao. *Focused ion beam systems: basics and applications*. Cambridge University Press, 2007.
- [132] Weiqiang Chen, Mark D Thoreson, Main Campus, Alexander V Kildishev, and Vladimir M Shalaev. Ultra-thin ultra-smooth and low-loss silver films on a germanium wetting layer on a germanium wetting layer. *Optics Express*, 18(5):5124, 2010.
- [133] VJ Logeeswaran, Nobuhiko P Kobayashi, M Saif Islam, Wei Wu, Pratik Chaturvedi, Nicholas X Fang, Shih Yuan Wang, and R Stanley Williams. Ultrasoother silver thin films deposited with a germanium nucleation layer. *Nano letters*, 9(1):178–182, 2008.
- [134] P Melpignano, C Cioarec, R Clergereaux, N Gherardi, C Villeneuve, and L Datas. E-beam deposited ultra-smooth silver thin film on glass with different nucleation layers: an optimization study for oled micro-cavity application. *Organic Electronics*, 11(6):1111–1119, 2010.
- [135] A De Rooij. The oxidation of silver by atomic oxygen. *EsA Journal*, 13:363–382, 1989.
- [136] ML Zheludkevich, AG Gusakov, AG Voropaev, AA Vecher, EN Kozyrski, and SA Raspopov. Oxidation of silver by atomic oxygen. *Oxidation of Metals*, 61(1):39–48, 2004.
- [137] Hans Martin Hövel. *Elektrodynamik dünner metallfilme am isolator-metall-übergang*. 2010.
- [138] Liwei Fu, Heinz Schweizer, Thomas Weiss, and Harald Giessen. Optical properties of metallic meanders. 26(12):111–119, 2009.
- [139] Zeyu Zhao, Yunfei Luo, Na Yao, Wei Zhang, Changtao Wang, Ping Gao, Chengwei Zhao, Mingbo Pu, and Xiangang Luo. Modeling and experimental study of plasmonic lens imaging with resolution enhanced methods. *Optics Express*, 24(24):27115–27126, 2016.
- [140] Yunfei Luo, Ling Liu, Wei Zhang, Weijie Kong, Chengwei Zhao, Ping Gao, Zeyu Zhao, Mingbo Pu, Changtao Wang, and Xiangang Luo. Proximity correction and resolution enhancement of plasmonic lens lithography far beyond the near field diffraction limit. *RSC Advances*, 7(20):12366–12373, 2017.
- [141] Mohammadreza Khorasaninejad and Federico Capasso. Metalenses: Versatile multifunctional photonic components. *Science*, 358(6367):eaam8100, 2017.

- [142] Carlos J Zapata-Rodriguez, David Pastor Calle, Vincente Camps, Maria T Caballero, J Juan, et al. Three-dimensional point spread function of multilayered flat lenses and its application to extreme subwavelength resolution. *Journal of Nanophotonics*, 5(1):051807, 2011.
- [143] Yechuan Zhu, Weizheng Yuan, Yiting Yu, and Ping Wang. Robustly efficient superfocusing of immersion plasmonic lenses based on coupled nanoslits. *Plasmonics*, 11(6):1543–1548, 2016.
- [144] Sumit Saxena, Raghvendra Pratap Chaudhary, Abhay Singh, Saurabh Awasthi, and Shobha Shukla. Plasmonic micro lens for extraordinary transmission of broadband light. *Scientific reports*, 4:5586, 2014.

Publications

The results obtained while working on this dissertation were published in print:

- Li, Huiyu, Liwei Fu, Karsten Frenner, and Wolfgang Osten. "A cascaded plasmonic superlens for far-field imaging with magnification at visible wavelength." *Optics Express* 26, no. 8 (2018): 10888-10897,
- Li, Huiyu, Liwei Fu, Karsten Frenner, and Wolfgang Osten. "Cascaded DBR plasmonic cavity lens for far-field subwavelength imaging at a visible wavelength." *Optics Express* 26, no. 15 (2018): 19574-19582,
- Li, Huiyu, Liwei Fu, Karsten Frenner, and Wolfgang Osten. "Nanofabrication results of a novel cascaded plasmonic superlens: lessons learned." *Proc. SPIE*, vol. 10330, (2017): 103300Y,
- Fu, Liwei, Audrey Berrier, Huiyu Li, Philipp Schau, Karsten Frenner, Martin Dressel, and Wolfgang Osten. "Depolarization of a randomly distributed plasmonic meander metasurface characterized by Mueller matrix spectroscopic ellipsometry." *Optics express* 24, no. 24 (2016): 28056-28064,
- Fu, Liwei, Karsten Frenner, Huiyu Li, and Wolfgang Osten. "A silicon superlens with a simple design working at visible wavelengths." *Proc. SPIE*, Vol. 9890, (2016): 98900I.

Lebenslauf

Huiyu Li,

Data of birth: June 25, 1989

- | | |
|-------------------|---|
| 09/2008 - 07/2012 | Bachelor of Engineer, Optics and of Literature, English, Harbin Institute of Technology |
| 09/2012 - 06/2014 | Master of Engineering, Optics, Harbin Institute of Technology, |
| 11/2014 - now | Doctor of Engineering, Optics, Institut für Technische Optik, Universität Stuttgart in group of “High resolution metrology and simulation” |

Acknowledgements

I would like to thank all the people who have helped me and contributed to this thesis. Partially grateful to:

Herr Prof. Dr. Wolfgang Osten for kindly agreeing to be my advisor, for giving me the opportunity to study at the Institute of Applied Optics, for all his guidance, support and advise, for making experiment possible and the opportunity to attend conferences and meetings.

Prof. Manfred Berroth for kindly being my co-professor.

Prof. Harald Giessen and Dr. Mario Hentschel for kindly access to their lab.

Dr. Karsten Frenner for always providing valuable suggestions and encouragement.

Dr. Liwei Fu for her mentorship, for many stimulating discussions and for experiment suggestions.

Herr Thomas Schoder, Herr Heiko Bieger, Frau Monika Ubl and Herr Ramon Walter for their technique support.

Frau Katja Costantino and Frau Christina Hübl for their support in administrative arrangement.

Herr Haiyu yang, Herr Shihao dong, Dr. Giancarlo Pedrini, Frau Maria Laura Gödecke and Frau Sindy Peterhänse for help in living in Germany.

All my colleagues at ITO for warm working atmosphere at many excursions, parties...

I acknowledge also the support from China Scholarship Council (CSC) and Deutsche Forschungsgemeinschaft (DFG under project OS111/40-1).

Last but not least, I would like to thank my parents for their endless love and support and all of my friends.

ISBN 978-3-923560-96-7